

Comparative Study of Silver Nanoparticles and Silver(111) by means of Femtosecond Laser Pulses

vorgelegt von Diplom-Physiker

Florian Evers

aus München

Fakultät II - Mathematik und Naturwissenschaften
der Technischen Universität Berlin
zur Erlangung des akademischen Grades
Doktor der Naturwissenschaften
Dr. rer. nat.
genehmigte Dissertation

Promotionsausschuss:

Vorsitzender: Prof. Dr. E. Sedlmayr

Berichter/Gutachter: Prof. Dr. H.-J. Freund

Berichter/Gutachter: Prof. Dr. T. Möller

Tag der wissenschaftlichen Aussprache: 20. März 2006

Berlin 2006

D 83

Abstract

As fundamental study to photodesorption experiments silver nanoparticles supported by an Al_2O_3 -film were investigated with femtosecond laser pulses, providing the excitation of the surface plasmon. For that purpose a noncollinear optical parametric amplifier was constructed to reduce the original pulse width of ≈ 100 fs to less than 60 fs, approaching relevant excited state lifetimes of less than 20 fs. At the same time the accessible photon energy range (1.58 eV - 2.14 eV and 3.16 eV - 4.28 eV) was extended to a continuously tunable range reaching from 1.2 eV up to 5.3 eV. This allows one-photon photoemission (1PPE) spectroscopy. The small required pump intensity makes two-colour experiments possible.

Employing the 5.3 eV photon energy output 1PPE experiments were carried out. These experiments revealed a peak below the Fermi level shifting to lower binding energy with increasing particle size. To check its relation to the surface state on Ag(111) at similar position, both the nanoparticles and a Ag(111) crystal were deposited with cesium to alter the work function. The resulting influences were discussed by comparison with the phase accumulation model of surface states.

In two-photon photoemission (2PPE) spectroscopy the peak below the Fermi cutoff appeared broadened. Firstly, its intensity dependence on particle size was recorded at the plasmon resonance position of silver nanoparticles ($h\nu=3.6$ eV) and off-resonant ($h\nu=3.16$ eV). The intensity at off-resonance was a factor of six lower than at resonance but still up to 100 times larger than the corresponding overall photoemission yield of Ag(111). By tuning the photon energy the peak's shape changed which could be assigned to a resonant transition from an occupied state via an unoccupied state. The dependence of these states on particle size suggested quantum well states (QWS), also checked by deposition with cesium. The resulting decrease of work function revealed additional features, as expected from the applied QWS-model. By taking a broad particle size distribution into account, a simulation by QWS could reflect the essential experimental features. Moreover, the QWS at lowest energy was identified with the peak detected in 1PPE.

By exposure to NO, favoured for photodesorption experiments, the plasmon excitation on nanoparticles was strongly damped. The dependence on coverage suggested that both excitation steps in 2PPE are driven by plasmon excitation. This was also confirmed by two-colour experiments. Further, time-resolved experiments could map the major nonradiative decay channel of the plasmon excitation. First results on intermediate state lifetimes were obtained. The entirety of 2PPE results showed that the excitation of plasmons can simply be regarded as enhancement of the electric field with respect to photoemission, which was determined to be a factor of 2.3 in this case.

Als Grundlage für Photodesorptionsexperimente wurden Silbernanopartikel auf einem Al_2O_3 -Film mittels ultrakurzer Laserpulse untersucht, welche die Anregung von Oberflächenplasmonen ermöglichen. Zu diesem Zweck wurde ein nichtkollinear optisch parametrischer Verstärker konstruiert, welcher die ursprüngliche Pulslänge von 100 fs auf weniger als 60 fs verkürzt und damit Lebensdauern relevanter angeregter Zustände von weniger als 20 fs näher kommt. Gleichzeitig wurde der zugängliche Photonenergiebereich (1,58 eV - 2,14 eV; 3,16 eV - 4,28 eV) auf einen kontinuierlich durchstimmbaren Bereich von 1,2 eV bis 5,3 eV erweitert. Dies ermöglicht einerseits Ein-Photon-Photoemissions(1PPE)-Spektroskopie und andererseits Zwei-Farben-Experimente durch eine geringe benötigte Pump-Intensität.

Mit Hilfe der 5,3 eV Photonenergie wurden 1PPE Messungen durchgeführt, die zur Detektion eines Peaks unterhalb des Fermi-Niveaus führten. Mit zunehmender Partikelgröße bewegte sich dieser zu niedrigeren Bindungsenergien. Um einen möglichen Zusammenhang mit dem Oberflächenzustand auf Ag(111) bei ähnlicher Bindungsenergie aufzuzeigen, wurden Nanopartikel sowie ein Ag(111)-Kristall mit Cäsium bedampft, was eine Änderung der Austrittsarbeit bewirkte. Der resultierende Einfluß auf die jeweiligen Zustände wurde anhand des Phasen-Akkumulations-Modells für Oberflächenzustände diskutiert.

Die Anwendung von Zwei-Photonen-Photoemissions(2PPE)-Spektroskopie führte zu einer Verbreiterung des Peaks unterhalb des Fermi-Niveaus. Dessen Intensitätsabhängigkeit von der Partikelgröße wurde einerseits bei resonanter Plasmonenanregung ($h\nu=3.6$ eV) und andererseits außerhalb der Resonanz ($h\nu=3.16$ eV) untersucht. Die nicht resonante Anregung zeigte 6-fach niedrigere Intensität als die resonante, war jedoch immer noch 100-fach höher als die entsprechende Photoemission von Ag(111). Ein Durchstimmen der Photonenergie beeinflusste die Peak-Form, was durch einen resonanten Übergang von einem besetzten über einen unbesetzten Zustand erklärt werden konnte. Die Abhängigkeit dieser Zustände von der Partikelgröße deutete auf zugrundeliegende Quantum-Well(QW)-Zustände, was wiederum durch Bedampfen mit Cäsium überprüft wurde. Die daraus folgende Abnahme der Austrittsarbeit offenbarte zusätzliche Strukturen, im Einklang mit dem gängigen QW-Zustandsmodell. Diese Strukturen konnten durch eine QW-Zustandssimulation für eine breite Partikelgrößenverteilung wiedergegeben werden, wobei der QW-Zustand mit höchster Bindungsenergie mit dem in 1PPE detektierten Peak identifiziert wurde.

Die Adsorption von NO führte zu einer starken Dämpfung der Plasmonenanregung. Deren Abhängigkeit von der Bedeckung ließ auf eine Beteiligung des Plasmons in beiden 2PPE-Anregungsschritten schließen, was durch Zwei-Farben-Experimente bestätigt wurde. Zeitaufgelöste Messungen konnten schließlich den wesentlichen strahlungslosen Zerfallskanal der Plasmonenanregung aufzeigen. Außerdem ließen sich Lebensdauern von unbesetzten Zwischenzuständen bestimmen. Die gesamten 2PPE Resultate legen letztlich den Schluß nahe, daß die Plasmonenanregung im Hinblick auf die Photoemission lediglich zu einer Erhöhung des elektrischen Feldes führt, welche im vorliegenden Fall einem Faktor von 2,3 entspricht.

Contents

1	Introduction	7
2	Properties of Silver Nanoparticles	11
2.1	Electronic States	11
2.1.1	Surface States	11
2.1.2	Quantum Well States	14
2.2	Plasmon Excitation	17
2.2.1	Surface Plasmon in Silver Nanoparticles	18
3	Experimental Setup	21
3.1	UHV System	21
3.1.1	Sample Mount	23
3.1.2	Time-Of-Flight Spectrometer	23
3.2	Sample Preparation	28
3.2.1	Ag(111)	28
3.2.2	Ag Nanoparticles	29
3.3	Optical Setup	31
3.3.1	Laser System	32
3.3.2	Optical Parametric Amplifier	33
3.3.3	Noncollinear Optical Parametric Amplifier	33
3.3.4	Beam Pathway	35
3.3.5	Pulse Characterization	36
3.4	Data Acquisition and Controlling	37
3.5	Table of Instruments	38
4	One-Photon Photoemission	41
4.1	Introduction	41
4.2	Evolution of Density of States with Nanoparticle Size	42
4.3	Influence on Density of States by Cs Deposition	47
5	Two-Photon Photoemission	51
5.1	Photoemission Depending on Nanoparticle Size	52
5.2	Density of States of Silver Nanoparticles	56

5.2.1	Change of Spectral Shape with Photon Energy	56
5.2.2	Influence on Density of States by Cs Deposition	61
5.2.3	Discussion of One and Two-Photon Photoemission Results . . .	64
5.3	Plasmon Resonance Shift with Particle Size	68
5.4	NO Adsorption on Ag(111) and Nanoparticles	71
5.4.1	Ag(111)	71
5.4.2	Nanoparticles	74
6	Two-Colour Experiments	77
6.1	Rate-Equation Model	77
6.2	Variation of Pump-Probe Intensities	79
6.3	Two-Colour Correlation	83
7	Summary and Outlook	89
	References	92
	List of Publications	105
	Danksagung	106
	Lebenslauf	107

Chapter 1

Introduction

Photochemistry plays an essential role in many processes, e.g. in the conversion of light to chemical energy in photosynthesis or to electrical energy in a dye-sensitized solar cell [43]. As anode in these dye-sensitized cells usually TiO_2 is employed which is further in use for sun light driven water detoxification because of its high oxidation potential [7]. As the underlying electronic processes proceed on a femtosecond time scale, it was not until the development of ultrashort laser technology that they could be approached by scientific investigation. Recently, "coherent control" of molecular bond-breaking has been achieved by employing femtosecond pulse shaping in a feedback loop [23, 5, 126, 73].

Physico-chemical processes on surfaces that are involved in heterogeneous catalysis may be photoinduced, too. Thus, ultrashort laser spectroscopy has been used to study the electron dynamics on surfaces [99, 131, 60] as well as the photoinduced manipulation of substrate-adsorbate bonds [9, 117]. Further, the state selective detection of photodesorbed molecules revealed essential information about the desorption mechanism [2, 133]. In this regard, considerable effort has been dedicated to the investigation of the photodesorption mechanisms on oxide surfaces [1], employing both experimental [76, 88, 13] and theoretical methods [20, 57, 122, 21, 123, 62]. Recently, femtosecond laser pulses allowed the mediation of simple reactions on the surface [47, 19].

It is important to note, that surfaces do not only change the chemical activity of adsorbed molecules, as primarily exploited in heterogeneous catalysis, but may also facilitate the access by optical methods. As the optical excitation of surface plasmons becomes possible, the absorption probability of light may be drastically enhanced. This can be achieved by using e.g. nanoparticles of certain metals [63].

The excitation of surface plasmons in nanoparticles has been extensively studied over the last decade using various methods [68, 116, 32, 92, 69, 4]. In our group, plasmon excitation in silver and gold nanoparticles supported by various oxide films have been characterized by photon-scanning tunneling microscopy [90]. The optical excitation of plasmons leads to a field enhancement at the surface and therefore to an enhancement of nonlinear optical processes such as surface-enhanced Raman scattering (SERS) [58],

second harmonic generation (SHG) [29, 66], and multiphoton photoemission [69, 80, 85, 36].

Recently, an enhanced photodesorption cross section has been reported on substrates, which are known to provide the optical excitation of surface plasmons [24, 105, 65, 129]. However, the disposition of substrates to the optical excitation of plasmons is always accompanied by nanostructuring. This in turn may not only alter the material's catalytic activity [72], but also the respective electron dynamics [79] as well as the electronic structure due to confinement [93]. Thus, in order to determine the contribution of plasmon excitation to photodesorption, a detailed study of substrate properties has to be performed.

This thesis is intended as a fundamental investigation to experiments on the photodesorption of molecules, i.e. the simplest case of surface photochemistry relevant for catalysis. Silver nanoparticles supported by an alumina film have been used as model catalyst system and compared to a Ag(111) single crystal. Silver nanoparticles provide the optical excitation of the surface plasmon, i.e. the collective oscillation of conduction electrons. However, the specific interaction mechanism between plasmon excitation and adsorbate is not clear, especially since the established electric field at the surface is not supposed to have a direct influence on the desorption. In contrast, the common mechanism in photodesorption is desorption induced by electronic transition (DIET) [3, 77, 106]. Therefore, the interaction of the plasmon with the local density of states shall be investigated by using two-photon photoemission (2PPE) spectroscopy. This technique allows on one hand the excitation of the surface plasmon and on the other hand the probing of occupied and unoccupied states in the vicinity of the Fermi level.

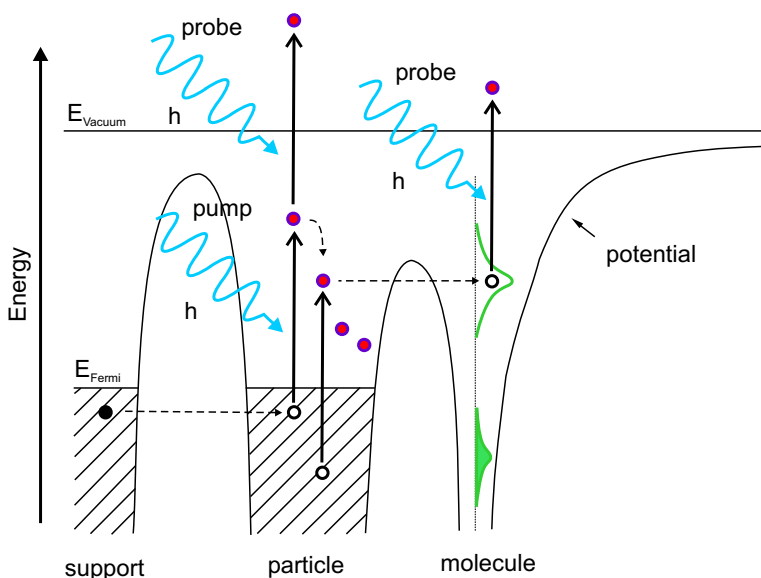


Figure 1.1: Sketch of two-photon photoemission on supported particles covered with molecules. A pumped electron excited in the particle may directly be probed by a second photon or transferred into an unoccupied orbital of the adsorbate. There it may induce the desorption of the molecule which may be controlled by a second probe photon.

In fig. 1.1 the 2PPE pump-probe mechanism is sketched also involving an electronic

transition to an unoccupied adsorbate orbital. Such a transition may induce desorption as will be described below.

If an electron, excited in the substrate (particle), is scattered into an unoccupied orbital of an adsorbed molecule generally the equilibrium bond length to the surface changes. By compensating this change the molecule starts to move and may gain enough energy to leave the surface. This gain in kinetic energy obviously depends on the excited state lifetime. Therefore, limiting values of the DIET cross section are the excitation probability of substrate electrons and related dynamics. This leads to the central issues which will be addressed in this thesis:

- Density of states of the substrate
- Role of plasmon excitation
- Influence of adsorbates on the above values
- Electron dynamics

Of particular interest in the present work is the investigation of the density of states of the substrate. The density of states is known to influence not only the catalytic properties of the substrate [96, 44], but also determines the light absorption due to electronic transitions therein as well as the related electron dynamics [95]. By employing one-photon photoemission (chapter 4) and two-photon photoemission (section 5.2) spectroscopy, the occupied and unoccupied density of states depending on particle size has been investigated. The results obtained can be explained by phase accumulation models of surface states and quantum well states, alternatively. By comparison to the surface state on Ag(111) and a quantum well state simulation for a realistic particle size distribution, the conformance of the competing models is discussed.

Especially with respect to 2PPE, various decay channels of the plasmon excitation have been proposed [80, 111]. These are considered as essential for an understanding of a plasmon induced desorption. As plasmon excitation is involved in all 2PPE results presented in chapter 5, a consistent picture of the plasmon decay is established by gathering the respective information of each section. Finally, the obtained picture is confirmed by two-colour experiments in chapter 6, revealing the magnitude of the electric field enhancement at plasmon resonance.

As adsorbate NO is chosen which is widely used in photodesorption experiments, especially since its state selective detection is possible [2, 133]. Upon adsorption, NO is found to have considerable influence on the plasmon excitation on rough Ag(111) and silver nanoparticles (section 5.4).

As mentioned above, the unoccupied density of states is expected to have considerable influence on the excited electron lifetime [95]. This is investigated by employing time-resolved two-colour experiments on nanoparticles in chapter 6. Further, the relaxation dynamics of excited electrons could be retraced, giving evidence for the major decay channel of the plasmon excitation.

The experimental results are arranged in chapters according to the methods being used, which are shortly introduced in each case. In chapter 4 the 1PPE results are presented, followed by the 2PPE results in chapter 5, and two-colour experiments in chapter 6. The experimental part is preceded by a review of the relevant properties of silver nanoparticles (chapter 2) and a subsequent description of the experimental setup (chapter 3), where special attention is dedicated to the self-built noncollinear optical parametric amplifier. It enables shorter pulses and makes one-photon photoemission spectroscopy possible as well as two-colour experiments. Finally, a summary is given in chapter 7.

Chapter 2

Properties of Silver Nanoparticles

2.1 Electronic States

Large nanoparticles ¹, which are used in this thesis, are in general supposed to exhibit bulk-like structure if crystalline ordered. Due to quantization effects, however, this structure may split into distinct states. Furthermore, especially for silver particles grown on alumina [93] and graphite [8, 48], a predominant disordered atomic structure has been reported.

Therefore, for an interpretation of the experimental findings, we present on one hand a model for surface states assuming bulk-like band structure without an influence of quantization effects. On the other hand, as an alternative interpretation, a band structure corresponding to an amorphous particle structure is considered. Due to confinement effects this band splits into distinct states called quantum well states.

2.1.1 Surface States

At the surface the periodicity of a crystalline bulk structure ends leading to a break in translational symmetry. This allows the existence of states which do not fulfill the requirements of an infinite periodic bulk. Here we will focus on the Shockley surface state, named after Shockley who worked out the criteria for its existence [112]. For a detailed review on experimental and theoretical investigations of surface states see [33]. The Shockley surface state, in the following simply called surface state, has not only been observed at bulk surfaces but also on thin films with down to monolayer thickness [98, 27, 102], as well as on nanoparticles [71, 8]. As it extends into the vacuum, it is considered to influence the adsorption of molecules if occupied [17, 75]. It was found that the position of this state on bulk surfaces could be well reproduced by a multiple-reflection theory of surface state formation [113]. This finally condensed in the so called phase accumulation model.

¹Here we make use of the term "large" denoting more than 500 atoms per particle [63].

Inside the bulk the existence of states within the band gap is not allowed. The k -wave vector then becomes complex leading to a continuous exponential increase or decrease of the wave function in the associated direction, violating the boundary conditions. At the surface, however, an increasing wave function may experience a limitation by the vacuum barrier. The phase accumulation model deals with the corresponding surface state electrons residing primarily between the outermost atomic layer and the vacuum barrier, described by an image potential in fig. 2.1. Associated Bloch waves depend on the position inside the band gap and are reflected by the vacuum barrier after leaving the crystal. The reflection induces a phase shift and leads to interference with the original wave, which is considered to result in a state as soon as the interference is constructive. The determining parameters will be discussed below, according to [75].

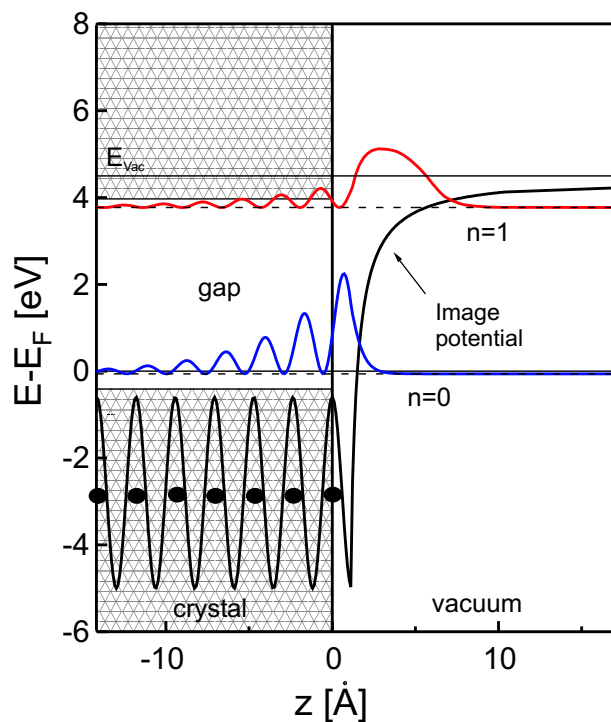


Figure 2.1: Potential and squared wave functions of surface state ($n=0$) and first image state ($n=1$) on Ag(111) according to the phase accumulation model. Electrons are trapped between the crystal surface and the vacuum barrier (Image potential).

In fig. 2.1 the squared wave functions of the surface state and of the first image state on Ag(111) are depicted, both obtained by the phase accumulation model. While the surface state is crystal-induced, i.e. related to bulk properties, image states have their origin in the free electrons at a metal surface. If we position an electron at the vacuum side it will induce a mirror charge with positive sign inside the bulk. Thus, in analogy to the hydrogen atom, a Rydberg-like series of image states will result,

provided the states lie within the surface projected band gap. For an image potential the Schrödinger equation in the barrier region is equivalent to that for the radial part of the hydrogen problem [40] with an effective charge $Z_{eff} = \frac{1}{4}$. Consequently the energies of these high-lying image states are approximately given by

$$E_{Image} \approx E_{Vac} - \frac{Z_{eff}^2}{2(n+a)^2} = E_{Vac} - \frac{0.85 \text{ eV}}{(n+a)^2}, \quad n = 1, 2, 3, \dots, \quad (2.1)$$

where E_{Vac} denotes the vacuum energy and the quantum defect a accounts for the altered boundary condition at the surface. In analogy to the hydrogen case the image states are labelled by quantum numbers $n \geq 1$, while the low-lying surface state is labelled by $n = 0$.

As can be seen in fig. 2.1 for the $n = 0$ state the electron density peaks right in front of the top layer while for the $n = 1$ state the electron density peaks several Å in front of the surface. The $n = 0$ state near the bottom of the gap exhibits nodes near the atomic positions, while the $n = 1$ state near the upper edge is shifted. This is due to the fact that the gap is Shockley-inverted: Bloch waves are p_z -like at the bottom and s-like at the top. If we pass the gap from bottom to top their character changes slightly resulting in a phase shift at the crystal surface.

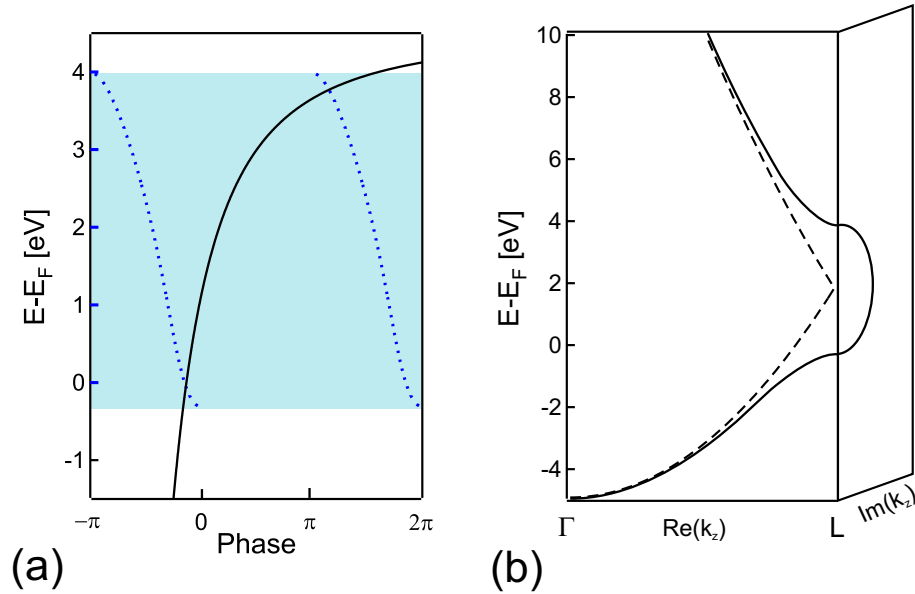


Figure 2.2: (a) Phase shift induced by the image potential (solid curve) and the negative of the phase shift due to the band gap (dotted curves). The band gap is highlighted. At the crossing points phase shifts add to a multiple of 2π indicating the position of a state. (b) Models of the sp-band dispersion in Ag(111) direction. The dashed curve represents a free electron dispersion, the solid curve a nearly free electron dispersion. In the latter case a gap opens up, giving a good approximation to the actual Ag(111) dispersion around the L-point.

To obtain the state positions in fig. 2.1, we consider the following. Bloch waves leaving the crystal will be reflected at the vacuum boundary, described by an image potential. The resulting phase shift Φ_{Image} can be approximated by [74]

$$\Phi_{Image} \approx \pi \left(\sqrt{\frac{3.4 \text{ eV}}{E_{Vac} - E}} - 1 \right) \quad (2.2)$$

If the reflected wave interferes constructively with the incoming wave, which itself shows an energy dependent phase shift as discussed before, a state is expected. The calculated phase shifts are depicted in fig. 2.2(a). The solid curve belongs to the phase shift due to the image potential, the dashed curves to the negative crystal induced phase shift. Consequently, the intersection points mark the position of a state where the two phase shifts add to a multiple of 2π .

In fig. 2.2(b) approximations to the sp-band dispersion in Ag(111) direction are shown. The nearly free electron dispersion depicted by the solid curve is a good approximation to the bulk band structure. It has been used for various calculations based on the band structure of Ag(111) around the L-point [101, 83] and was also used in this case to determine the crystal induced phase shift. For proper matching of the sp-band dispersion around the L-point for an interlayer distance of 2.36 Å the band bottom was fixed at -4.9 eV. The effective electron mass has only implicit character and is taken as unity. For details of the proceeding see [75].

The gap which opens up for the nearly free electron dispersion at the L-point in the real plane is closed in the imaginary plane. The imaginary part represents the constant for the exponential decay of the surface state into the bulk. The more the state is located at the band edges the further its wave function extends into the crystal.

To conclude we have seen that the phase accumulation model provides essential insight into the nature of the surface state. Its position depends on one hand on the work function induced phase shift, i.e. on the work function itself (see equ. 2.2), and on the other hand on the crystal induced phase shift, i.e. on the band structure. A lowering of the work function leads to a shift of the state to lower energy, an increase of the work function vice versa. For a shift of the SP-band edges an equivalent behaviour is expected.

2.1.2 Quantum Well States

If the structure under investigation is very narrow, i.e. several atoms in thickness, we have to consider quantization effects ². In our case silver is deposited on an alumina support which exhibits a pronounced band gap from -5 eV up to 3 eV. At these energies, electrons inside the film are confined between the alumina gap and the vacuum boundary, expressed by an image potential. This confinement leads to a quantization of the sp-band of silver and to corresponding quantum well states (QWS), depending

²Lateral confinement effects as reported in [71, 49] are not taken into account.

on film thickness. QWS have been extensively studied especially in Ag films on various supports [35, 97, 109, 30, 95]. These results could be well described by a phase accumulation model of QWS which will be introduced below.

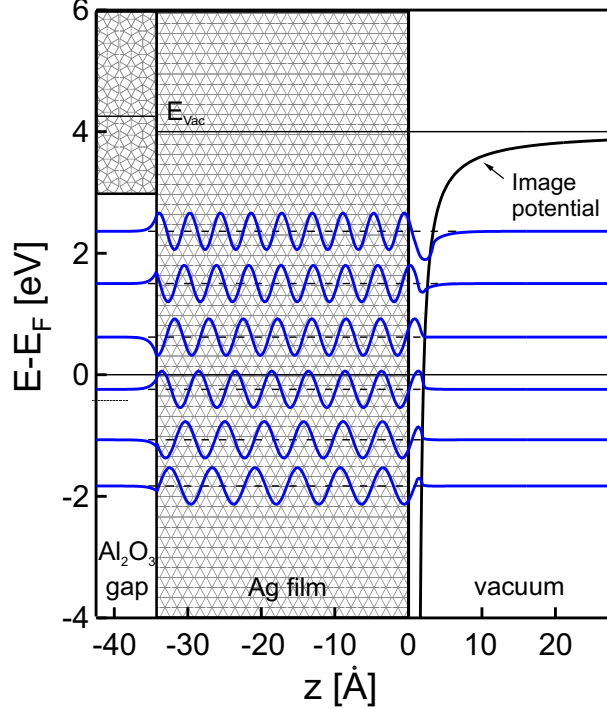


Figure 2.3: Wave functions of Quantum Well States in a 14 ML thick silver film. Electrons are confined perpendicular to the surface by the vacuum boundary (Image potential) and the Al_2O_3 band gap of the support. The Ag-band structure is assumed to be free electron like due to disordered atomic structure. Consequently, no sp-band gap exists for the silver film.

We consider an electron propagating inside the film perpendicular to the surface. It may be reflected at one side by the image potential and at the other side by the alumina gap. At each boundary it suffers a phase shift Φ_{Image} and $\Phi_{Support}$, respectively. For a film thickness Nd , where N denotes the number of monolayers and d the interlayer distance, a standing wave is established in dependence on the wave vector k . After one traveling cycle the phase then should stay the same leading to the following equation:

$$\Phi_{Image} + 2kNd + \Phi_{Support} = 2\pi n, \quad (2.3)$$

where n enumerates the resulting states. The corresponding wave functions are depicted in fig. 2.3 for $N=14$ ML and $d=2.36$ Å, the interlayer distance of Ag(111). As experimental data suggested, a free electron like sp-band dispersion was assumed, illustrated in fig. 2.4(b) by the solid line. This approach can be understood as due to a disordered atomic structure of silver aggregates excluding the formation of a crystalline

band structure. For matching to the experimental data the band bottom was adjusted to -6.3 eV with an effective electron mass of unity³.

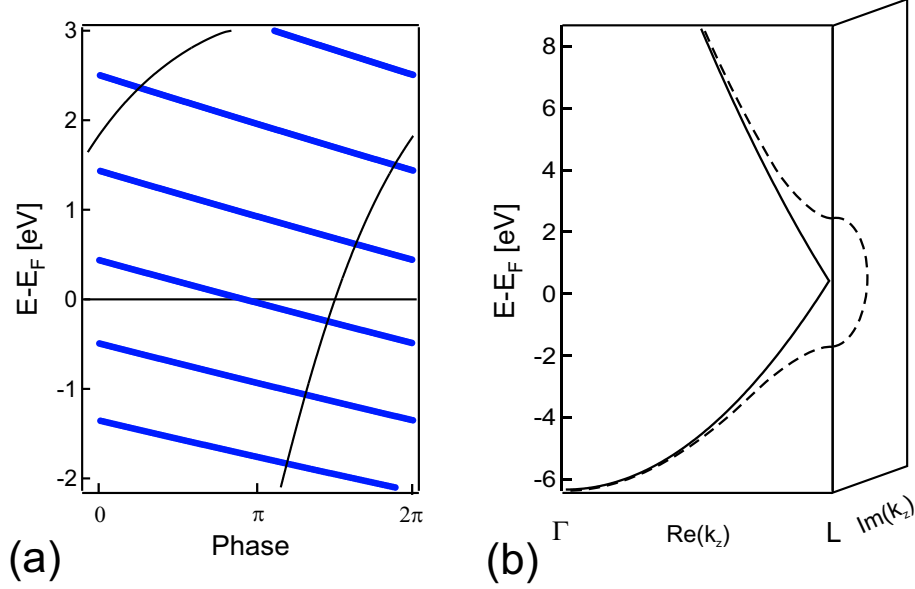


Figure 2.4: (a) The curved line represents the total phase shift induced at the boundaries of a Ag film. The straight lines represent the negative phase resulting from 14 ML film thickness and free electron like dispersion. Crossing points indicate the positions of quantum well states. (b) The solid line depicts a free electron like dispersion as being used in (a). For an ordered crystalline structure a nearly free electron like dispersion would be expected as indicated by the dashed line.

In fig. 2.4(a) the phase shift induced by the film boundaries as the sum of Φ_{Image} and $\Phi_{Support}$ is given by the curved line. Φ_{Image} has already been introduced by equation 2.2 and $\Phi_{Support}$ can be approximated by [114]

$$\Phi_{Support} = 2 \arcsin \sqrt{\frac{E - (-5 \text{ eV})}{3 \text{ eV} - (-5 \text{ eV})}} - \pi, \quad (2.4)$$

where 3 eV denotes the upper gap edge and -5 eV the lower gap edge of the alumina film. Also shown in fig. 2.4(a) is the negative phase due to the term $2kNd$ for $N=14$ ML as indicated by straight lines. The intersection points indicate the positions of quantum well states (QWS). It can be seen that also beyond 3 eV a crossing point exists. However, this state is no more confined by the alumina gap and is therefore expected to be quenched [84, 82].

To summarize we have seen that both surface state and quantum well states depend on the work function. Surface states exist inside a band gap, QWS only exist outside

³Depending on binding energy, a deviating effective mass for individual QWS was found [109], which, however, is not included in the simple model described here.

the gap. Therefore a major part of the surface state electrons reside outside the bulk while QWS electrons preferentially reside inside the bulk with only a small amount spilling over into the vacuum.

2.2 Plasmon Excitation

A plasma oscillation in a metal is a collective oscillation of the conduction electrons against the positive ion cores. The corresponding quantum is called plasmon. One differentiates between bulk plasmon and surface plasmon. The bulk plasmon denotes electron fluctuations propagating as longitudinal waves inside the bulk. They cannot couple to transversal waves as light.

Surface plasmons are collective charge density fluctuations at the metal-vacuum or metal-dielectric interface. The solution of the Maxwell equations leads to the corresponding dispersion relation. The real part of the wave vector $k_x(\omega)$ parallel to the surface is then given by

$$k_x(\omega) = \frac{\omega}{c} \sqrt{\frac{\varepsilon(\omega)\varepsilon_d}{\varepsilon(\omega) + \varepsilon_d}}, \quad (2.5)$$

where $\varepsilon(\omega)$ denotes the real part of the dielectric function and ε_d the adjacent medium. For a free electron system and neglect of damping, $\text{Re } \varepsilon(\omega)$ is given by the Drude-theory as

$$\varepsilon(\omega) \approx 1 - \frac{\omega_p^2}{\omega^2}, \quad (2.6)$$

with the volume plasmon frequency

$$\omega_p = \sqrt{\frac{ne^2}{\varepsilon_0 m_e}}, \quad (2.7)$$

where n denotes the electron density.

The surface plasmon dispersion of equation 2.5 is depicted in fig. 2.5 by the solid line. It approaches the light line for small k_x but remains larger eluding the coupling to light. At large k_x , ω approaches

$$\omega = \frac{\omega_p}{\sqrt{1 + \varepsilon_d}}. \quad (2.8)$$

In this region $\varepsilon(\omega) < -\varepsilon_d$, leading to a real value of k_x . The solution for k_z perpendicular to the surface exhibits an exponential decrease due to the imaginary value in that direction. Therefore, this region is denoted as bound modes. At $\varepsilon(\omega) \geq 0$, i.e. $\omega \geq \omega_p$, k_z becomes real leading to radiative modes. For details see [104].

There are possibilities to couple surface plasmons to light. By using a prism we may alter the k -vector of the exciting light proportional to the reciprocal optical density of the prism [61]. Another way is to use a grating which adds a reciprocal grating vector

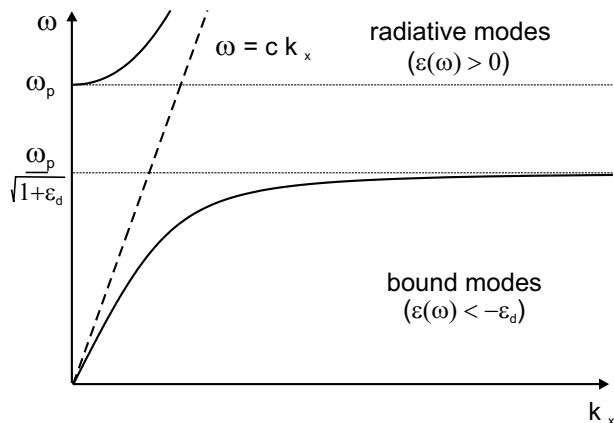


Figure 2.5: Dispersion relation of light (dashed line) and surface plasmon (solid line). ω_p denotes the volume plasmon frequency. Although surface plasmon and light concern transversal waves they elude coupling due to their different dispersion relations.

to the k -vector upon diffraction [64]. In general the grating may also be replaced by a rough surface. The reciprocal grating vector then is given by the Fourier components of the corrugation.

2.2.1 Surface Plasmon in Silver Nanoparticles

On metal nanoparticles the excitation of plasmons is also possible, as has been reported for various metals [63]. For Au and Ag the plasmon resonance is situated in the visible region. In the case of Ag the resonance position is clearly separated from the interband transition leading to a pronounced and narrow shape [28]. Its width is determined by the lifetime as measured on single nanoparticles by photon-STM [92].

The solution of the Maxwell equations with spherical boundary condition has been derived by G. Mie in 1908 to explain the colour of stained glass and solutions of metal colloids [81]. A derivation of the theory can be found in several text books, e.g. [63, 55, 18]. Therefore, the corresponding theory is called Mie-theory and the plasmon excitation Mie-plasmon. Often this resonance is also called surface plasmon because of the essential influence of the surface on its properties, despite the fact that for the nanoparticles all conduction electrons participate in the oscillation. In the following, we will adopt the latter term. The oscillation can be understood as a resonant screening of an external (light) field leaving the field inside the nanoparticle uniform. Because of its resonant character the oscillation may result in a polarization and an electric field exceeding that of the exciting light, often referred to as field enhancement. Such a field enhancement can also be induced by the particle shape [41]. It should be most pronounced at edges where the curvature of the particle is high.

In this thesis, silver nanoparticles aggregate on a NiAl substrate which is covered by a 5 Å thick alumina film (sec. 3.2.2). For that reason particles become elliptical,

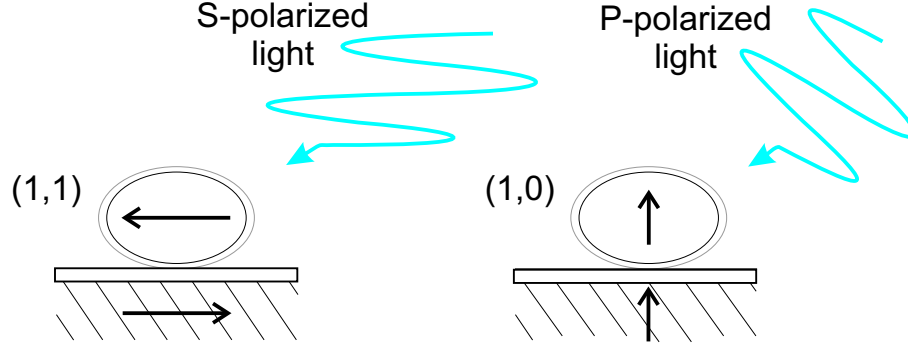


Figure 2.6: Plasmon oscillations along the principal axes of a silver nanoparticle. The $(1,1)$ -mode, excited with s-polarized light, is damped by its image dipole in the support. For the $(1,0)$ -mode, excited with p-polarized light, the image dipole superposes constructively.

breaking the degeneracy of a sphere. Moreover, the resulting principle axes are distinguished by the interaction of the plasmon excitation with the substrate, depicted in fig. 2.6. The plasmon oscillation along the $(\pm 1,1)$ -axes parallel to the substrate's surface induces a mirror dipole in the NiAl-alloy pointing to opposite direction. Therefore, the plasmon oscillation in that direction will be hindered resulting in a shorter lifetime and lower resonance energy [42]. For the $(1,0)$ -mode perpendicular to the surface the opposite applies. The induced dipole superposes constructively supporting the oscillation.

The quasistatic Mie-theory does not contain an explicit size dependence. Deviations occur for large particles due to retardation effects when the incident field may no longer be treated as uniform. For spherical particles this leads to the excitation of multipole resonances. The dipole resonance is usually red shifted and broadened as a consequence of the enhanced radiation damping which grows with the volume of particles.

As a rule of thumb, the quasistatic theory works well for particle sizes up to 10 nm [63]. In this range different mechanisms are relevant. Particles smaller than the bulk mean free path length of electrons experience an enhanced damping due to surface scattering [31, 124]. In silver this is partly compensated by the growing importance of the spill-out region at the surface. The electrons in the free electron like 5s-band extend further into the vacuum than the tighter bound 4d electrons and their mutual coupling is weakened [10]. This leads to a blue shift of the plasmon resonance with decreasing particle size. Another explanation was proposed by Cai et al. [25] and alternatively by Lerme et al. [70]. They detected a lattice contraction for smaller silver particles and attributed the blue shift to the increasing charge density. A contrary effect of the spill-out is the reduced electron density which is in silver of minor importance.

Chapter 3

Experimental Setup

The experimental apparatus has originally been designed to combine photodesorption and photoemission facilities. Therefore, the design differs from common photoemission setups [86], as will be mentioned in the text. As this thesis is intended as a fundamental study to photodesorption experiments it will be focussed on photoemission spectroscopy.

The experimental setup can be divided into two main parts, given by the femtosecond laser system, described in detail in sec. 3.3, and the UHV-chamber where the preparation of samples and photoemission experiments were performed. The UHV is necessary to avoid a fast contamination of the sample during preparation and experiment. Furthermore, the mean free path length of electrons should be > 1 m to avoid scattering losses.

For photoemission measurements femtosecond pulses made by a commercial laser system from Spectra Physics are frequency converted, compressed in time or may be delayed before hitting the sample. Pulses are characterized by a grating spectrometer and autocorrelation methods.

In the following sections the various parts of the setup are described. For a better legibility the exact labeling of each part is given in sec. 3.5 at the end of this chapter.

The experiments described in chapter 4, 5, and 6 were performed during the last two years on a UHV device built up and described in detail in the thesis of Christoph Rakete [105]. For the UHV part only small changes were performed as will be mentioned in the text. The optical setup was extended by a self-built noncollinear optical parametric amplifier which enables shorter pulses, one-photon photoemission (sec. 4), and two-colour experiments (sec. 6).

3.1 UHV System

The UHV system consists of two chambers with cylindrical shape and 40 cm in diameter. They are vertically connected by a lead-through of 10 cm diameter which can be closed by a valve. Diverse flanges enable the installation of components. The

upper part, serving for sample preparation, consists of stainless steel and is pumped by a turbo molecular pump. Another pump of the same type pumps the measurement chamber below, which is built of μ -metal to shield electrons from the earth magnetic field. In this chamber additionally a ion-getter pump and a titanium sublimation pump are installed. Both turbo pumps are pumped by a forepump which delivers 10^{-3} mbar, monitored by a Pirani gauge. After 24 h baking at 140°C a base pressure of $< 10^{-10}$ mbar is achieved, monitored by ion gauges in each chamber.

Samples are mounted on a liquid nitrogen cryostat (see sec. 3.1.1) which allows cooling down to 83 K. The reservoir can additionally be pumped by a forepump to reduce the boiling point of nitrogen resulting in 77 K.

The cryostat is fixed on a x/y/z-manipulator which enables the positioning of the sample horizontally ± 2.5 cm and vertically 42 cm from one chamber to the other. A rotational lead-through, differentially pumped, enables the rotation of the sample in order to position it in front of each preparation or diagnostic device.

Diverse components of the chamber are depicted in fig. 3.1.

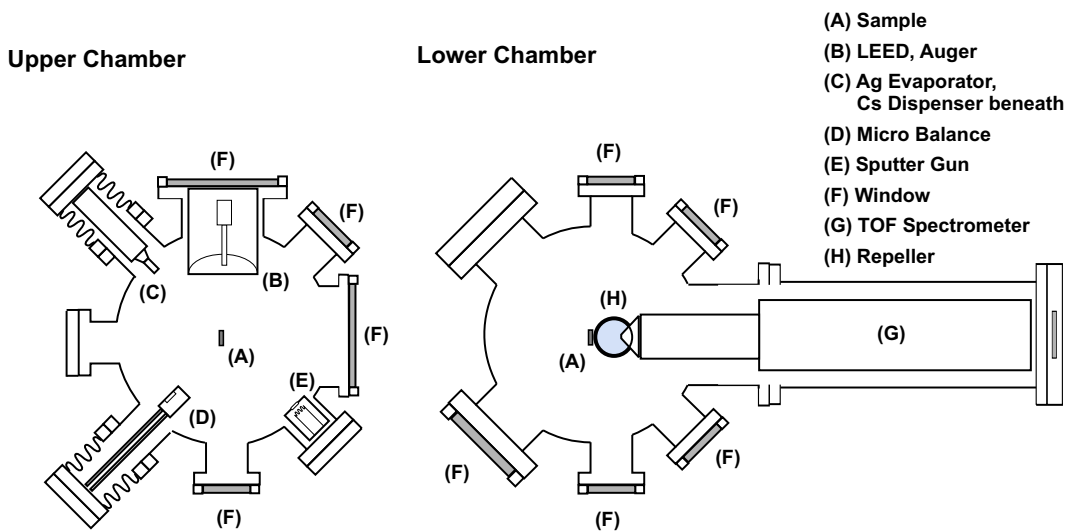


Figure 3.1: Sketch of the vacuum chamber with its upper part serving for sample preparation and the lower part for measuring purpose (Cut along the horizontal plane).

Samples are cleaned by sputtering with Ar^+ ions created and accelerated by a sputter gun. The cleanness of the sample can be checked by Auger spectroscopy, the crystal structure by low energy electron diffraction (LEED), both comprised in one device. Furthermore, there is a silver evaporator which can be calibrated by a micro balance and a cesium dispenser which has been installed during this thesis.

The essential device is the time-of-flight (TOF) spectrometer. Its calibration procedure and resolution is described in sec. 3.1.2. The laser beam enters the chamber through a fused silica window and hits the sample in front of the orifice of the spectrometer under an angle of 45° . The reflected light leaves the chamber by passing

through another fused silica window. Between sample and TOF-spectrometer a repeller is located consisting of two horizontal molybdenum meshes, one above and one below the electron flight path. Its purpose is the detection of ionized photodesorbed molecules but is not in use here. Therefore the meshes, suspected to charge up due to their graphite coating, were replaced by titanium plates.

For sample preparation and adsorption experiments each chamber is equipped with a leak valve.

3.1.1 Sample Mount

The sample mount was designed to hold two crystals pointing with their polished surfaces to opposite direction. Here we used a Ag(111) crystal and a NiAl(110) crystal throughout the experiments, both exhibiting 3 mm thickness and 10 mm in diameter. By rotating the manipulator we can select one crystal for preparation or measurement. In the vicinity of the samples only non-ferromagnetic metals were used. This is to avoid on one hand magnetic deflexion of photoelectrons and on the other hand charging effects due to non conducting parts. Samples were spot welded on 2 mm thick molybdenum rods by using tantalum wire as connection. The rods were mounted to appropriate fittings being part of a Sapphire crystal. Sapphire is an insulator which exhibits high heat conductivity at low temperature and poor heat conductivity at high temperature. It is in good thermal contact to a nitrogen reservoir and therefore provides appropriate cooling of the sample if needed. If the sample is heated the Sapphire acts contrarily, again supporting the desired effect. The heating is realized by a tungsten filament at the rear side of each crystal. For small temperature increase radiative heating is applied, for high temperature, i.e. > 800 K, heating by electron impact due to high voltage is used. For temperature check each crystal is connected to a thermocouple of type E(NiCr-CuNi).

The cryostat where the Sapphire is mounted consists of a rigid 50 cm tube which is closed at the bottom and open at the top, providing the insertion of liquid nitrogen. Its upper part is made of stainless steel because of its stability and poor heat conductivity. The lower part consists of copper which is non-ferromagnetic and exhibits high thermal conductivity. To avoid warming up due to heat radiation the lower part is gold-plated.

3.1.2 Time-Of-Flight Spectrometer

The kinetic energy of electrons is generally determined either by deflection due to defined electric fields or by determination of their time of flight over a known distance. The latter method is distinguished by high resolution at low energy and high transmittance, and is described in the following.

Setup

The time-of-flight spectrometer was designed and built up by Christoph Rakete [105]. The laser pulse hits the sample at 45° incidence, facing the spectrometer entrance in normal direction. Resulting photoelectrons have to pass through a repeller consisting of two horizontal tantalum plates of 5 cm in diameter and 1.5 cm in distance which are on ground potential. This repeller was designed for the detection of photodesorbed molecules and is not in use here. After ≈ 5 cm flight path the electrons enter the spectrometer through a 5 mm orifice. After passing a drift tube of 60 cm, which is terminated by a molybdenum mesh on ground, they are accelerated by another mesh on 500 V to a double multi channel plate (MCP) in Chevron arrangement in 5 mm distance. An impinging electron initiates there an electron cascade which is collected by an anode at the rear side. The resulting pulse is finally transformed by a capacitor before leaving the UHV.

The sample can be set on voltage. The spectrometer is surrounded by μ -metal to shield magnetic fields from outside and consists of non magnetic parts inside. To avoid perturbation fields inside due to altering work function, repeller plates and spectrometer were coated with graphite.

Time-to-Energy Conversion

The TOF-spectrometer provides the determination of photoelectron energies. This is performed in normal direction to the sample's surface. Angular resolved measurements, which are also feasible with this setup, are not applied here. For determination of the electron kinetic energy, we have to know the flight time t_{flight} of electrons starting with the laser pulse excitation at the sample and ending with the arrival of an emitted electron at the detector. The flight path l is in good approximation field free [105], leading to the simple expression:

$$E_{kin} = \frac{1}{2}m_e \left(\frac{l}{t_{flight}} \right)^2 + e\Delta U, \quad (3.1)$$

where ΔU denotes the potential difference between sample and spectrometer. It includes the bias voltage U_{bias} which may be applied on the sample and the difference in work function $\Delta\Phi$ between sample and spectrometer:

$$e\Delta U = \Phi(spectrom.) - \Phi(sample) + eU_{bias} \quad (3.2)$$

$$= \Delta\Phi + eU_{bias} \quad (3.3)$$

The flight time t_{flight} differs from the measured time t_{exp} by an electronic delay time t_0 . This is due to a delay between the start pulse, given by a photodiode which is triggered by the incident laser pulse, and the stop pulse, generated in the MCP-detector, which has to pass several electronic steps, depicted in fig. 3.2. Equation 3.1 then changes to

$$E_{kin} = \frac{1}{2}m_e \left(\frac{l}{t_{exp} - t_0} \right)^2 + \Delta\Phi + e\Delta U_{bias} \quad (3.4)$$

To transform the detected time of flight distribution $\tilde{N}(t)$ into kinetic energy distri-

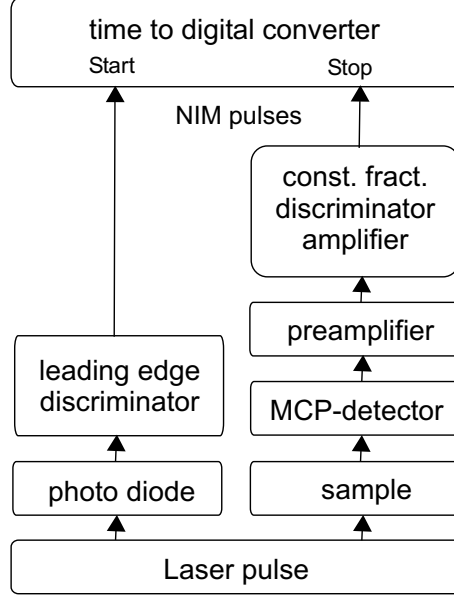


Figure 3.2: Detection chain for time of flight.

bution $N(E_{kin})$ we have to take into account the conservation of particle number per interval, i.e.

$$\tilde{N}(t) \cdot dt = N(E_{kin}) \cdot dE_{kin}. \quad (3.5)$$

With

$$\frac{dE_{kin}}{dt} = -\frac{m_e l^2}{(t - t_0)^3} \quad (3.6)$$

we end up with

$$N(E_{kin}) = \tilde{N}(t) \frac{(t - t_0)^3}{m_e l^2} \quad (3.7)$$

Calibration

For determination of the kinetic energy of photoelectrons there are some unknown parameters like t_0 , $\Delta\Phi$, and l . l can be estimated to 654 ± 5 mm []. If we solve equ. 3.4 for t_{exp} we get

$$t_{exp} = l \cdot \frac{1}{\sqrt{\frac{2}{m_e}(eU_{bias} + E_{kin} + \Delta\Phi)}} + t_0. \quad (3.8)$$

Now we take time of flight spectra for different values of U_{bias} . By plotting distinct points of the recorded spectra like the vacuum cutoff or the surface state on Ag(111) versus values of t_{exp} obtained with the above equation with $l = 1$ m and $t_0 = 0$, we should get a linear dependence if equ. 3.4 is true. This however depends on the proper

choice of $E_{kin} + \Delta\Phi$. If this is the case, the resulting slope equals l and the intersection with the time-axis determines t_0 .

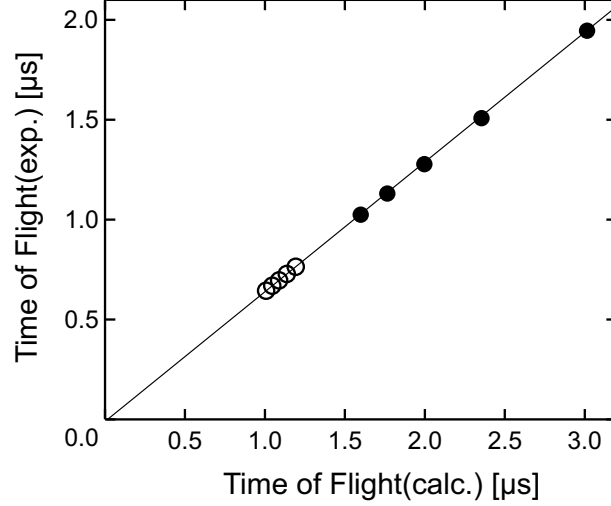


Figure 3.3: Spectrometer calibration. The measured flight time versus calculated flight time is plotted for varied U_{bias} and fixed kinetic energy. Only if the proper kinetic energy value is chosen we see a linear dependence, where the slope is determined by the flight length l and the intersection with the time axis marks the delay time t_0 .

The value of $E_{kin} + \Delta\Phi$ has been varied iteratively for various values of U_{bias} (-0.1 V, -0.3 V, -0.5 V, -0.7 V, and -0.9 V) at $h\nu=3.15$ eV to optimize linearity. The result is shown in fig. 3.3. Open circles mark the surface state feature and closed circles the vacuum cutoff. At the vacuum cutoff $E_{kin} = 0$, revealing $\Delta\Phi=0.21$ eV, $t_0=-11$ ns, and $l=650$ mm which is close to the estimated value. The surface state electrons have $E_{kin}=1.68$ eV. The Fermi level was determined by employing s-polarized light on Ag(111) localizing the surface state at -50 meV. This value is in good agreement with the literature value of -63 meV at 30 K [107], leading to a work function of Ag(111) of 4.55 eV, which is also close to literature values of around 4.5 eV [86]. The work function of the spectrometer is then 4.34 eV, which is between the value of another graphitized spectrometer [78] of 4.2 eV and the work function of pure graphite of 4.5 eV. The resulting work function of the alumina film with 4.3 eV is close to the value of 4.4 eV obtained by UPS measurements, exhibiting less accuracy.

Energy Resolution

Systematic deviations with an influence on the absolute kinetic energy are:

- Deviation of the flight length l of ± 3 mm
- Uncertainty for the delay time t_0 of ≈ 3 ns

- Neglect of the acceleration in front of the sample. Estimated error: 10 meV

The mean systematical error can be estimated by

$$\Delta E_{kin}^{syst} \approx \sqrt{\left(\frac{2\Delta l}{l} E_{kin}\right)^2 + \left(\frac{2\Delta t_0}{t_{exp} - t_0} E_{kin}\right)^2 + (0.01 \text{ eV})^2} \quad (3.9)$$

$$= \sqrt{\left(\frac{2\Delta l}{l} E_{kin}\right)^2 + \frac{8E_{kin}}{m_e l^2} (\Delta t_0 E_{kin})^2 + (0.01 \text{ eV})^2} \quad (3.10)$$

With this, a kinetic energy between 1 eV and 4 eV leads to a systematical error of 1.5 %.

The statistical error is responsible for the broadening of peaks and may be determined by

- Uncertainty for the flight length l due to the angular acceptance of the detector of ≈ 0.2 mm
- Field inhomogeneity inside the spectrometer
- Jitter of the applied sample potential U_{bias}
- Time resolution of the TDC of 2 ns.

The above contributions can hardly be assessed theoretically. As a measure for the spectral resolution we can rather use the width of the vacuum cutoff. It is independent of the spectral width of laser pulses and is only determined by the inhomogeneity of the sample's work function and the spectrometer resolution. The width of the vacuum cutoff is here ≈ 60 meV giving a lower limit for the resolution. The vacuum cutoff is also employed for the adjustment of U_{bias} . It was best mapped with a potential difference of 0.5 V between sample and spectrometer. At lower potential the vacuum edge becomes broader while at higher potential the intensity for low energy electrons inflates. Furthermore, a low bias voltage U_{bias} leads to higher time resolution and lower inhomogeneity of the electric field.

There are two effects due to intensity that may falsify the spectra. One is called space charging and leads to a spread of the resulting TOF spectra caused by mutual coupling of electrons on their flight to the detector. Another is the pile-up effect and is due to the TDC. If the number of electrons arriving at the detector is too large, high energetic electrons will preferentially be detected as they come first. This effect is partially circumvented by a multi-hit device which is able to count five stop pulses for one start pulse. During experiments a maximal mean count rate of two events per laser shot was assured. Furthermore the spectral shape was checked to be independent of intensity.

3.2 Sample Preparation

3.2.1 Ag(111)

A newly cut and polished silver crystal had to undergo up to 50 sputter-annealing cycles. A cycle starts by sputtering i.e. the cleaning of the surface by bombardment with Ar^+ ions (at 250°C , 500 eV , $3\ \mu\text{ A}$ ion current, 20 min) at an angle of $\pm 20^\circ$, varied after each cycle. Sequential annealing at $450\text{-}500^\circ\text{C}$ for 20 min leads to smoothing of the surface due to an enhanced mobility of surface atoms. A higher temperature may not only lead to melting but before to roughening due to a restructuring of the crystal. The procedure is repeated until no impurities were detected by Auger spectroscopy. The crystal structure was checked by LEED and the width and height of the surface state on Ag(111). Also the amount of hot electrons in two-photon photoemission gives a measure of the surface roughness.

Before each experiment the crystal was cleaned by applying two cleaning cycles.

3.2.2 Ag Nanoparticles

Ag nanoparticles are grown on an alumina film which is achieved by oxidation of a NiAl(110) crystal. Its preparation procedure and properties are well known and have been subject of intense studies [52, 12]. It exhibits a large band gap from -5 to 3 eV and is chemically inert. An oxide film grown on a metal provides access by electron spectroscopy methods since charging effects are avoided. Photoemitted electrons are replaced by electrons of the bulk. Similar approaches are Ag nanoparticles grown on graphite [129, 48, 100] or on oxide monocrystallites where the surface is permanently neutralized by spraying with slow electrons [68].

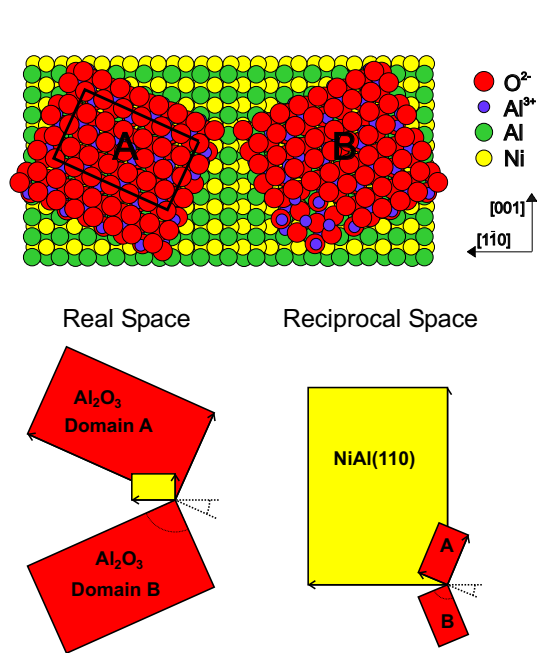


Figure 3.4: On top: Structure of $\text{Al}_2\text{O}_3/\text{NiAl}(110)$ with rotational domains A and B. Bottom: Corresponding unit cells in real and reciprocal space.

from known alumina structures but resembles the γ -modification. The film offers two rotational domains tilted against each other by 48° and against the NiAl-structure by 24° (see fig. 3.4). This causes line defects at domain boundaries. A second species of line defects is due to the fact that the ratio of lattice constants of film and support is not an integer. This mismatch leads to antiphase domain boundaries within each rotational domain resulting in a mean extension of around 100 \AA .

For cluster preparation silver is evaporated from a molybdenum oven by electron impact. The resulting deposition rate is around 1 \AA per minute which is calibrated before each preparation by a micro balance. On the alumina film silver atoms are rather mobile at room temperature nucleating preferentially at domain boundaries or step

A newly polished NiAl crystal had to undergo up to 50 sputter-annealing cycles. Sputtering is applied to clean the surface by Ar^+ ions (at 700 K, 1.5 keV, $5 \mu\text{A}$ ion current, 1 h, 45° incidence). Annealing for 5 min at 1300 K recovers the original stoichiometry at the surface and leads to smoothing. The cleanness is checked by Auger spectroscopy and the crystal structure by LEED. For a new preparation only one sputter-annealing cycle is applied. Subsequently the crystal is exposed to $4 \cdot 10^{-6}$ mbar oxygen at 540 K for 15 min. During oxidation only alumina is produced while the nickel diffuses into the bulk. Annealing at 1200 K for 2 min leads to an ordered film structure. Repeating of the last cycle closes the film and results in a well ordered and smooth structure which is checked by LEED and photoelectron spectroscopy.

The alumina film consists of an aluminum-oxygen double layer of 5 \AA thickness which is terminated by oxygen. Its structure differs

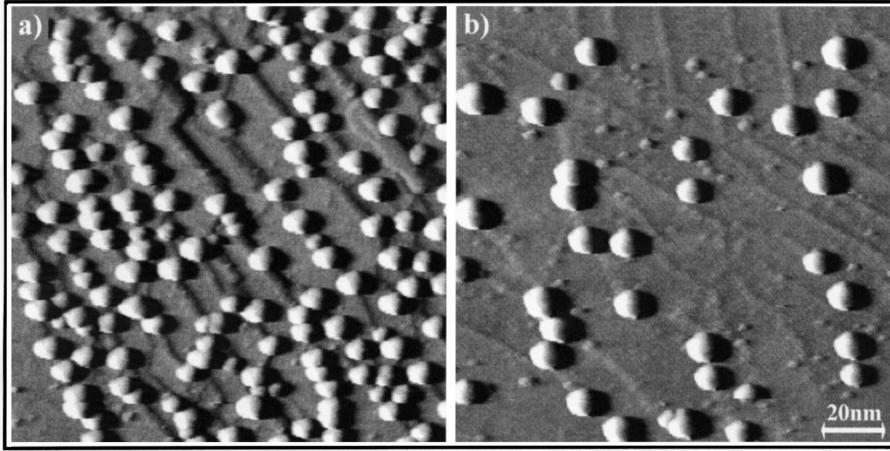


Figure 3.5: STM images of Ag nanoparticles grown on an alumina film, recorded by Niklas Nilius [32]. a) Cluster nucleation on step edges. b) Cluster nucleation on domain boundaries.

edges (see fig. 3.5). Clusters grow in 3-dimensional structures (Vollmer-Weber growth mode) due to the weak interaction with the support. As the density of nucleation sites is constant from 1 Å silver deposition on ($\approx 4 \cdot 10^{11} \text{cm}^{-2}$), the cluster size can be changed by varying the amount on deposited silver. The number of atoms per cluster should then linearly scale with the deposited silver amount until coalescence of adjacent clusters occurs.

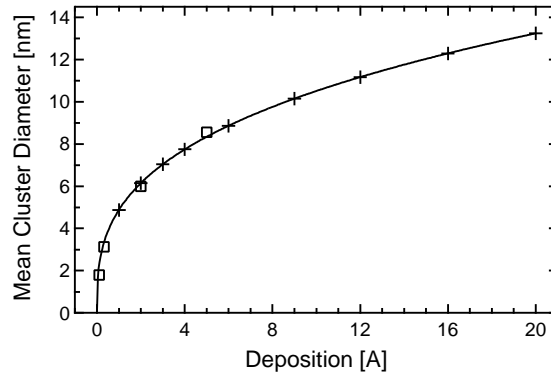


Figure 3.6: Cubic fit to STM data (squares). The crosses indicate depositions applied during experiments. For high deposition ($> 6 \text{ \AA}$) clusters flatten resulting in larger diameter than the fit indicates.

In fig. 3.6 a cubic fit (solid curve) to STM data (squares) gives an estimate of the expected mean cluster diameter. The crosses indicate depositions used during experiments. The mean aspect ratio for smaller clusters is around 0.5 (height to width) and decreases with larger cluster size as determined by STM [90]. At around 10 nm cluster diameter the begin of coalescence is expected.

3.3 Optical Setup

The optical setup is sketched in fig. 3.3. It consists of a commercial fs-laser system from Spectra Physics, an optical parametric amplifier from Light Conversion and a self-built noncollinear optical parametric amplifier. Pulses are compressed by prism pairs, frequency converted and characterized by wavelength, pulse duration, and spot shape.

The purpose is to probe the electron dynamics (typically in the fs regime) and electronic structure at the sample surface. The dynamics is dominated by the excitation of surface plasmons at energies around 3.6 eV, roughly fixing the necessary photon energy.

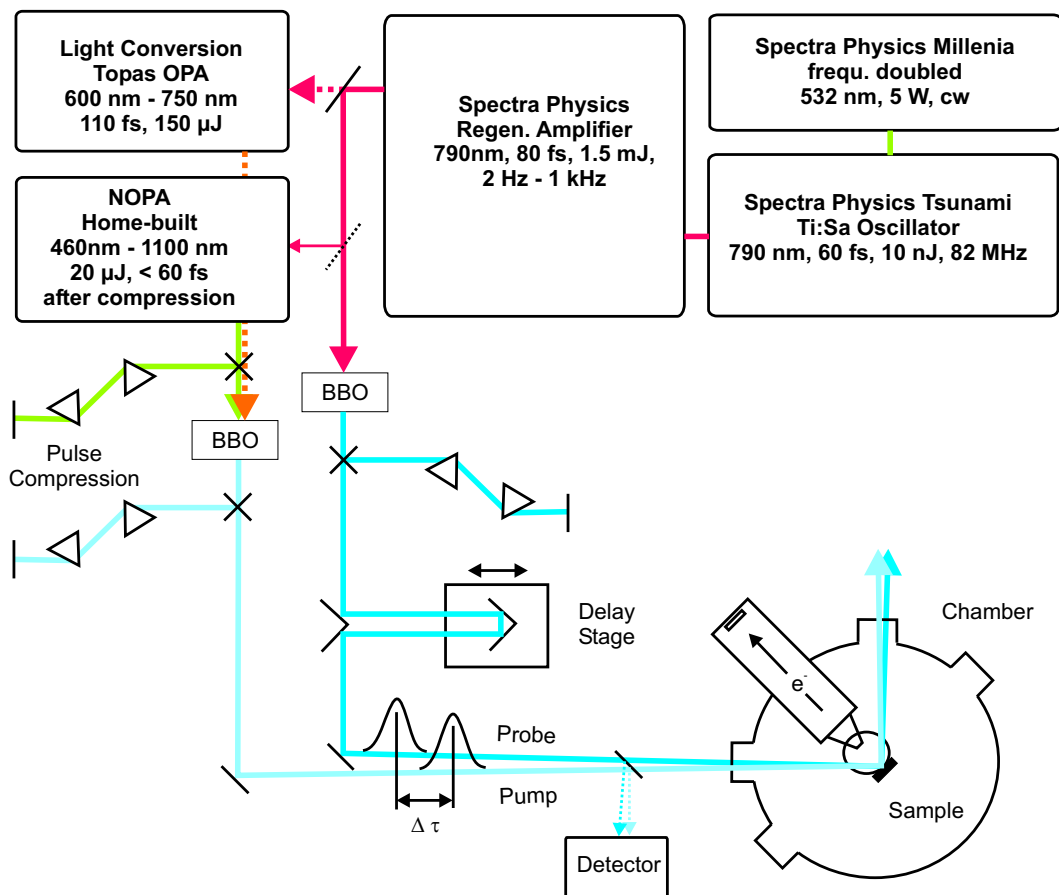


Figure 3.7: Sketch of the optical setup. A TiSa-oscillator is pumped by a diode laser to generate 60 fs pulses at 790 nm with a repetition rate of 20 MHz. Pulses are amplified by a Regenerative Amplifier which reduces the repetition to 1 kHz but increases the intensity per pulse to 1.5 mJ. This intensity enables the pumping of sequential devices like OPA or NOPA. For the NOPA a pump intensity of 300 μJ is sufficient providing two-colour measurements by splitting the beam and using the fundamental, second or third harmonic as additional colour.

3.3.1 Laser System

For the generation of femtosecond pulses a laser system from Spectra Physics was used consisting of an oscillator (Tsunami) and a regenerative amplifier (Spitfire), pumped by a continuous wave (cw) Nd:YVO₄ laser and two pulsed Nd:YLF lasers (Merlin), respectively.

The laser medium consists of Ti³⁺ doped Al₂O₃ which is characterized by a broad vibrational fluorescence reaching from 630 nm to 1130 nm [39]. This broad range allows on one hand for tuning the wavelength and on the other hand for generation of ultrashort pulses. The amplification is high compared to other laser media and exhibits its maximum at 790 nm ¹. Due to the absorption maximum at 490 nm and the long lifetime of the excited laser level of 3.2 μs the pumping with continuous wave lasers like Argon-ion laser or frequency doubled solid state lasers(Nd:YLF, Nd:YVO₄) is possible.

Laser Oscillator

To generate short pulses a high number of longitudinal modes of the resonator have to couple to a coherent superposition. This technique called "mode locking" is achieved either by active methods, e.g. acousto-optical modulators, or by passive methods, which provides shorter pulses down to 6.5 fs [120]. For Ti:Sapphire lasers generally passive "Kerr-lense" mode locking is employed. It is realized by introducing a medium with an intensity dependent diffraction index into the resonator, causing self-focussing. The Kerr-lense allows only light with sufficiently high intensity to remain inside the resonator. Since this effect weakens also with time, the pulse becomes shorter with every circulation up to equilibrium due to dispersion. The dispersion, due to different velocities of the various colours of the pulse, is mostly compensated by dielectric mirrors and a four prism arrangement inside the resonator. To start pulsing, an irregularity has to be introduced to the circulating light. This is here realized by an acousto-optical modulator which is stopped as soon as the laser operates.

The typical output at 790 nm wavelength are 60 fs pulses. The pulse intensity is 8.5 nJ at 82 MHz repetition.

Regenerative Amplifier

For frequency conversion with the optical parametric amplifier pulse intensities of around 1 mJ are necessary. The intensity enhancement of five orders of magnitude requires an arrangement differing from that previously described. It consists of two amplification stages with Ti:Sapphire as active medium, each pumped by a Nd:YLF-laser (Merlin). The pump pulses are frequency doubled resulting in 527 nm wavelength, 250 ns pulse duration, and 10 mJ intensity.

¹Other valuable properties of Ti:Sapphire are the high destruction threshold, good heat conductivity, and high density of energy storage [6].

A direct amplification of the pulses entering from the Tsunami would exceed the destruction threshold of the laser media. To reduce the intensity, pulses are stretched in time, amplified, and then finally compressed. This procedure is termed "chirped pulse amplification". As stretcher and compressor grating arrangements are used exploiting different path length for the different wavelengths. The first amplification stage consists of a resonator where pulses are coupled in by a Pockels cell to circulate until their amplification saturates due to the decrease of the population inversion at the Ti:Sapphire crystal. Subsequently the amplified pulse is coupled out by a second Pockels cell to traverse a Multipass amplifier where the pulse passes three times through another Ti:Sapphire crystal.

The amplification of each pulse is fairly time consuming and the amplifier has to "regenerate" its population inversion. For that reason the original repetition cannot be kept. In this case it is determined by the repetition of the pump laser of 1 kHz. Resulting pulses are <100 fs with up to 1.5 mJ intensity.

3.3.2 Optical Parametric Amplifier

The Ti:Sapphire amplifier output is restricted to a spectral range of 750 nm - 840 nm. In order to detect a change in photoemission depending on the wavelength generally a much wider tuning range is necessary, provided by an optical parametric amplifier (OPA). Its concept is based on the ability of splitting one photon (k_0) into two, where momentum must be conserved:

$$k_0 = k_{signal} + k_{idler}, \quad (3.11)$$

where k_{signal} stands for the desired wave vector and k_{idler} represents the residual part. This process is feasible e.g. in a birefringent crystal. To achieve a certain wavelength a seed pulse is required which provides the appropriate wavelength. It enters the crystal collinearly to the pump pulse. If the phase matching condition is fulfilled, i.e. by adjusting the proper angle of the crystal (group velocity of both pulses must be equal), the seed pulse is amplified by several orders of magnitude.

The seed pulse is generated by focusing a small fraction of the initial intensity into a crystal to induce strong nonlinear effects which finally lead to the creation of white light.

As OPA the TOPAS from Light-Conversion is used which consists of two amplification stages and provides up to 200 μ J pulses at 1.2 mJ input with a spectral range of 580-760 nm. Pulse length without compression is < 110 fs.

3.3.3 Noncollinear Optical Parametric Amplifier

The noncollinear optical parametric amplifier (NOPA) is very similar to the previously described OPA (see sec. 3.3.2), but offers some essential advantages [130], which is the reason why it has been built up during this thesis. The basic difference to OPA is

that, as the name tells, seed and pump beam do not enter collinearly the optical active crystal but under a certain angle, as depicted in fig. 3.8. Equation 3.11 therefore has to be changed into vectorial notation:

$$\vec{k}_0 = \vec{k}_{signal} + \vec{k}_{idler} \quad (3.12)$$

This correlation enables the phase matching condition for a much wider spectral range at once such that amplified pulses can be compressed to much shorter duration (< 60 fs after compression). Furthermore, by changing the angle a broader spectrum is available (1100-460 nm), which also allows one-photon photoemission (1PPE) spectroscopy at up to 5.3 eV after SHG. The conversion efficiency with more than 0.3 is a factor of three better than for OPA. Therefore comparatively smaller pump intensities are required and the excess intensity may be used as additional colour for two-colour experiments.

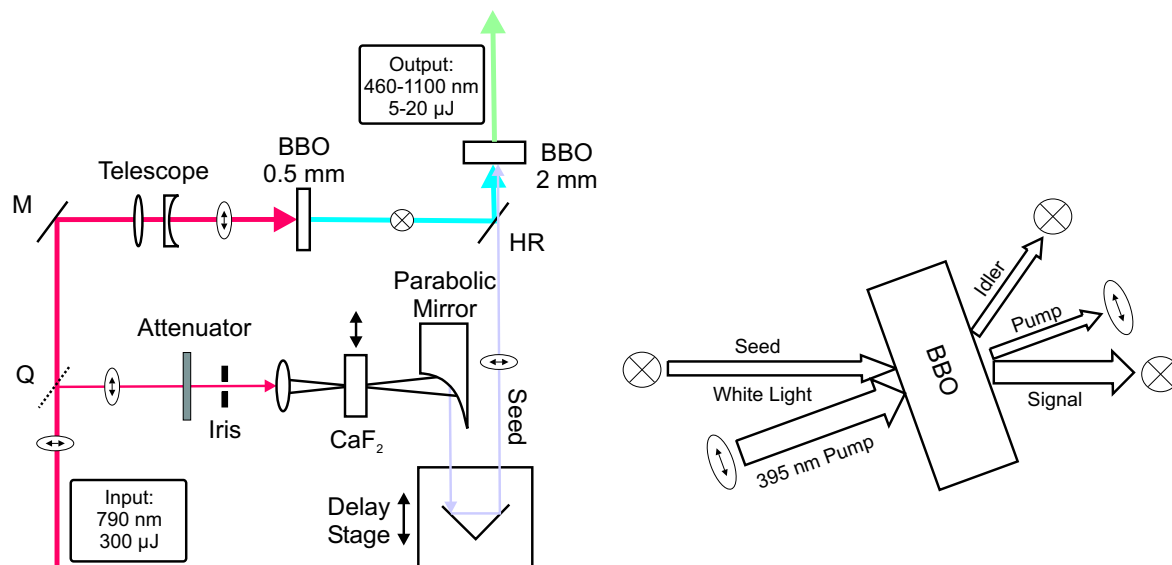


Figure 3.8: Sketch of NOPA

A small fraction of the Spitfire output is necessary to pump the NOPA. The input beam is polarized parallel to the optical table plane as indicated by the arrows in fig. 3.8. By passing a Quartz plate Q, 4 % of the intensity are split off to generate white light. The main intensity passes the mirror M and the telescope to narrow the beam diameter for a better efficiency in second harmonic generation by a 0.5 mm thick BBO crystal. The second harmonic then is focused by a spherical mirror HR(395 nm) into a 2 mm thick BBO as pump light to produce parametric fluorescence.

The lower intensity part split off at the beginning can be varied by a variable attenuator and an iris before it is focused by a Quartz lens into a CaF₂ crystal. The established electric field intensities cause higher order processes resulting in the generation of white light. Compared to conventionally used Sapphire crystals CaF₂ provides

several advantages: Higher intensity of the white light, broader spectral range, and lower chirp [51]. This light serves as seed pulse and is focused by an off-axis parabolic mirror into the 2 mm BBO to overlap with the pump pulse. For optimization of the temporal overlap the seed pulse passes a delay stage. Since the white light holds a chirp due to dispersion, the delay stage allows tuning by overlapping the desired colour of the seed pulse with the pump pulse.

However, there is one hitch concerning the CaF₂ crystal: Upon irradiation the white light generation weakens with time. To overcome this effect the crystal has to be moved constantly perpendicular to the beam axis. For this purpose an appropriate device was built consisting of two micro stages movable in the x/y-plane and driven by an electric motor. Deviations in z-direction during rotation were determined to be smaller than 10 μm .

For oncoming photodesorption experiments the NOPA may be extended by a second amplification stage to enhance the pulse intensity [108].

3.3.4 Beam Pathway

The 790 nm pulses of the Spitfire may be directly frequency doubled by a 0.5 mm thick BBO-crystal. The fundamental then is split off by passing a dielectric mirror, while the second harmonic at around 3.16 eV photon energy and 100 fs pulse width is led to the sample. For photon energy dependent measurements, i.e. scanning the plasmon resonance or determination of unoccupied states, the Spitfire output is used to pump the OPA which provides an easy tuning of the wavelength if once adjusted. For time resolved measurements the NOPA is used. A fraction of the Spitfire output then is used as pump by passing a beam splitter. The visible NOPA output is compressed by a prism pair (60° SF10) by exploiting negative group velocity dispersion. In this arrangement the path length for red light is longer than for blue light, compensating the positive dispersion due to optical components. After SHG the resulting UV pulses are again compressed by prisms (60° Quarz). To guide the beam generally Ag coated mirrors are used for visible light and Al coated mirrors in the UV. To change the beam polarization $\frac{\lambda}{2}$ -plates are used.

For the use of two colours additionally the remaining part of the 790 nm light was frequency doubled, compressed and overlapped with the other colour on the sample at an angle $< 2^\circ$. For adjustment of the spatial overlap a flip-mirror in front of the chamber reflects both beams onto a screen at the same distance as the sample. For a defined overlap in time the second colour passes a motor driven delay stage, i.e. a retroreflector mounted on a microstage.

To minimize vibrational influences the beam path length was kept as small as possible. Also the number of mirrors was reduced to avoid absorption losses.

3.3.5 Pulse Characterization

For characterization of ultrashort pulses ≤ 100 fs special techniques are required. As electronic mechanical methods, e.g. streak cameras, are restricted to a maximal temporal resolution of ≈ 200 fs, they cannot be employed for this purpose. Rather, optical correlation methods are used to determine the pulse duration.

The Spitfire pulses are determined by a commercial autocorrelator, which is useful for high intensity pulses around 800 nm. A pulse is split in two parts which travel each along a delay path to be overlapped in space and time in a nonlinear crystal under a certain angle. The spatial width of the resulting sum frequency signal depends also on the pulse duration of the fundamental and is read out by a CCD array. For determination of the pulse duration in the visible region a self-built device is used. The beam is here also split in two which are then focused by spherical mirrors to overlap in a 0.3 mm thick BBO(GWU) crystal. Before, one of the beams passes a delay stage. The finally generated sum frequency signal is detected by a photodiode while the delay stage is moved. The resulting autocorrelation signal for 2.7 eV photon

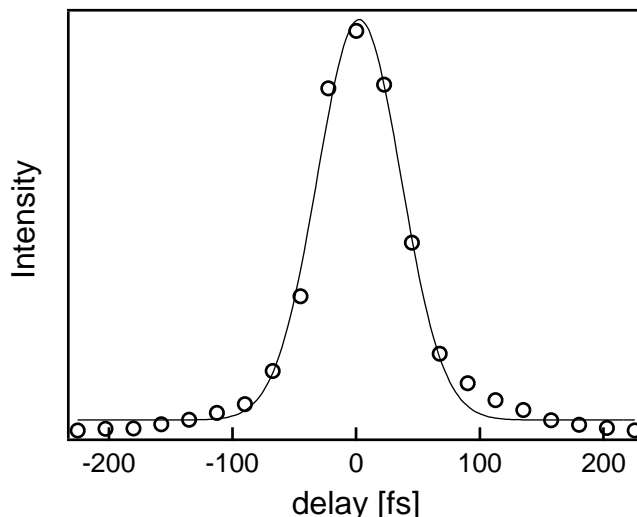


Figure 3.9: Autocorrelation trace of $h\nu=2.7$ eV pulses. The data are represented by open circles, the solid curve represents a gaussian fit to the data. Its width of 80 fs corresponds to a pulse width of 56 fs.

energy is represented in fig. 3.9 by open circles. The solid curve is a gaussian fit to the data. By assuming gaussian shape of the pulses we can extract the pulse width by multiplication of the autocorrelation width with $1/\sqrt{2}$, resulting here in 56 fs.

The BBO is suitable, i.e. transparent, for wavelengths >205 nm. Therefore, SHG is only likely at wavelengths >410 nm. However, we may use the sample instead of the BBO and take the resulting nonlinear photoemission signal instead of the SHG-signal for photon energies lower than the work function. Since we probe in this case

the unoccupied electronic structure of the sample, the correlation width gives only an upper limit of the pulse width. By taking only the high energy photoelectrons, corresponding to intermediate state energies $E-E_F > 1.5$ eV, lifetime effects should be negligible compared to the pulse width. Moreover, the determination of the pulse width on the sample includes already all effects of pulse broadening due to dispersion, e.g. by the windows. The pulse compression is then iteratively optimized.

The spectral shape can be determined by a grating spectrometer. The spatial width is checked by introducing a 0.1 mm slit into the beam. The detection of the transmitted intensity then reveals roughly the spot shape by moving the slit perpendicular to the beam axis.

3.4 Data Acquisition and Controlling

Data is acquired and experiments controlled by a realtime computer (Wind River Systems) as illustrated in fig. 3.10. It is connected via a VME-bus to a work station (SUN) which provides the user interface written in JAVA.

For acquisition of a Photoemission spectrum the flight time of an electron is determined and fit into a 1024-channel register. Each channel corresponds to a time window of 2 ns restricting the detection range to $2.048 \mu\text{s}$. This is realized by a self-built multi-hit time-to-digital converter which is able to detect 5 stop pulses per start pulse. The start pulse passes an amplifier and a leading edge discriminator. A stop pulse is preamplified directly after leaving the UHV and led to a constant fraction discriminator. The discriminators convert pulses into standard shape and amplitude (Fast NIM). For determination of the pulse rate of start or stop pulses rate-meters are used.

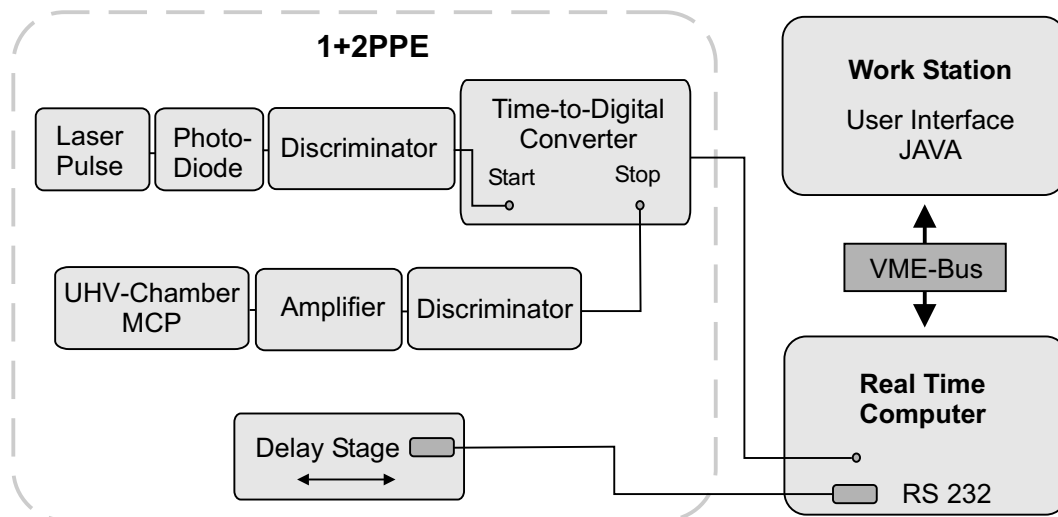


Figure 3.10: Instruments applied for data acquisition and controlling.

For time-resolved experiments time-of-flight spectra are recorded for different pump-probe delays. The delay is changed by varying the path length of one of the two beams (Accuracy $\approx 0.1 \mu\text{m}$ (2/3 fs)). The delay position, controlled by the computer via RS232 interface, is associated to each event during time-of-flight acquisition. A typical accumulation time for corresponding time-of-flight spectra is 2 s per delay step. To compensate intensity fluctuations of laser pulses, the procedure is repeated around 20 times.

3.5 Table of Instruments

In the following the basic instruments are listed which are mentioned in the text. Self-built devices are not noted.

UHV System

- Chamber, Vacuum Generators
- Manipulator, PINK
- Turbo Pump, Varian, Turbo-V550
- Rotational Pump, Pfeiffer-Vakuum
- Ion Getter Pump / Titanium Sublimation Pump, Varian, Vacion Plus 300
- Ion gauge, AML, PGC2
- Pirani gauge, Pfeiffer-Vakuum, CMR 263
- Auger / LEED, Specs, ErLEED Digital
- Quadrupole Mass Spectrometer, Pfeiffer-Vakuum, Prisma QMS 200 M2
- Evaporator, Omicron, EFM3
- Micro Balance, Caburn, MDC
- Cs Dispenser, SAES
- Ion Gun, Specs, IQ11-35

Optical Components

- Diode Laser, Spectra Physics, Millennia
- Ti:Sa-Oscillator, Spectra Physics, Tsunami
- Regenerative Amplifier, Spectra Physics, Spitfire
- Optical Parametric Amplifier, Light Conversion, TOPAS
- Delay Stage, Physical Instruments, M-515.22
- Autocorrelator, Positive Light, SSA
- Grating Spectrometer, Ocean Optics, USB 2000

Data Acquisition

- Photodiode, Hamamatsu, R840
- Preamplifier, EG&G Ortec, VT120
- Amplifier / CF-Discriminator, Tennelec, TC 454
- 100 MHz Discriminator, Ortec, 436
- Lin/Log Ratemeter, Tennelec, TC 527

Chapter 4

One-Photon Photoemission

In this work, one-photon photoemission (1PPE) was realized by employing the high energy output of the noncollinear optical parametric amplifier. After second harmonic generation a photon energy of 5.3 eV was achieved which is higher than the work function of Ag(111) determined to 4.55 eV¹. This applies also for silver nanoparticles of up to ≈ 15 nm corresponding to a work function of 4.4 eV, which decreases for smaller particles.

4.1 Introduction

If a metal is illuminated by photons with energy higher than its work function, i.e. vacuum level E_{Vac} , photoemission occurs. The photon energy $h\nu$ is transferred to an electron resulting in a kinetic energy $E_{Kin} = h\nu - E_{Vac}$ after emission. The determination of the kinetic energy of the emitted electrons and integration over an appropriate time interval yields information about the density of states of the metal.

However, an electron may experience an influence from its excitation until it reaches the detector. If we consider an electron excited in the bulk, its excitation probability λ_{if} depends on the density of states in the final state $\rho_f(E)$, given by Fermi's golden rule:

$$\lambda_{if} = \frac{2\pi}{\hbar} |M_{if}|^2 \rho_f(E), \quad (4.1)$$

where M_{if} is the transition matrix element, described by

$$M_{if} = \langle \Psi_f | A \cdot \nabla + (\nabla \cdot A)/2 | \Psi_i \rangle, \quad (4.2)$$

with A denoting the vector potential of the incident light.

While the electron approaches the surface, it may suffer inelastic scattering with other electrons and phonons or elastic scattering with the lattice. Inelastic scattering

¹Alternatively, for 1PPE the fourth harmonic of the Ti:Sapphire output can be used at >820 nm. However, at these wavelengths the present oscillator is not stable.

processes will result in a background signal in photoemission. If the electron reaches the surface, it may be reflected according to its energy dependent escape function [16, 15]. As soon as it escapes into the vacuum it leaves a positive hole behind. The interaction between hole and electron depends on the lifetime of the hole having an influence on the electron kinetic energy [121, 50]. For isolated nanoparticles this lifetime is infinitely long having a strong influence on the electron energy, while for a bulk the lifetime may be only a few femtoseconds. The lifetimes of hole and emitted electron influence also the width of the detection state.

4.2 Evolution of Density of States with Nanoparticle Size

For investigation of the occupied density of states, the bare alumina film was probed normal to the surface. Subsequently the change of emission spectra was analyzed in dependence on a progressive deposition of silver. As silver aggregates in 3-dimensional structures, the alumina support will not be perfectly covered. Therefore, a contribution of the support to particle spectra cannot be eliminated. To determine the actual contribution of particles, a two step evaluation has to be performed, which will be described in detail below.

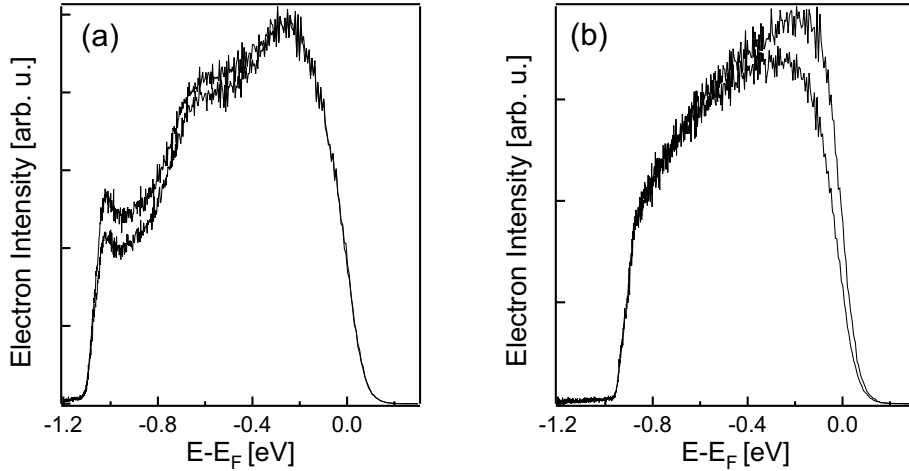


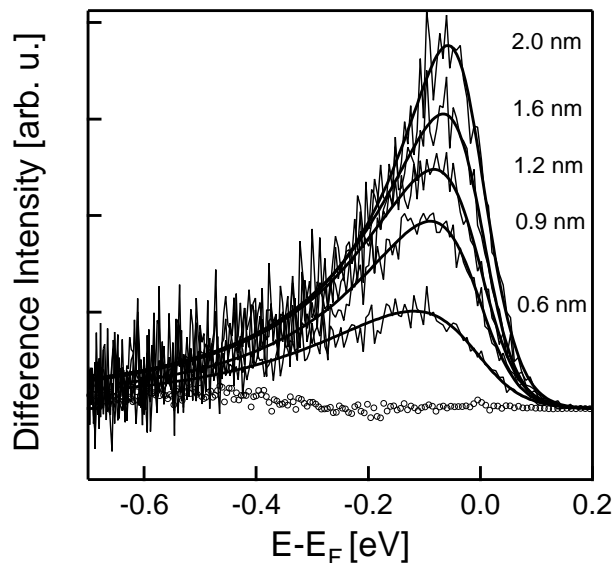
Figure 4.1: (a) s/p-polarized spectra of the bare alumina film. The s-polarized spectrum is slightly lower in intensity. The structure is due to the NiAl support underneath. (b) s/p-polarized spectra of the alumina film after 20 Å Ag deposition. The work function changes and support features disappear. The s-polarized spectrum is matched to the p-polarized spectrum at low energies with 2 times higher intensity than for (a).

Fig. 4.1(a) displays spectra of the bare alumina film. The electron kinetic energy is related to the Fermi level as obtained from the spectrometer calibration (sec. 3.1.2). The higher intensity belongs to p-polarized, the lower to s-polarized light. As the

alumina film exhibits a pronounced band gap from -3 eV to 5 eV, it should not show distinct features like those at -0.2 and -0.6 eV. These features can be attributed to the NiAl-support underneath. However, photoelectrons of these energies are not allowed to pass the band gap. This contradiction as well as the similar intensities for s and p-polarization can be explained by photoelectrons being scattered at step edges or alumina domain boundaries where the oxide film is not closed. Direct photoemission processes, e.g. tunneling through the alumina film, have in this case a minor contribution.

By silver deposition the distinct features disappear very fast and intensity increases - for s-polarized light only slightly and for p-polarized light up to a factor of 2 for the highest used deposition of 20 Å silver. Such a strong quenching of support features is expected as the nanoparticle nucleation preferentially takes place at step edges or alumina boundaries, i.e. the sources of scattered support electrons. Spectra for 20 Å silver deposition are shown in fig. 4.1(b). The vacuum cutoff at low energy changes by 0.14 eV compared to fig. 4.1(a) due to an increase of the work function. The p-polarized spectrum with higher intensity exhibits a much steeper Fermi edge than the bare oxide surface. If we match the s-polarized spectrum to it at low energies we can recognize a difference between the spectra near the Fermi edge. This difference changes with the amount of silver deposition.

Figure 4.2: 1PPE spectra for mean deposition thicknesses as indicated at the right. Curves were obtained by matching the s-polarized to the p-polarized spectrum at low energy. The difference between them is shown. They fit well to a Lorentzian which is cut off at the Fermi level (thick lines). The open circles represent the result for the bare alumina film.



As we are not able to determine the contribution of the support to the spectra we make in the following use of a photoemission selection rule: Direct photoemission normal to the surface is only likely if an electric field component points to that direction. Therefore, in our case, a direct emission is only likely for p-polarized light, while for s-polarization only scattered electrons can be detected. If we match both spectra to each other, appearing differences can be attributed to direct transitions. However, electrons

excited by s-polarized light may elastically scatter at defects or particle boundaries to normal direction. This contribution is of minor intensity but may influence the position of the resulting feature. Therefore, we have to assume that for each polarization the same state is probed, as it would be the case for a surface state on particles with a smooth surface on top.

The matching was carried out for various silver depositions. The resulting difference between the spectra is plotted in fig. 4.2. Data could be extracted down to 6 Å deposition only, though a feature can be seen down to 2 Å deposition. However, it eludes the evaluation by matching because the support structure then dominates the signal. Open circles represent the result for the bare surface.

The peak fits well to a Lorentzian that is cutoff by a Fermi distribution at the Fermi edge. The fitting provides information about its position and width, shown in fig. 4.3, as well as a more accurate positioning of the Fermi level than can be achieved by the wavemeter at these high photon energies. The width seems to be correlated with the position of the peak and the particle thickness. Very similar results were observed for quantum well states in silver films of equal thicknesses [82]. In this case the width was assigned to lifetime broadening due to the imperfect reflectivity of the boundaries, scaling with the inverse of the thickness. However, quantum well states should show up as a series and not as a single state. Alternatively, a broadening by lifetime of this magnitude was also found for a surface resonance on vicinal surfaces [87]. In that case the band gap of Ag(111) in $\Gamma - L$ direction was closed leading to strong coupling of the surface state wave function with bulk states and a corresponding short lifetime.

The surface state position on Ag(111) at -63 meV, 30 K [107] is near to the observed energies. It is reasonable to expect it also on the particles, especially since a hexagonal shape of individual silver nanoparticles for the same system was found by STM [93]. However, with increasing particle size the state should converge into the bulk-like one. This seems not to be the case, moreover, it moves to much higher energy and its dependence on thickness goes all the way linearly without showing any saturation. Nevertheless there are some effects that may influence the position of a surface state. These will be discussed below.

- A shift to higher energy due to lateral confinement is very well known for nanoparticle islands. Surface state electrons can be treated as being confined in a potential well. The surface state parabola then is split into discrete energy levels, and the bottom is shifted up (see [71], [87]). However, for large nanoparticles of 20 Å deposition the mean diameter is > 15 nm. The resulting shift in energy would be < 10 meV and lacks to explain the observed value of ~ 80 meV.
- A shift to lower energy due to the cutoff of the surface state wave function at the support was reported by Patthey [98]. This effect only becomes pronounced if the decay length for the surface state is in the same range as the layer thickness. For silver films on graphite a decay length of 2.6 monolayers was found, leaving this influence negligible.

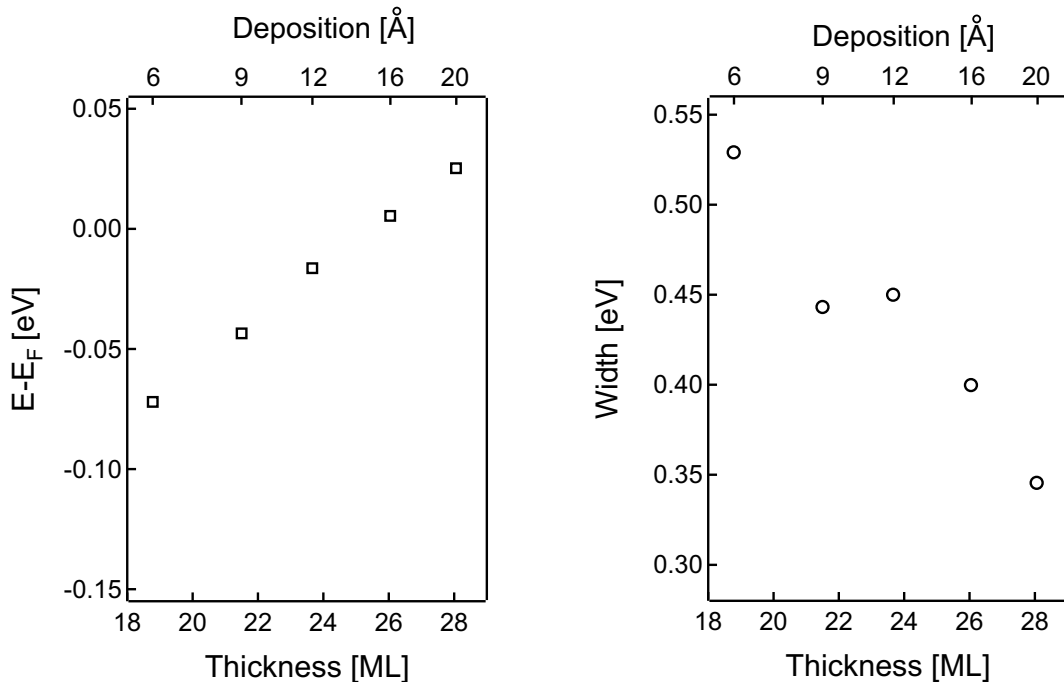


Figure 4.3: Result of the fitting in fig. 4.2. The position of the peak shifts to higher energy with increasing nanoparticle size while the width diminishes. For comparison with literature the expected mean particle thickness is given.

- A shift may also be induced by a mismatch of the lattice constants of nanoparticle and support. This mismatch can induce strain to the nanoparticle changing its interatomic distance. The result is a shift of the sp-band edge to which the surface state is related. This relation can be understood by the phase accumulation model (PAM) described in sec. 2.1. For silver films on Si(111) a shift of the surface state by 150 meV to higher energy was found by Neuhold [89]. Such a scenario would give an explanation for the data and will be discussed at the end of this chapter.

A common way for the identification of a surface state is to check its energy dispersion parallel to the surface [8]. On a silver(111) crystal this dispersion is described by a free electron parabola and has been recorded with the present setup. In the case of nanoparticles the electrons are laterally confined causing the parabola to split into discrete energy levels. Furthermore, in the present case only a small photon energy is available. That requires an appropriate tilt of the crystal in order to reach the sequential quantization level of the surface state [87] which leads in our case to inhomogeneity of the electric field near the sample. Finally, a lateral dispersion of the discussed peak could not be observed.

Another proof can be performed by covering the surface with adsorbates. As a surface state is related to the properties of the surface, it should be influenced by

adsorbates or even quenched as its wave function extends into the vacuum [17]. The influence by adsorbates will be studied in the next section.

4.3 Influence on Density of States by Cs Deposition

The aim of this section is to examine a possible influence on the density of states by covering the nanoparticle surface with adsorbates. On one hand we would expect an interaction of certain adsorbates with the wave function of the surface state extending into the vacuum. This may lead to a "poisoning" of the state and associated vanishing. On the other hand adsorbates can induce a change of the work function. Such a change is expected to influence the surface state position (see sec. 2.1). In the following cesium was chosen [89] which induces a pronounced dipole if adsorbed on the surface. The result is a lowering of the work function which also opens up a wider spectral range for 1PPE. To obtain a homogeneous distribution atomic adsorption is desired. For that reason the sample is usually liquid nitrogen cooled to enhance the sticking coefficient. The additional adsorption of Cs on not Ag covered alumina parts should lead to a background in the Ag particle photoemission spectra. Consequently, in two-photon photoemission a second vacuum cutoff at lower energies has been found, indicating the emergence of Cs clusters. In the present case of very large Ag nanoparticles, the existing background did not change upon Cs deposition remaining at 2 % signal intensity.

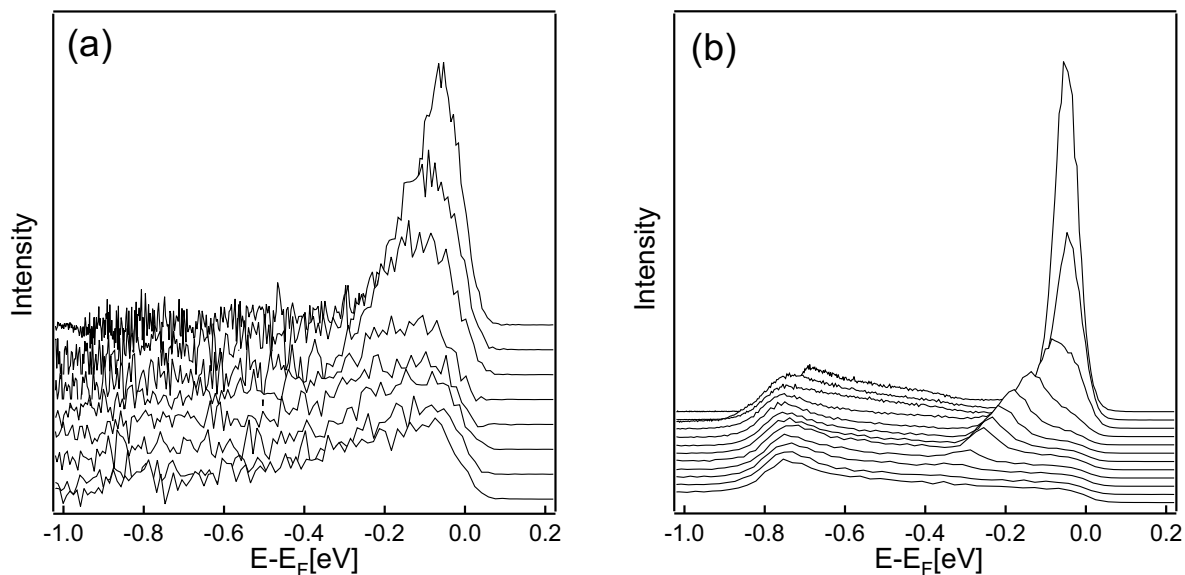


Figure 4.4: Samples are liquid nitrogen cooled leading to 83 K. (a) Difference spectra for 20 Å silver deposition are shown prepared in the previously described manner (sec. 4.2). The curve on the top represents data for pure silver nanoparticles, covered progressively with cesium. (b) Spectrum of a silver(111) crystal undergoing the same procedure as in (a). Basically the same trend can be seen but the shift of the surface state is much more pronounced and ends in a complete quenching.

Fig. 4.4 shows spectra of liquid nitrogen cooled samples. The single spectra were progressively collected, each after the sample was additionally covered with cesium.

At the top of fig. 4.4(a) the debated peak for 20 Å silver deposition is displayed. It is strongly quenched by Cs deposition in the beginning but then levels off for higher deposition without being totally quenched. A slight shift to higher binding energy can be seen while the work function decreases (not visible here). The width becomes broader with increasing Cs coverage.

In (b) for the surface state on Ag(111) at -50 meV basically the same trend as in (a) can be seen but the shift of the state is much more pronounced. Interestingly, after the first Cs exposure the surface state moves at first slightly to higher energies. Such a behaviour can be understood by considering the Cs atoms dividing the initial surface into smaller parts. Surface state electrons then are reflected by the Cs atoms building up potential wells of various sizes. This leads as previously described (sec. 4.2) to a rise in energy. At the same time the surface becomes inhomogeneous resulting in a broader peak.

The quenching of the particle peak by adsorbates indicates its relation to surface properties. Furthermore, the influence of a change in work function reveals that the origin of the peak should be either a surface state or a quantum well state, as only these exhibit an explicit dependence on the work function. Its large width and the lack of complete quenching by cesium speaks for the latter. However, still a surface resonance has to be taken into account, with their wave function penetrating far into the bulk eluding a complete "poisoning".

Fig. 4.5 shows again data for 20 Å silver coverage but with cesium deposition at room temperature. In contrast to the previous data a quenching and broadening of the peak only takes place very late. Nevertheless the work function changes and so does slightly the position of the peak.

The cesium atoms can be considered much more mobile on a silver surface at room temperature than at liquid nitrogen temperature. Consequently, one can think of most atoms diffusing off the particle top surface, especially if it is (111)-terminated. They may then preferentially stick at the edges of the nanoparticle, still inducing a work function change but no other effects as those mentioned above. These data can be explained by applying the phase accumulation model in fig. 4.6.

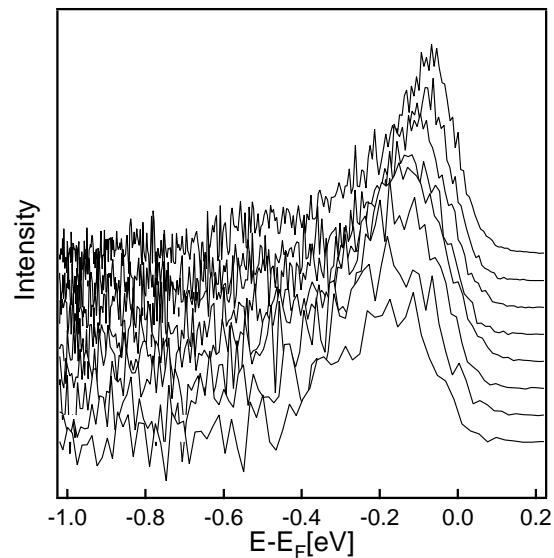


Figure 4.5: Sample at room temperature. The on top curve represents a difference spectrum for 20 Å silver deposition, progressively deposited with cesium for lower curves. Data were prepared as described in sec. 4.2.

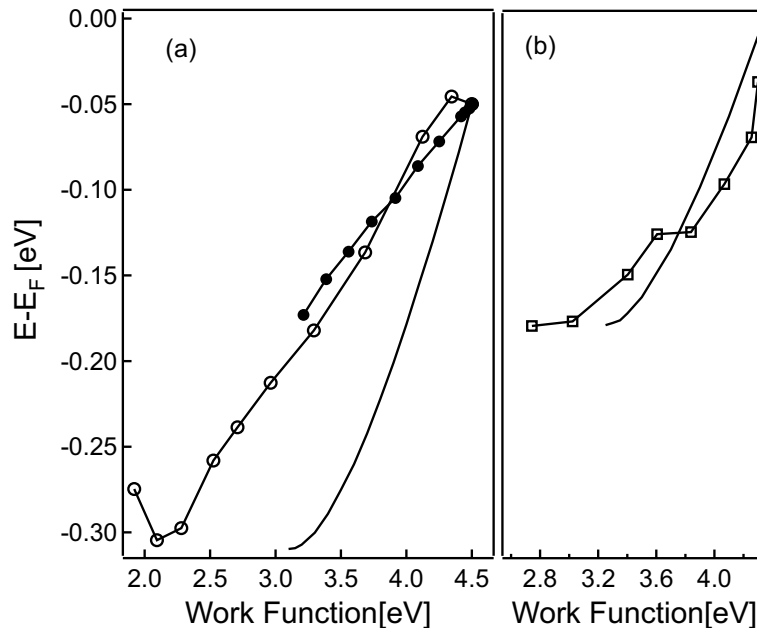


Figure 4.6: (a) The shift of the surface state on Ag(111) with the work function is shown. Open circles represent liquid nitrogen data, closed circles room temperature data. The line is given by the phase accumulation model for Ag(111). (b) Data from fig. 4.5 are shown which level off already at -0.18 eV. By assuming a surface state this could be explained by a shift of the band edge up to this value in accordance to the phase accumulation model (solid line).

The phase accumulation model predicts a shift of the surface state in dependence on the work function (see sec. 2.1). The surface state only exists inside the band gap and levels off by approaching the band edge at -0.31 eV (solid line in fig. 4.6(a)). The experimental data show the same trend but the slope is different. This discrepancy is in fact not surprising as the measured work function, determined by the vacuum cutoff, gives always a mean value. If we take the formation of small cesium nanoparticles on the surface into account, the local work function at the Ag(111) facets should be higher than the mean value.

This can also explain the different slopes for room temperature and liquid nitrogen data. As the cesium atoms are more mobile at higher temperature they tend to form fewer and bigger nanoparticles. As a result the inhomogeneity is enhanced leading to a smaller slope in fig. 4.6(a). A shift due to confinement as for the cooled sample is not visible any more.

In fig. 4.6(b) nanoparticle data of fig. 4.5 are shown. They level off already at -0.18 eV which may be due to a shift of the band edge according to the phase accumulation model if a surface state is assumed. A shift of the band edge can be caused by a mismatch of the lattice constants of nanoparticle and support, inducing a contraction of the lattice as discussed before. However, this seems to be not very likely as the interaction between the alumina film and silver should be weak. Therefore, support

induced strain should play a minor role.

It should be mentioned that by scanning tunneling spectroscopy no surface state was found although individual nanoparticles showed hexagonal structure. Moreover, a series of quantum well states has been observed [93], which we already discussed as an alternative solution. This could also explain the difficulties in interpretation for the current peak. However, quantum well states should show up as a series, but down to -2.5 eV below Fermi level no other feature was found. This apparent contradiction will be discussed in detail in section 5.2.

Chapter 5

Two-Photon Photoemission

With respect to photochemistry electronic excitation and relaxation processes play an essential role. On a surface these processes are determined by the involved density of states of the substrate. Subsequent electronic transitions to the lowest unoccupied molecular orbital (LUMO) of the adsorbate can induce its desorption [106, 77, 3]. Therefore, for a detailed study of photodesorption processes, the knowledge of states involved in the excitation process is an important issue.

Two-Photon Photoemission (2PPE) spectroscopy is a powerful tool for probing unoccupied states below the vacuum energy. The photon energy is chosen such that a single photon excitation is not sufficient for an electron to overcome the work function. It is rather used as pump to populate an intermediate state. Subsequently this pumped electron is probed by a second photon to escape into the vacuum (see fig. 5.1(b)).

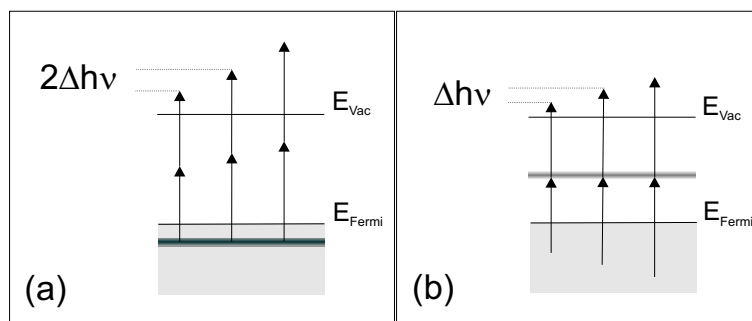


Figure 5.1: Diagram of 2PPE Processes. (a) The probing of occupied states requires two photons. A change in photon energy therefore leads to a change in kinetic energy of the resulting photoelectrons of $2\Delta h\nu$. (b) The probing of intermediate states requires only one photon, resulting in a corresponding change in kinetic energy of $\Delta h\nu$.

Fig. 5.1 depicts two possible excitation mechanisms in 2PPE. In fig. 5.1(a) the excitation via a virtual state is illustrated, in fig. 5.1(b) an intermediate state transition. The virtual state transition occurs if no real intermediate state is available for a specific excitation path. Therefore, a 2PPE spectrum may generally consist of both processes.

That does not allow to distinguish between occupied and unoccupied state at first glance. However, if the photon energy is changed by $\Delta h\nu$, the resulting change in kinetic energy of photoemitted electrons for either state is different, as illustrated in fig. 5.1. An intermediate state is probed by only one photon, while an occupied state is probed by two photons. Thus the shift in kinetic energy will be once or twice $\Delta h\nu$, respectively. The Fermi level behaves like an occupied state. Therefore, relative to the Fermi level, occupied states will not shift by a change in photon energy, while unoccupied states will shift with $-\Delta h\nu$.

Another issue of 2PPE on silver nanoparticles is the excitation of the surface plasmon at around 3.6 eV. Its interaction mechanism with the density of states is not yet clear but its excitation leads to a strong enhancement of the photoemission yield [69].

In 2PPE the same effects may occur as already discussed for 1PPE in sec. 4. Additionally, there is the influence of the intermediate state in a coherent two-photon excitation. The lifetime of this state can be described by the Fermi liquid theory and is $\propto (E - E_F)^{-2}$ [94]. The coherent transition probability therefore depends on photon energy as soon as the laser pulse width exceeds the intermediate state lifetime.

5.1 Photoemission Depending on Nanoparticle Size

The effect of silver deposition on alumina was studied. From STM measurements it is known that silver, if deposited on the alumina film at room temperature, aggregates on defect sites and alumina domain boundaries (sec. 3.2.2). The density of nucleation sites should stay constant independent of the deposited silver amount and alumina film preparation. Therefore, the number of atoms per nanoparticle should be proportional to the amount of deposited silver.

At the bottom of fig. 5.2 the photoemission spectrum of the bare alumina film is shown at 3.16 eV photon energy. The sample is then covered by an increasing amount of silver. The total amount is indicated at the left in terms of silver film thickness. For comparison at the top a spectrum of Ag(111) is shown multiplied by a factor of 40. The spectral range is limited at low kinetic energy by the vacuum cutoff and at high kinetic energy by the Fermi level.

The 2PPE spectrum of Ag(111) shows the Shockley surface state near the Fermi edge at 2.2 eV, and the sp-intra band transition peak at 1 eV. The 2PPE spectrum of silver nanoparticles is dominated by the hot electron distribution at low energy. The intensity increases with silver deposition and levels off at about 0.9 nm. The total photoelectron yield is then about 100 times larger than that from the bulk Ag(111). The feature near the Fermi edge is broader than in case of 1PPE but also approaches the Fermi edge with increasing deposition. It becomes more pronounced until 0.4 nm deposition with a subsequent closing on of the hot electron signal. Interestingly, for the

¹This is especially applicable in case of silver [11]

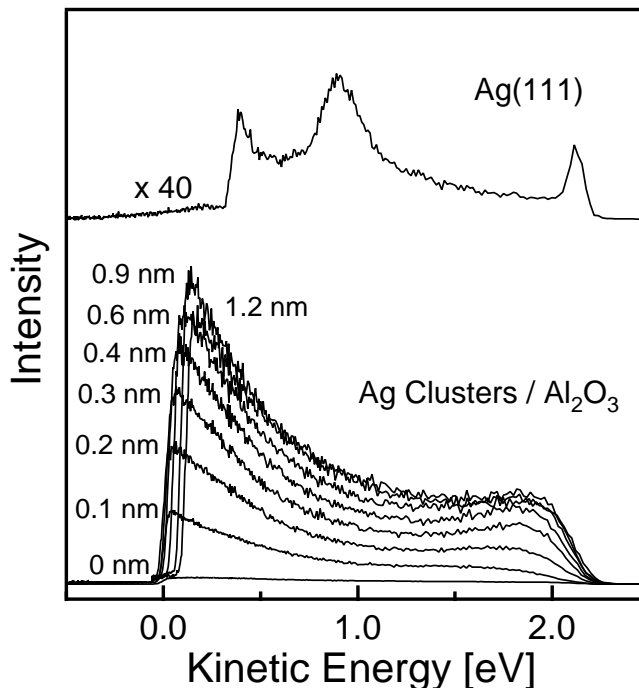


Figure 5.2: 2PPE spectra of Ag nanoparticles on alumina at $h\nu=3.16$ eV. The corresponding silver deposition thickness is shown in nm units. For comparison the 2PPE spectrum of silver(111) is shown on top, multiplied by a factor of 40.

nanoparticles the sp-intra band transition peak is absent, which could be an indication for a changed electronic structure compared to Ag(111).

Fig. 5.3(a) shows the intensity dependence on silver deposition of the feature near the Fermi edge. The signal from 1.5 to 2.3 eV kinetic energy in fig. 5.2 is integrated for 3.16 eV photon energy represented by closed circles. The same has been done at 3.6 eV photon energy for an adequate interval shown as triangles. Furthermore, the photocurrent was measured as the current from sample to ground at a laser intensity of $9 \mu\text{J}/\text{cm}^2$. While doing this, its quadratic dependence on laser intensity was assured to exclude saturation of the plasmon excitation at 0.1 nm and 2 nm deposition. The data are shown in open circles and are normalized to the 2PPE signal intensity in fig. 5.3(a). The highest current of 140 pA was obtained at 0.9 nm deposition.

For the 2PPE spectra intensity the hot electron contribution at low kinetic energy was deliberately left out. As it is due to secondary processes and relaxation it would manipulate the dependence. In contrast, the photocurrent represents an integral over the whole kinetic energy range and all emission angles.

The plasmon is excited resonantly at 3.6 eV [92] while the 3.16 eV excitation is far off-resonance. This is the reason for the different absolute intensities at the two excitation energies whereas their relative dependence on particle size is similar. Fig. 5.3(a) shows a linear increase up to 0.4 nm size and a subsequent leveling off until at 0.9 nm size the maximum is reached. The intensity then decreases slightly for higher deposition.

In fig. 5.3(b) the intensity is plotted versus the corresponding mean particle di-

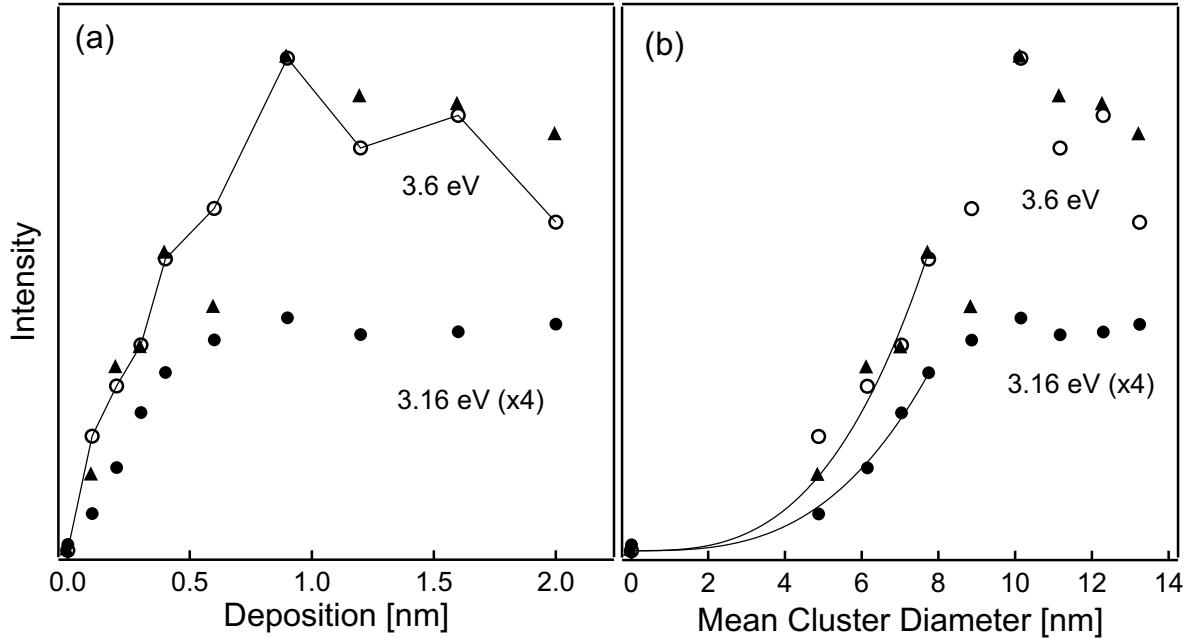


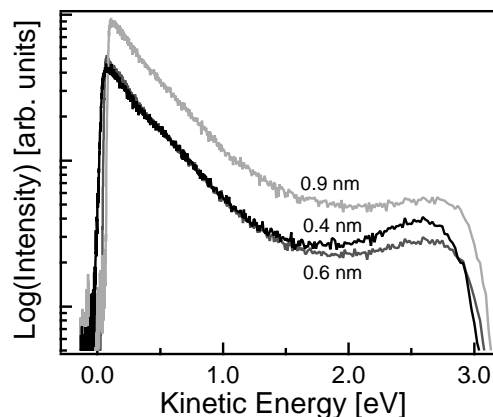
Figure 5.3: 2PPE intensity of Ag nanoparticles at $h\nu = 3.16$ eV (solid circles) and 3.6 eV (triangles) as functions of (a) silver deposition and (b) mean particle diameter. The photocurrent for $h\nu = 3.6$ eV is given by open circles. (b) The solid curves indicate a cubic fit to the 2PPE data.

ameter. Since the particle density per unit area stays constant (see sec. 3.2.2), the nanoparticle growth should be proportional to the deposited silver amount. The photoemission intensity in fig. 5.3(b) corresponds to a cubic fit up to 8 nm size suggesting a linear dependence on atoms per nanoparticle. The subsequent leveling off for sizes larger than 8 nm can be attributed to coalescence of adjacent particles. For 3.6 eV photon energy even a decrease in intensity occurs for 9 nm particles. Interestingly, such a decrease could not be recognized for the photocurrent which was monitored at the same time. Furthermore, the spectral shape changes dramatically, as can be seen in fig. 5.4. While the hot electron distribution remains constant compared to 8 nm particles the feature at high kinetic energy is decreasing.

We can think of the excited nanoparticles as oscillating dipoles perpendicular to the surface. The influence of adjacent particles will grow with increasing particle sizes, i.e. decreasing particle distance. It is reasonable to assume that an excited particle then will induce an antiphase oscillation in the surrounding particles. That leads to a weakening of the plasmon oscillation normal to the surface and related photoemission processes. For a more detailed study of the coupling of plasmon modes in adjacent particles see [91, 45].

Hot electrons, caused by secondary processes and scattering e.g. at the particle surface, have been confirmed to be isotropically distributed and may also stem from non normal excitations. Therefore, their distribution gives a measure for the absorption

Figure 5.4: Spectra for 3.6 eV photon energy. The feature at high kinetic energy decreased for 0.6 nm deposition. The indicated depositions correspond roughly to 8, 9, and 10 nm particles.



process in total.

The photoemission intensity at the plasmon resonance is for s-polarized light strongly weakened. A difference in intensity between p and s-polarization of more than two orders of magnitude was found. For 3.16 eV photon energy the relative hot electron distribution was independent of polarization and its intensity differed only by up to a factor of 8. This is a factor of two higher than the expected ratio according to the Fresnel equations of ≈ 3.5 [105]. However, there is the direct transition which is for p-polarized light more pronounced than for s-polarized light which may explain the deviation. Therefore, we can assume that in the latter case plasmon excitation plays only a minor role.

The feature at high kinetic energy, apparently due to a direct excitation process, will be studied in the next section.

5.2 Density of States of Silver Nanoparticles

For the investigation of the density of states we are only interested in the shape of the nanoparticle spectra. Although the applied photon energies correspond to the plasmon resonance no direct influence of the plasmon was found. Its only contribution seems to be an overall enhancement of the photoemission intensity. Therefore, intensities for different photon energies are normalized in the following. For actual intensities see sec. 5.3.

Furthermore, to enable the comparison between spectra of different photon energies, the electron kinetic energy is related to the Fermi level, i.e. replaced by $E - E_{Fermi}$. The Fermi level E_{Fermi} has been determined by the ToF-spectrometer calibration (sec. 3.1.2).

5.2.1 Change of Spectral Shape with Photon Energy

An unoccupied state in 2PPE can only be identified by varying the photon energy as already mentioned in the beginning of this chapter. In fig. 5.5 spectra of 6 nm particles are shown recorded at different photon energies as indicated at the right. For comparison the spectra are plotted relative to the Fermi level.

In the following we will focus on the feature near the Fermi edge in fig. 5.5. The black and shaded shapes at the bottom of each spectrum belong to the fitting and will be discussed later. It can be seen that the feature changes with photon energy implying the contribution of an intermediate state transition. However, an intermediate state should shift by $-\Delta h\nu$ relative to the Fermi level. The shift is actually much less pronounced and also the width of the feature increases. From 1PPE (see sec. 4) we know that there exists a state right below the Fermi edge. That gives rise to the assumption that in the current feature an occupied and an unoccupied state might be involved.

Let us consider the excitation of an occupied state via a broad intermediate state as illustrated in fig. 5.6. The transition is then more or less resonantly enhanced if the photon energy is changed. From Fermi's golden rule we know that the probability for the first photon excitation is proportional to the density of states in the final state, i.e. in this case the intermediate state. This is correct if the transition matrix elements do not change with particle size which will be assumed in the following. The density of the initial state is projected by the first photon excitation onto the density of the intermediate state, as indicated in fig. 5.6. To obtain the resulting intermediate state population we have to multiply the density distributions of unoccupied state and projected occupied state, i.e. $I(E_{intermediate}) \propto \varrho(E_{unoccupied}) \cdot \varrho(E_{occupied} + h\nu)$. The projection is illustrated at the left of fig. 5.6. The resulting maximum of a multiplication should be expected where both distributions show values considerably different from zero, i.e. in between the maximum of the projection and the intermediate one. This will result in an energy shift $\Delta E < \Delta h\nu$ to lower energy if the photon energy is increased.

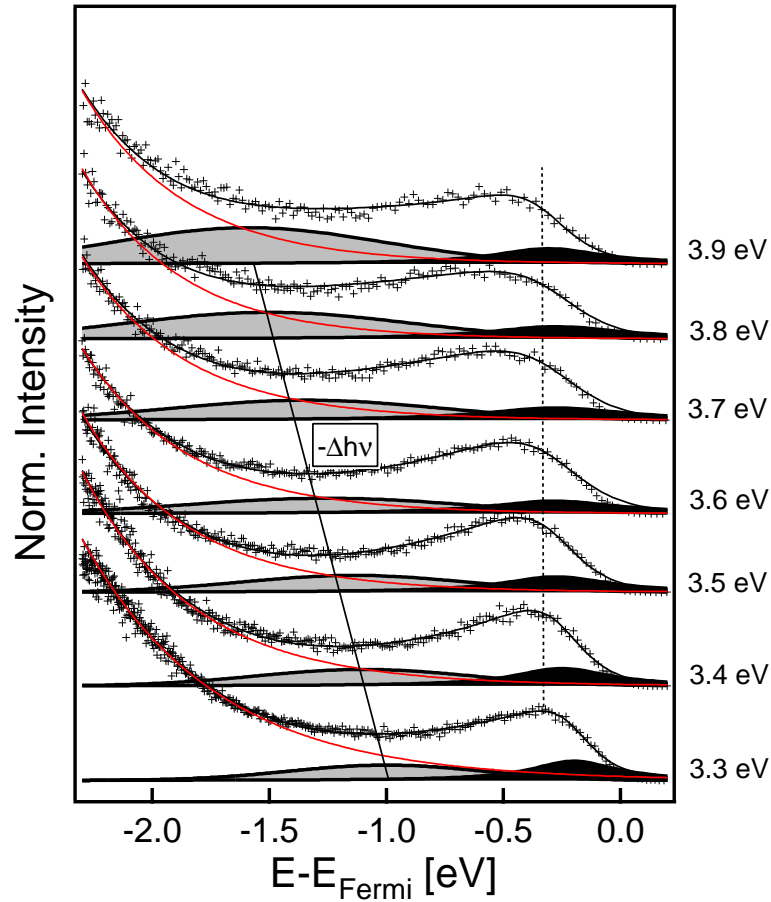


Figure 5.5: Spectra of 6 nm particles for different photon energies as indicated at the right. The integral of the spectra from -2 to 0 eV is normalized in intensity. For description of the fitting see the text.

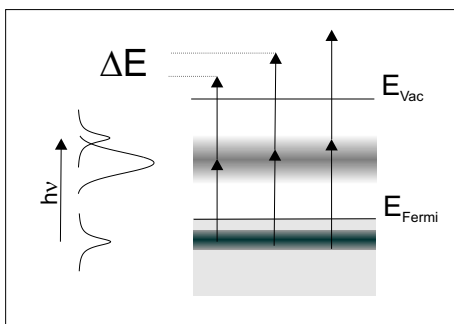


Figure 5.6: Diagram of a complex 2PPE Process. The occupied density of states is projected by the first photon excitation onto the unoccupied density of states.

Following these considerations we are able to disentangle the various contributions to the data. The hot electron distribution of each spectrum corresponds to an exponential function [127, 132], as can also be seen at low energies in fig. 5.4. This exponential contribution, indicated in fig. 5.5, is eliminated by subtraction. The residual feature near the Fermi edge of each spectrum is then fit in the following manner: As a fit function we assume the product of two distributions of arbitrary shape. At first the shape of a distribution is justified by the quality of the resulting fit to the data. The completing justification however gives the dependence

of the fit positions on the photon energy. In the beginning of this chapter we have already seen that in 2PPE only two shifts in dependence on photon energy are reasonable: An occupied state should not shift relative to the Fermi edge, while an unoccupied state should shift with $-\Delta h\nu$. This rule is not put into the fitting procedure but rather serves as an evaluation of the employed distribution shapes.

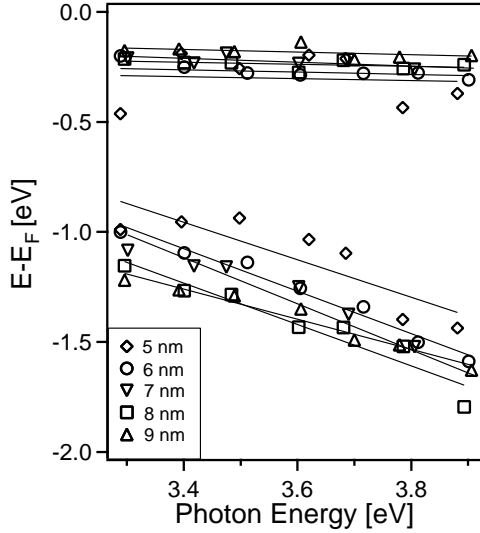


Figure 5.7: Peak positions obtained by multiplicative fitting for different particle sizes as indicated.

The positions obtained for different photon energies are given. Independent of particle size, the occupied state exhibits a slight shift with slope higher than $-0.06 \Delta h\nu$. This can be explained by the selectivity of the plasmon excitation and the particle size dependence of the occupied state as will be shown later. With increasing photon energy preferentially smaller clusters are excited.

The unoccupied state shifts generally with $-1 \pm 0.05 \Delta h\nu$. For 5 nm particles this value is only $-0.85 \Delta h\nu$ which we assign to the noise of the data. The noise is due to broader fit-distributions and a larger overlap of Gaussian and Lorentzian, making a determination of actual positions more difficult. At 9 nm particle size the intermediate state shift increased to $-0.7 \Delta h\nu$. This may be assigned to the interaction with other intermediate states as will be discussed later, leading to a deviation from a gaussian shape. Therefore, the analysis is not extended to larger particle sizes. As actual state positions the average of the data, obtained for different photon energies, are taken, in the case of the intermediate state position only after addition of the respective photon energy.

In fig. 5.8 peak positions and widths for different particle sizes are shown, analysed as previously described. Each particle size exhibits an unoccupied and an occupied state marked by a closed circle and an open circle, respectively. By assuming (111)-

Gaussian and Lorentzian distributions were tried for the multiplicative fitting. However, the only satisfactory result was obtained by applying a combination of a Lorentzian and a Gaussian distribution, as depicted in fig. 5.5. While the Lorentzian stays nearly constant in energy the Gaussian moves with $-\Delta h\nu$ corresponding to an occupied and an unoccupied state, respectively. The fit exhibits a slight mismatch with the data near the Fermi level. This is due to the cutoff by a Fermi distribution for the experimental data which was deliberately left out for the fitting so far. It turns out that the falling edge near the Fermi level can be well reproduced and is not due to a cutoff by the Fermi edge or charging effects [50, 121].

The multiplicative fitting has been carried out for various particle sizes as indicated in

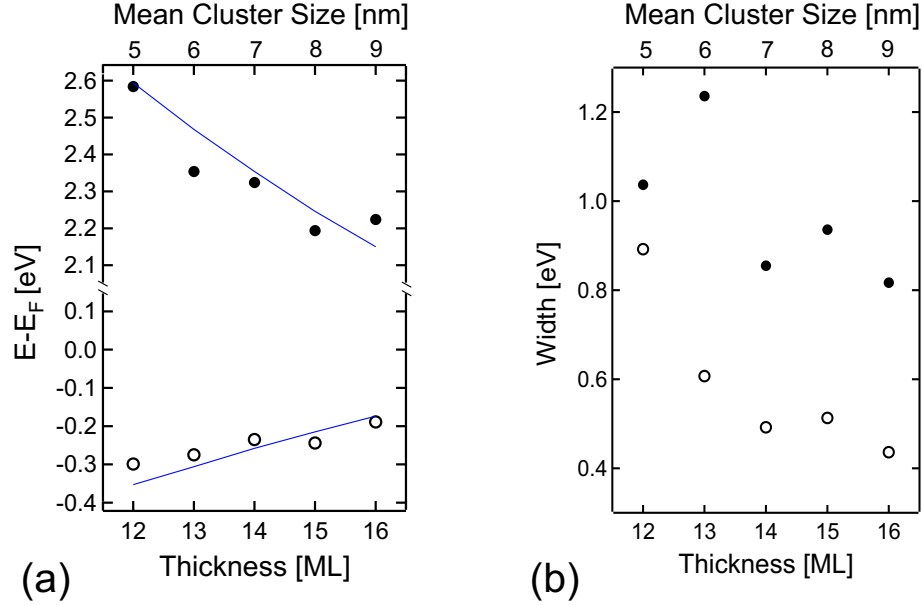


Figure 5.8: (a) States of different particle sizes are shown by circles. Slopes and positions are well reproduced by the assumption of quantum well states (solid lines). (b) Corresponding width of the states. The width diminishes with increasing particle size. Unoccupied states are considerably broader.

terminated nanoparticles, these states would be located inside the band gap which extends for Ag(111) from -0.31 eV up to 3.99 eV. In the case of occupied states the most plausible explanation would be again a Shockley surface state as already discussed in sec. 4. But this assumption leaves the origin of the unoccupied state unclear. Moreover, by STS no surface state was found on the nanoparticles although some of them exhibited a hexagonal shape, suggesting a well ordered structure and (111)-termination. However, STS revealed a series of quantum well states (QWS) on individual nanoparticles [93] which will be discussed in the following.

One could argue that for a broad particle size distribution as in the present case QWS should smear out since we are using an integrating method. For that reason we will have a closer look at the QWS equation derived in sec. 2.1 :

$$\Phi_{total} + 2kNd = 2\pi n \quad (5.1)$$

If we neglect for a moment the surface induced phase shift Φ_{total} we can solve the residual for the wave vector k :

$$k = \frac{\pi n}{dN}, \quad (5.2)$$

where d has been the interlayer distance. The only variables are n that enumerates the QWS, and N denoting the number of monolayers. That means that for each particle thickness N we can find an n with the same value such that equation 5.2 is simplified to $k = \frac{\pi}{d}$, the brillouin zone boundary (BZB). In other words: Whatever particle size

we are dealing with it should exhibit a QWS at the brillouin zone boundary, resulting in a commensurate state [53]. Around this state also other states should show up even if the particle size distribution is broad. As the band gap of Ag(111) is located at the BZB, it is not unlikely to find the commensurate state inside the accessible energy interval.

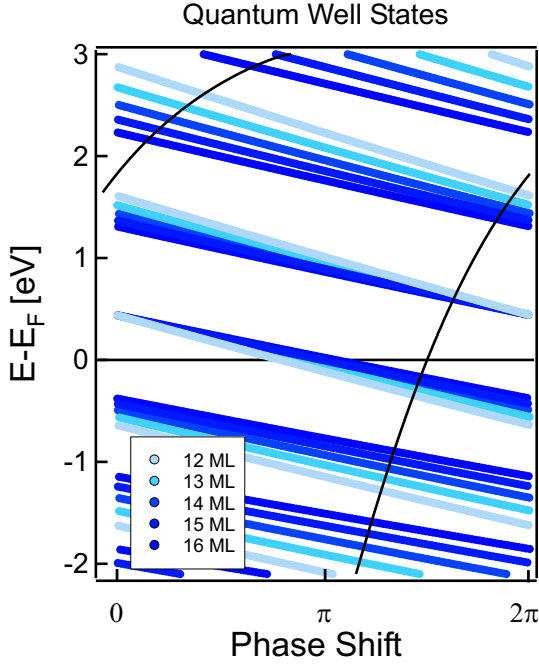


Figure 5.9: Quantum well state condition. Phase shifts (straight lines) for different particle thicknesses as indicated in the inset are plotted. They meet at the commensurate point at 0.44 eV. At the intersection points with the negative surface induced phase shift (curved line) quantum well states are expected.

To relate equation 5.1 to energy, a free electron like dispersion was assumed, which will be discussed later. In fig. 5.9 the straight lines show phase shifts induced by the second term in equation 5.1 for different thicknesses N . The corresponding thicknesses are given at the bottom of fig. 5.8(a). The bright line corresponds to the lowest thickness, the darkest line to the largest thickness. As black curve the negative total phase shift Φ_{total} is given. At the intersection points of the curves the condition for a QWS is fulfilled.

As expected, the phases for different thicknesses converge while approaching the commensurate point, here located at 0.44 eV. Interestingly, their order reverses after passing this point reflecting the reversed slope of the data. The sp-band bottom has been adjusted to -6.3 eV which reproduces the data quite well as indicated by the lines in fig. 5.8(a). The lines correspond to intersection points in fig. 5.9 between 2 and 3 eV, and those right below 0 eV, respectively. The assumed thicknesses correspond to an aspect ratio (height to width) of 0.58 for 5 nm particles down to 0.43 for 9 nm particles. This is in good agreement with a mean aspect ratio of 0.5 found by STM where also a flattening for bigger nanoparticles was observed [90].

QWS may also explain the broader width of unoccupied states in fig. 5.8(b) by the inhomogeneity of the sample: As they are further away from the commensurate point

at 0.44 eV, differences for adjacent thicknesses become more pronounced than in case of the occupied states (See fig. 5.9). Also the size dependent broadening of states can be attributed to inhomogeneity, roughly scaling with the square of the reciprocal particle thickness (see equ. 5.2).

The fact that we can match the data by the assumption of a free electron like dispersion seems to be surprising at first glance. However, it gives a simple explanation for the existence of states where we expected the band gap for Ag(111) to be. Besides, the QWS series found by STS could be detected up to 1.5 eV without showing any influence by a band gap. They were also well reproduced by the assumption of a free electron like dispersion [93]. This can be explained by the assumption of a disordered arrangement of the atoms in a nanoparticle, prohibiting the formation of a crystalline band structure. Such a change of the electronic structure gives additionally an explanation for the missing sp-intraband transition peak on nanoparticles which is prominent on Ag(111) (see sec. 5.1).

By taking a look at fig. 5.9 we see that there are additional intersection points, especially at energies in between the detected ones. The respective QWS we will investigate in the next section.

5.2.2 Influence on Density of States by Cs Deposition

The energetic position of a QWS depends among others on the surface induced phase shift. At the vacuum side this phase shift is determined by the work function. Therefore, a change in work function should influence the position of the previously discussed states. The higher their energy the bigger the influence should be. In the following the work function will be lowered by deposition with cesium [89, 95, 128]. The results will be discussed by comparison with simulations.

At the top of fig. 5.10 spectra of 7 nm particles are shown at 83 K. The spectrum at the top shows the bare nanoparticles which are subsequently deposited with Cs by up to a quarter of a monolayer. The deposition leads to a shift of the vacuum cut-off to lower energies as the work function decreases. At the same time additional features show up at low energies and also the feature at high energy changes. The hot electron contribution was eliminated by subtraction of an exponential from each spectrum for the sake of a better illustration. We made sure that the subtraction had no influence on the position of the features.

At the bottom of fig. 5.10 the simulation of a QWS distribution is shown using the same parameters as in the previous section. For matching to the experimental data the particle size distribution was assumed to be Gaussian with a width of half the particle thickness. The width of each single state was 0.5 eV. Following the spectra from the top on, the work function was changed in total by the same amount as for the 2PPE data. As expected, the influence of the work function is very strong for high energy states and becomes weaker for lower energy states.

If we compare the 2PPE data with the simulation we have to keep in mind that

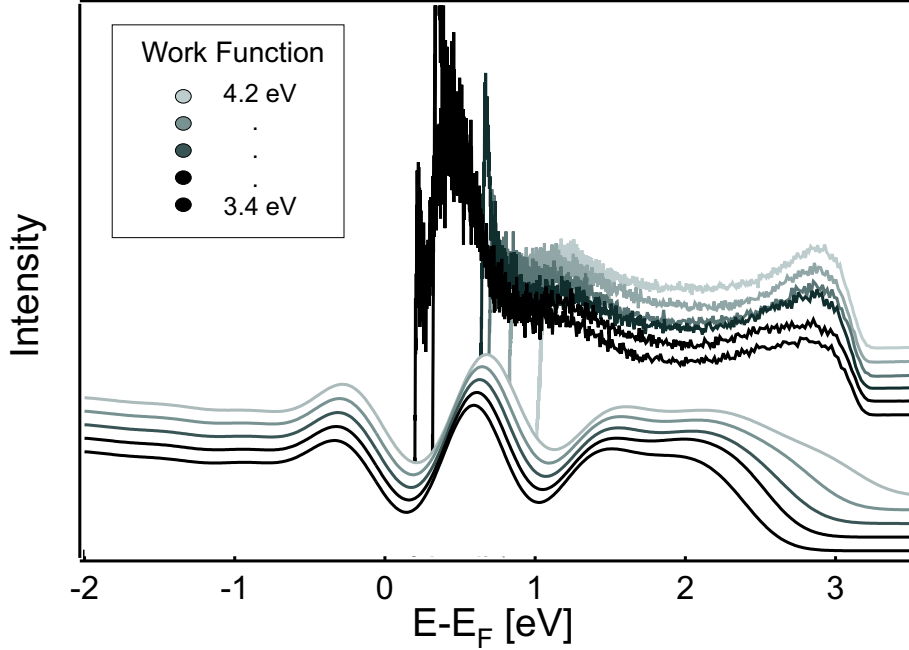


Figure 5.10: At the top a 2PPE spectrum of 7 nm particles is shown at $h\nu=3.15$ eV. The work function is subsequently lowered by Cs deposition as can be seen from the low energy cutoff. At the bottom a simulation for a broad particle size distribution for 7 nm particles is shown. The work function is changed in analogy to the experimental data as indicated in the inset.

the 2PPE data is a result of the projection of the occupied density of states onto the unoccupied density of states. In the case of the 2PPE feature at high energy the shape is significantly different to the simulated density of states. This is in fact not surprising since we know from the previous section that we are probing at that point the transition from an occupied state via an unoccupied state. The simulation reveals that the occupied state at about -0.3 eV is hardly influenced by the work function change while its counterpart at high energy ($+3.15$ eV) is strongly affected. If we apply again the previous fitting to the discussed feature in 2PPE, we get the very same dependence as for the simulation, shown in fig. 5.11. The relative shift of the falling edge of the simulation at high energy is given by a line.

It has to be mentioned that in this case the high energy feature had to be extracted by matching the s-polarized spectrum to the p-polarized one. An anomalous contribution from the s-polarized spectrum to the feature could not be excluded. That may be the reason why the positions in fig. 5.11 are shifted to higher energy. Therefore, the data reflect only a relative trend.

For the residual features the analysis should be simpler. As was shown by 1PPE no additional feature exists down to -2.5 eV. This was also reproduced by the simulation in fig. 5.10. Therefore, in this energy range, it can be expected that the two-photon

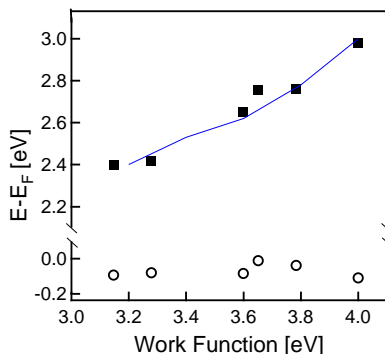


Figure 5.11: Influence on the nanoparticle states by a Cs induced work function change for 7 nm particles ($h\nu=3.15$ eV). The line represents the relative positions of the corresponding simulation.

excitation of the smooth occupied density of states reflects the intermediate density of states. By comparison of the lowest spectra of 2PPE data and simulation, respectively, we can identify the commensurate state at around 0.5 eV and the sequential state at around 1.2 eV, which only shows up as a shoulder. The positions of these states differ in energy compared to the simulation by about 0.15 eV.

One may argue that latter features could be due to cesium. However, the deposited amount was only a quarter of a monolayer performed at 83 K. Cesium then is supposed to aggregate in small nanoparticles or even atomically due to the strong dipole repulsion between atoms. In fact a contribution of those nanoparticles could be detected exhibiting an additional vacuum cutoff at lower energy, but the intensity was about two orders of magnitude lower. Furthermore, the commensurate state could also be detected for bare 5 nm silver particles using 3.9 eV photon energy.

The sp-band dispersion of the bulk in Ag(111) direction around the Fermi energy can be well reproduced by a nearly free electron like dispersion by adjusting the sp-band bottom to -4.9 eV. This is in disagreement with the value of -6.3 eV chosen for the free electron like dispersion. For a matching of the commensurate state to the simulation we would even have to lower the bottom to -6.45 eV. This would mean a broadening of the lower sp-band branch of 22 percent. However, for the simulation we assumed an interlayer distance of 2.36 Å in agreement with Ag(111). For a disordered nanoparticle the mean interlayer distance should be considerably higher correcting the assumed broadening of the sp-band.

To summarize the results obtained by cesium deposition, we have been able to explain the extended density of states of nanoparticles by the assumption of quantum well states, too. This includes the influence of the observed work function change by deposition with cesium. The experimental features could be qualitatively reproduced by a QWS simulation of a broad particle size distribution, assuming a free electron like sp-band structure.

5.2.3 Discussion of One and Two-Photon Photoemission Results

So far the density of states of the nanoparticles recorded by 2PPE could be explained quite well by QWS. In order to obtain a complete picture, we should be able to explain the 1PPE results of sec. 4 by QWS, too. Therefore, we first look again at the influence of a work function change on the occupied nanoparticle state near the Fermi level, shown in fig. 5.12.

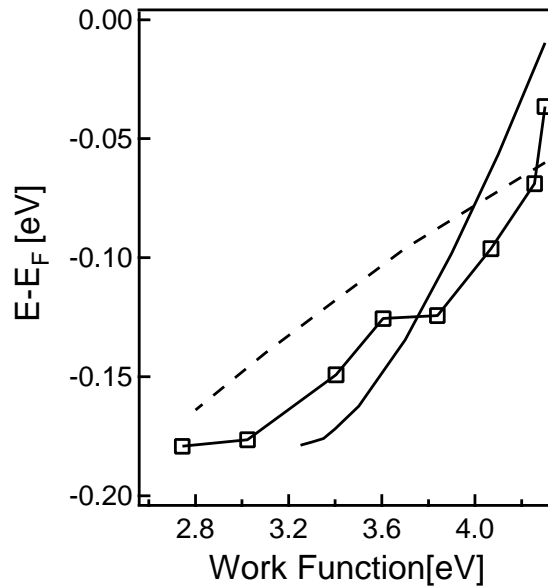


Figure 5.12: 1PPE data of 20 Å Ag deposition. In sec. 4 the state was interpreted as surface state by comparison to the phase accumulation model (solid line). The shift in dependence on work function can also be explained by the assumption of a Quantum Well State and 19 ML particle thickness (dashed line).

The trend was described with the phase accumulation model by the assumption of a surface state (solid line). For matching a shift of the sp-band edge of +0.13 eV had to be assumed. However, the same trend can be reproduced by QWS for a particle thickness of 19 ML (dashed line), using the same parameters as in the previous section. Note that both the slope and the position of the dashed line strongly depend on particle thickness. The assumed thickness corresponds to an aspect ratio (height to width) of 0.34, following the previously recognized trend of flattening with growing particle size². By adopting this aspect ratio, we have to correct the 1PPE thicknesses of fig. 4.3. These were initially calculated by the rough estimate of an aspect ratio of 0.5 due to

²Due to coalescence we should have particle strings for larger deposition thicknesses applied in 1PPE decorating step edges and alumina domain boundaries

the lack of an accurate value. These corrected 1PPE results will be compared with the 2PPE data.

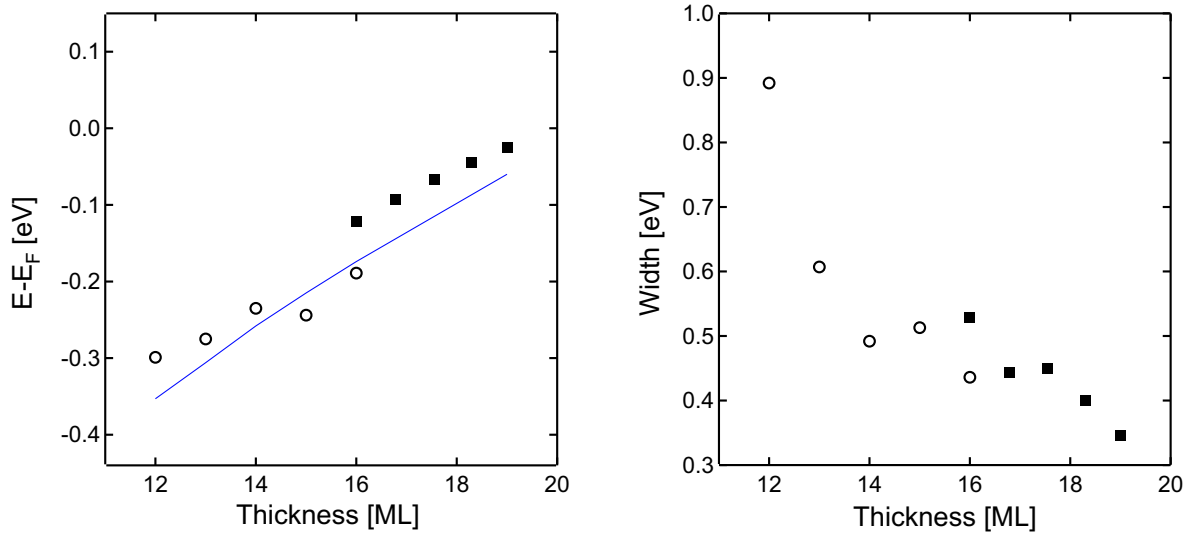


Figure 5.13: (a) 2PPE data are given by circles, 1PPE data by squares. The occupied state is well reproduced for both methods. The solid line represents the quantum well state position expected for parameters used in the previous section and particle thicknesses as indicated at the bottom. (b) Corresponding width of the states. The width diminishes with increasing particle size.

In fig. 5.13(a) 2PPE data are shown as circles, 1PPE data as squares. The occupied state is well reproduced with both methods, also the slope for the dependence of the energetic position on particle thickness is similar in both cases. However, 1PPE and 2PPE data exhibit slight deviations which will be discussed below.

The occupied states in 1PPE exhibit a small offset of 50 meV compared to the 2PPE data. Recently it was reported that the photoemission process on Ag(111) differs for 1PPE and 2PPE in respect to the vector potential coupling to the surface [101]. Furthermore, in 2PPE plasmon excitation is involved which may cause different lifetimes for the excitation processes. A longer lifetime of the created electron-hole pair would shift the detected feature to lower energy. Such a behaviour would also be reflected in the width of the states which is smaller in case of 2PPE (see fig. 5.13(b)). Both effects are in agreement with a model proposed by Hövel et al. [50].

We used two ways to determine the Fermi level. One is given by exploiting the TOF-calibration (see sec. 3.1.2), the other by employing the fitting with a Lorentzian and a Fermi distribution as cutoff. The fitting gave the Fermi level 50 meV lower than the calibration. Such a shift could be explained by a longer lifetime of the electron-hole pair on nanoparticles compared to the bulk, also stated in [50]. The data in fig. 5.13(a) are related to the Fermi level given by the calibration, so 1PPE data are corrected by -50 meV compared to fig. 4.3.

However, the analysis of both the 1PPE and 2PPE data is not so straightforward and a deviation of 50 meV lies within the error bar. Also the excitation differs in both cases. While in 1PPE the sum over all occupied nanoparticle states is directly probed, in 2PPE the sum over all transitions per nanoparticle is probed. These transitions are resonantly enhanced by an intermediate state. With varying particle size both the occupied and unoccupied state move to opposite direction, narrowing the resonance condition. This manifests itself in a smaller width for the 2PPE data in fig. 5.13(b).

Following the above considerations, the 2PPE results should considerably differ from the 1PPE results if inhomogeneously broadened. This is actually not the case. Rather, the detected widths can be basically assigned to lifetime broadening as it was observed for silver films of similar thicknesses [82]. There, the observed QWS showed similar widths depending on film thickness, too. Their broadening with decreasing film thickness was attributed to enhanced surface scattering and therefore to a reduced lifetime.

By employing the aspect ratio of 0.34 for 20 Å deposition found above, we can extend the expected QWS positions of fig. 5.8(a) to higher deposition (solid line in fig. 5.13(a)). Aspect ratios in between 16 ML and 19 ML are interpolated. The result is a linear increase which reflects the slope of the data quite well.

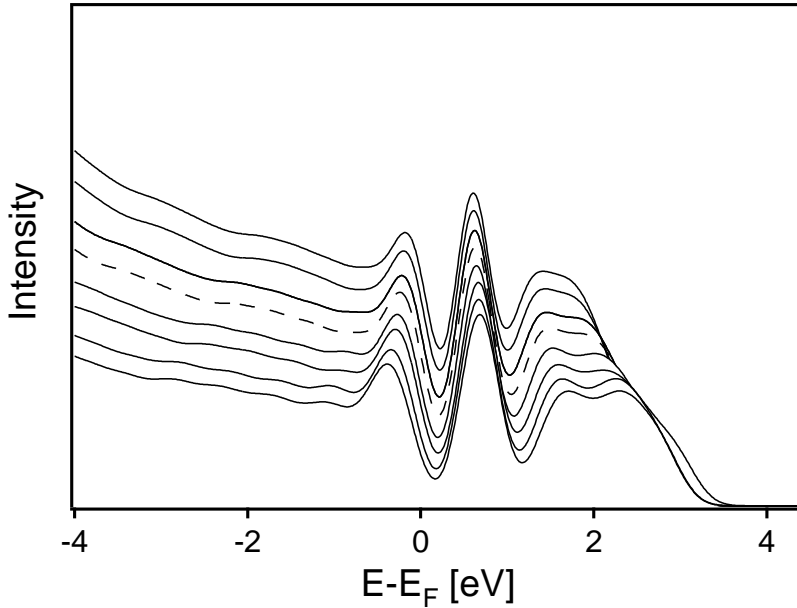


Figure 5.14: Quantum Well structure simulations for thicknesses of 12 ML to 19 ML, corresponding to depositions of 1 Å to 20 Å silver (from bottom to top). Dashed line: 16 ML.

In fig. 5.14 simulations of the density of states by QWS are shown for particle thicknesses of 12 ML (low intensity) up to 19 ML (high intensity). They correspond to silver depositions of 1 Å up to 20 Å, respectively. The dashed curve marks 16 ML

thickness, i.e. 6 Å silver deposition, accessible for both 1PPE and 2PPE. Parameters being used correspond to those of the previous section.

Now we focus on the feature beneath the Fermi level. Although its shape is the result of an overlap of a QWS distribution of Gaussian shape, it fits well to a Lorentzian at low energy side. The high energy side however is much steeper, coinciding with the Fermi level. If we try to fit the corresponding photoemission spectra by a Lorentzian and a Fermi distribution as cutoff, the resulting Fermi level will be located below the real one. This gives an alternative explanation for the disagreement found above.

To summarize we have seen that all effects we tried to explain by surface states in sec. 4 can be alternatively explained by QWS. Moreover, QWS allowed an interpretation where surface states failed, e.g. the lifetime broadening or the linear shift of the occupied state with increasing particle size. Furthermore, the interpretation of the unoccupied states as QWS requires an occupied QWS at the position in dispute.

5.3 Plasmon Resonance Shift with Particle Size

The energy of the plasmon resonance as a function of particle size has been intensely studied by Photon-STM [92]. Exploiting the radiative decay channel of the plasmon excitation, the emitted light was detected to determine its resonance position. Another decay channel of the plasmon excitation is the coupling to electrons. These electrons can be detected by 2PPE. The common way to determine the resonance position of the plasmon with 2PPE is to tune the photon energy. The integral over a certain energy range of the obtained photoemission yield then is supposed to reflect the intensity of the plasmon excitation [110, 80]. However, the 2PPE yield also depends on the density of states of the nanoparticles. This density of states is usually not known and may distort the results. However, in the present case the density of states is known, demanding a correction of the plasmon resonance shape obtained in the above described manner. This will be carried out below.

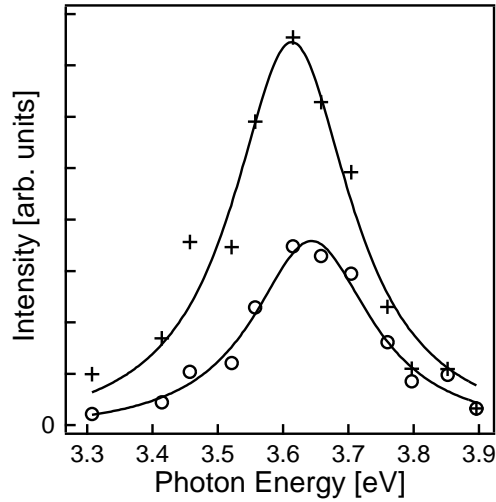


Figure 5.15: 2PPE intensity integrated from E_F to $E-E_F=-1$ eV as a function of photon energy, indicated by crosses. The corrected dependence is given by circles. Curves are fit by Lorentzians.

In fig. 5.15 the integrated 2PPE intensity of 7 nm particles is shown as crosses for different photon energies. The integrated energy range of the spectra extends from the Fermi edge projection to 1 eV lower kinetic energy. This is the common procedure aiming to avoid a contribution from the hot electrons. However, as we know from the previous chapter, the feature we are integrating over belongs to a resonant transition via an intermediate state. This transition depends on photon energy and is more resonant for lower photon energies than for higher photon energies (see fig. 5.8). If we correct this contribution by assuming the transition at 3.9 eV as non resonant we obtain the curve given by the circles.

The correction was carried out as follows: Since the normalized spectra in fig. 5.8 had to be fit by the product of two distributions, their relative intensities are not known. Therefore, the integral over the occupied state distribution was assumed to be independent of the photon energy such as the normalized spectra are. The result can be seen in fig. 5.8 which leads to a growth of the intermediate state distribution with photon energy. Drawing the same approximation of constancy for the intermediate state distribution, we can extract a correction factor for photon energies lower than 3.9 eV. This correction is applied to the original data points in fig. 5.15.

The most remarkable result of the correction is that at 3.3 eV photon energy the intensity decreases by a factor of 5. The correction factor increases nearly exponentially with decreasing photon energy. This suggests that the strong photoemission enhancement for silver nanoparticles at $h\nu=3.16$ eV found in sec. 5.1 is mainly due to the intermediate QWS transition, which can be estimated to cause a factor of 10. Furthermore, it can be seen that the Lorentzian fit to the data in fig. 5.15 matches better in case of the corrected curve. Also a slight shift to higher energy for the correction occurs.

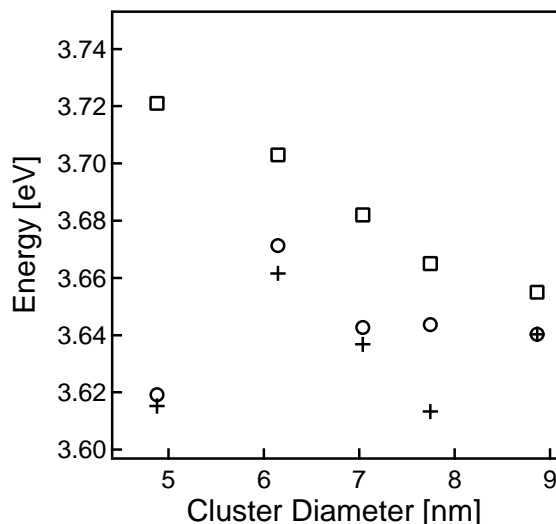


Figure 5.16: Position of the plasmon resonance for different particle sizes. The uncorrected position is indicated by crosses, the corrected position by circles. The squares show Photon-STM data.

Fig. 5.16 shows the plasmon resonance position for different particle sizes. Crosses represent the original maximum position, circles the corrected position. The position for 9 nm particles was not corrected since the shape of the intermediate state was not accurately determined. The reason why the resonance for 5 nm particles does not follow the usual blue-shift is unclear. The squares show the data from Photon-STM. Although the data correction provides a better matching to the STM data, this picture only gives a qualitative impression, since the error bar for the STM data extends over

0.1 eV.

Summarizing we have shown that the quantum well state transition demands a correction of the common determination of the plasmon resonance in 2PPE. Although the broad width of involved states caused only a slight correction of the resonance position, the low energy wing of the resonance was strongly decreased. This suggests that the enhanced photodesorption cross section observed for NO for the present system at $h\nu=3.2$ eV [105] is not plasmon induced but rather due to the enhanced intermediate state transition. However, there is a difference between the observed photoemission enhancement at $h\nu=3.16$ eV on nanoparticles compared to Ag(111) of 100 and the estimated enhancement due to the QWS transition of 10. The missing factor of 10 has to be assigned to altered properties of the nanoparticles, e.g. a longer lifetime of excited electrons [79].

5.4 NO Adsorption on Ag(111) and Nanoparticles

For the study of fundamental processes in photodesorption usually simple molecules are chosen in order to reduce complexity. NO is a well investigated molecule which exhibits its first and second electronic excitation in the near UV allowing resonant ionisation (REMPI) by commercial dye lasers. This process is state selective and therefore provides information about its electronic, vibrational, and rotational quantum numbers, giving insight into the desorption process itself [2, 1, 133]. For that reason, the influence of adsorbed NO on the properties of Ag(111) and silver nanoparticles is investigated in the following.

5.4.1 Ag(111)

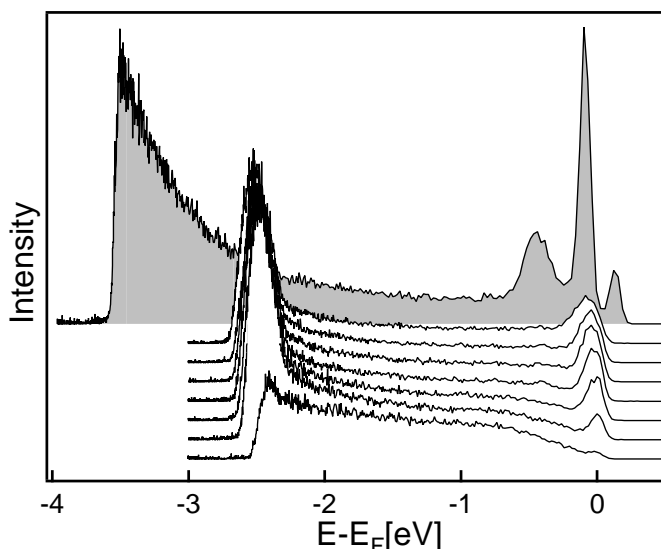


Figure 5.17: Ag(111) spectra for 4.1 eV photon energy at 77 K. In the front a spectrum for NO saturation coverage of 2 L is shown. Every 300000 laser shots sequentially a new spectrum was recorded. In the back a spectrum for the clean Ag(111) surface is shown.

In the back of fig. 5.17 the 2PPE spectrum of a Ag(111) crystal is shown at 77 K and $h\nu=4.1$ eV. Three peaks show up around the Fermi level. The most pronounced one belongs to the surface state, the peak at the low energy side to the first image state and the other peak to the second image state. In the front a spectrum of the NO saturated sample is shown where all three features are quenched and only a small peak can be perceived at the Fermi edge. Further, the work function increased by 1.1 eV and a broad feature appears around -1 eV.

After sequential exposure to the laser light a peak at the Fermi edge recovers and shifts to lower energy, stopping finally at the original position of the surface state. The

broad feature at -1 eV disappears but the work function changes only very slightly. After laser irradiation also another feature arises at low energy.

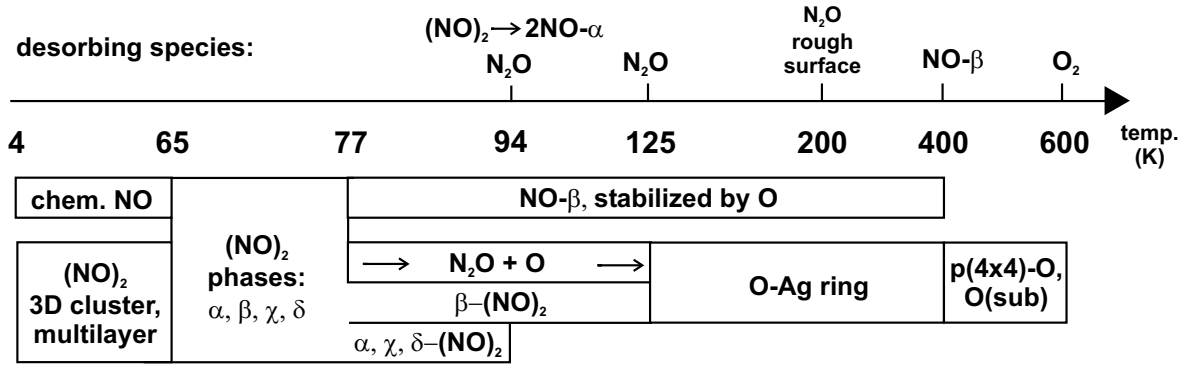


Figure 5.18: Temperature dependent NO chemistry on Ag(111). (NO)₂ is considered as major photoactive species which splits into monomers upon desorption. The photoactivity of NO-β is of minor relevance.

Fig. 5.18 depicts the temperature dependent chemistry on Ag(111) upon adsorption of NO, extracted from [115, 26, 125]. NO tends to form dimers with different configurations which can also split into N₂O + O. These dimers are considered as photoactive species. During laser irradiation they split into NO monomers which desorb subsequently. On Cu(111) a NO induced feature was detected at 1.8 eV and attributed to the 2π* orbital of NO [56]. For the density of states of NO on Ag(111) see also [38] and references therein. In fig. 5.17 the position of the 2π* orbital would correspond to -2.3 eV which is here close to the vacuum cutoff. Only after exposure to laser light a feature rises around this energy.

By NO adsorption the surface state followed the change in work function according to the phase accumulation model (not shown here). The recovering of its original position during laser irradiation therefore implies the depletion of the surface. However, the work function changed only very slightly and gives rise to the following speculation. The laser light preferentially splits the dimers which may correspond to the broad feature at around -1 eV. Thus, the feature vanishes and at the same time NO monomers are produced. Some of them desorb but some may remain at the surface giving rise to the feature at -2.5 eV. This may lead to a partial depletion of the surface. The constant work function can be attributed to the photoinduced generation of different species.

A similar feature at the vacuum cutoff also shows up in the case of silver nanoparticles (fig. 5.20). However, it seems always to be located at the vacuum cutoff independent of the work function. For determination of the origin of the feature we would have to tune the wavelength in order to see an influence on an unoccupied state. This is not possible as the applied photon energy is already at the accessible maximum at hν=4.1 eV. Furthermore, the ongoing photochemistry changes the spectral shape while tuning the wavelength, making an analysis more difficult.

Now we come back to the states around the Fermi level for the clean surface. After NO coverage the surface state recovers during exposure to laser light, not so the image states. This can be attributed to their different origins and properties (see sec. 2.1.1). A similar behaviour as for the surface state is expected for the quantum well states on nanoparticles, as will be employed later. These states extend only little into the vacuum and are therefore not expected to be "poisoned" by NO, either.

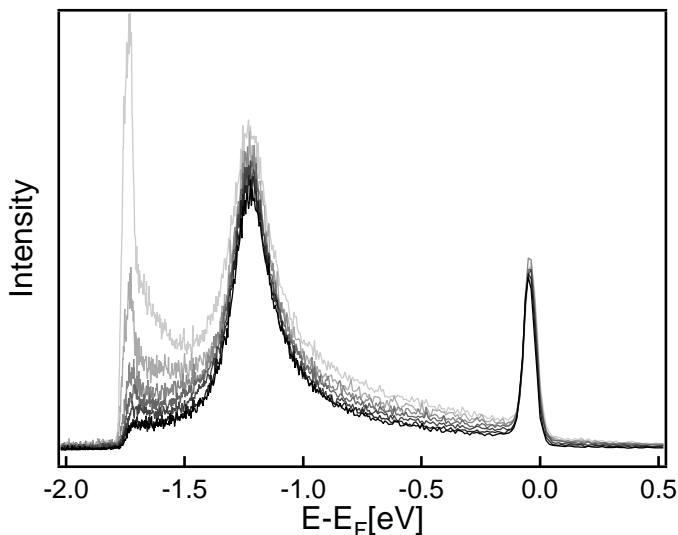


Figure 5.19: Ag(111) spectra for 3.16 eV photon energy at 83 K. The spectrum with high intensity belongs to the clean surface which is progressively exposed to NO until saturation at 1.5 L.

At higher temperature Ag(111) shows a completely different behaviour as depicted in fig. 5.19. The intensity of the clean sample, i.e. the hot electron distribution, is strongly quenched at low energies after exposure to NO. However, features like the sp-intra band transition and the surface state seem not to be affected. Also the work function doesn't change suggesting that there is no NO adsorbed on (111)-facets but only at defect sites. This interpretation was also confirmed by TPD measurements. Only a diffuse background showed up in contrast to the well defined signal from the NO covered Ag(111) surface [125].

From photoelectron emission microscopy (PEEM) on Ag(111) it is known that defects can be the origin of so called "hot spots" which show high electron emission intensity if exposed to laser light. These "hot spots" are related to surface plasmon excitation [64, 119].

By comparison with literature it turns out that the spectral shape for NO saturation in fig. 5.19 is similar to spectra of defect-poor Ag(111) surfaces [101]. This gives rise to the assumption that NO, sticking at defect sites, quenches the "hot spot" or surface plasmon excitation. This excitation turns out to manifest itself in hot electrons which cannot be resolved with PEEM. Different to the plasmon excitation on particles, the

surface plasmon excitation on rough surfaces seems not to couple to states on smooth facets as can be seen in fig. 5.19. For a roughened silver surface, prepared as for photodesorption experiments in [125], no enhancement of the photoemission yield for p-polarized light has been observed, either.

5.4.2 Nanoparticles

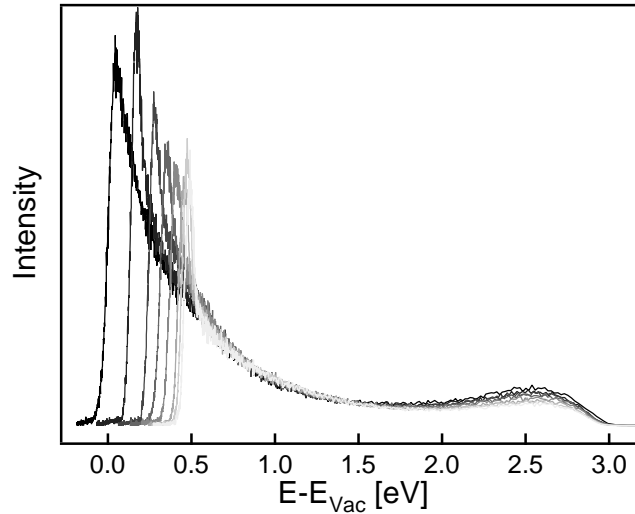


Figure 5.20: Spectra of 7 nm Ag particles progressively exposed to NO at 83 K and excited at plasmon resonance (3.6 eV). Spectra are normalized at 1.5 eV.

Fig. 5.20 shows spectra of Ag nanoparticles at 83 K. The intensity is strongly quenched by sequential adsorption of NO but normalized at 1.5 eV for comparison of the spectral shape. Also the work function increases and the well known feature at 2.5 eV (see sec. 5.2) becomes smaller compared to the hot electron signal.

From sec. 5.2 we know that there is a resonant transition which is influenced by a change in work function. As the work function increases this influence should manifest in intensity enhancement while here it is diminishing. Nevertheless this effect should play a minor role because the change in work function is smaller than 0.5 eV and involved states are very broad.

In fig. 5.21 the intensity of the 2.5 eV feature is plotted versus the change in work function. The intensity decreases by a factor of 19 and matches thereby to a quadratic fit. On Ag(111) no quenching due to NO was recognized. Furthermore, by using a photon energy of 3.16 eV for the same particle size the quenching factor by NO was only 3. This suggests that the observed decrease in intensity is due to a quenching of the plasmon excitation as previously observed on rough Ag(111) in fig. 5.19. A relation between plasmon quenching and work function change will be established in the following.

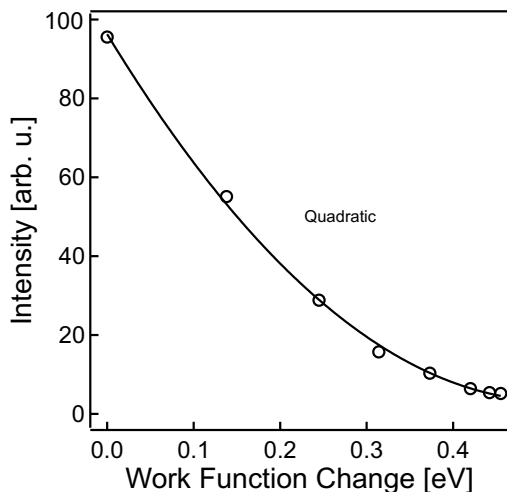


Figure 5.21: Intensity of the feature at 2.5 eV in fig. 5.20 versus the change in work function. The solid curve represents a quadratic fit to the data.

A change in work function can be regarded as a measure of the charge transfer between the adsorbate and the substrate. As the work function is increasing by NO adsorption we can expect a net charge transfer from the substrate to the adsorbate. This charge transfer was attributed to a mixing between the NO $2\pi^*$ level and the metal 5s electrons [54]. Therefore, we can assume that the 5s electron density in the particle is reduced by NO adsorption. On the other hand, employing the Thomas-Reiche-Kuhn rule, the oscillation strength of the plasmon excitation is proportional to the electron density, i.e. the 5s electrons in this case. Thus we end up with a linear relation between plasmon excitation strength and the inverse of the adsorbate induced work function change. Consequently, the quadratic intensity dependence on work

function in fig. 5.21 suggests twice the contribution of the plasmon excitation to the photoemission, giving evidence that each excitation step in 2PPE is driven by plasmon excitation. This is also confirmed by two-colour experiments in section 6.2.

A decreasing 5s electron density due to NO adsorption should also result in a redshift of the plasmon resonance. A determination of this shift by 2PPE would only be possible by scanning the photon energy, resulting in changing conditions due to induced photochemistry. However, the decrease of the photoemission at $h\nu=3.16$ eV by a factor of 3 on NO covered particles puts minor importance on such a shift.

In fig. 5.22 the measured work function change versus NO exposure is plotted. Again, we will try to find a relation between both values by employing the Langmuir assumptions [67]. For that purpose we introduce $\theta(t)$ as the time dependent coverage on the surface during exposure with values between 0 and 1. The amount on vacancies then is given by $1-\theta(t)$, provided that the density of adsorption sites and the sticking coefficient is independent of coverage. For a constant background pressure P we obtain the variation of $\theta(t)$ with time of exposure:

$$\frac{d\theta(t)}{dt} = b(1 - \theta(t))P, \quad (5.3)$$

with b as proportionality constant. The solution is given by

$$\theta(t) = A \cdot (1 - e^{-bPt}), \quad (5.4)$$

with Pt denoting the exposure. This equation is fitted to the data in fig. 5.22 by the solid curve reproducing the trend quite well. It suggests either that parameters as

adsorption site density or sticking coefficient change, leading to an accidental matching, or otherwise that the NO coverage θ is proportional to the work function, as has been found for O₂ on silver [34]. In the latter case the interaction between single molecules at the surface would be of minor relevance, excluding dimer formation as depicted in fig. 5.18. This could be interpreted as due to a nanoparticle structure different from Ag(111).

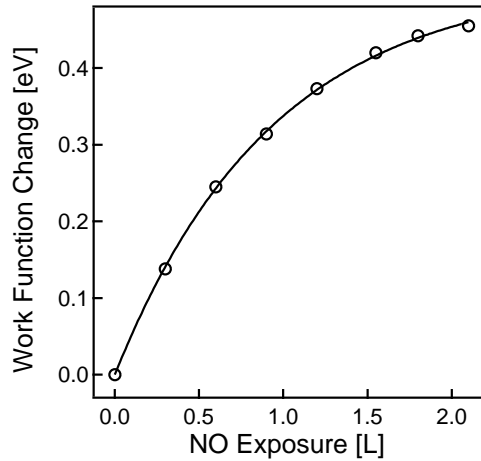


Figure 5.22: Work function change of 7 nm particles in dependence on NO exposure. For the fitting (solid curve) see the text.

nanoparticles even an increase of the plasmon resonance intensity was observed. The accompanying change of the resonance could be solely attributed to the altered dielectric surrounding [65]. For CO covered silver nanoparticles no shift of the plasmon resonance was found for particles larger than 4 nm [28].

It turns out, that NO frustrates a plasmon induced desorption from silver nanoparticles. Likewise, the enhanced photodesorption cross section of NO on silver nanoparticles observed in [132] is not supposed to be plasmon induced. Rather, it could be caused by intermediate state transitions as in the present case or altered properties of nanoparticles due to confinement, e.g. the reduced hot electron transport efficiency into the bulk [79].

It may be argued that the decrease in intensity is not necessarily due to quenching of the plasmon. However, a shift of the plasmon resonance by NO adsorption as explanation for the quenching seems not likely. With decreasing electron density the resonance should shift to lower energy, as reported for SO₂ adsorption on 30 nm silver particles, where a shift of 50 meV was observed [46]. A pronounced shift would lead to an intensity increase at 3.16 eV in contrast to the observed decrease by a factor of 3. This decrease however may be caused by a weakening of the quantum well state transition due to NO, partly contributing to the observed quenching at plasmon resonance.

Interestingly, no reports on plasmon quenching by adsorbates were found in the literature. For H₂O adsorption on silver

Chapter 6

Two-Colour Experiments

The electronic excitation of adsorbates mediated by the substrate plays a key role in surface photochemistry. These substrate mediated excitations are mostly caused by electronic transitions into unoccupied molecular orbitals. Therefore, the electron dynamics with respect to excitation, population, and relaxation processes at the surface is a decisive parameter. Likewise, the energy dependent residence time of excited electrons above Fermi level limits the transition probability into adjacent adsorbate orbitals. As these processes proceed on a femtosecond time scale, only few methods are capable to allow an investigation in the time domain [99, 111, 37]. In this work, femtosecond time-resolved 2PPE spectroscopy is employed by cross-correlating two pulses in a pump-probe scenario. To enable the differentiation between single excitation steps, in the following pulses of different colours are used. An introduction to time resolved two-colour experiments is given by illustrating the rate-equation model.

6.1 Rate-Equation Model

In the following lifetime effects are dealt with by assuming a rate-equation model according to [78]. A two-colour pump-probe scenario is sketched in fig. 6.1(a). Starting at positive delay time pulse 1 excites a population into an intermediate state proportional to its intensity I_1 . Its relaxation dynamics is described by an exponential decay with decay constant T called lifetime. The population is probed after a delay time τ by pulse 2. By performing this experiment for different delay times we can determine the intermediate state lifetime T .

Rate equations for the population N and the detected signal S are

$$\frac{d}{dt}N(t) = \mu_1^2 I_1(t) - \frac{N(t)}{T} \quad (6.1)$$

$$\frac{d}{dt}S_{rate}(t, \tau) = N(t)\mu_2^2 I_2(t - \tau) \quad (6.2)$$

Here we have assumed low excitation densities and have neglected depopulation and

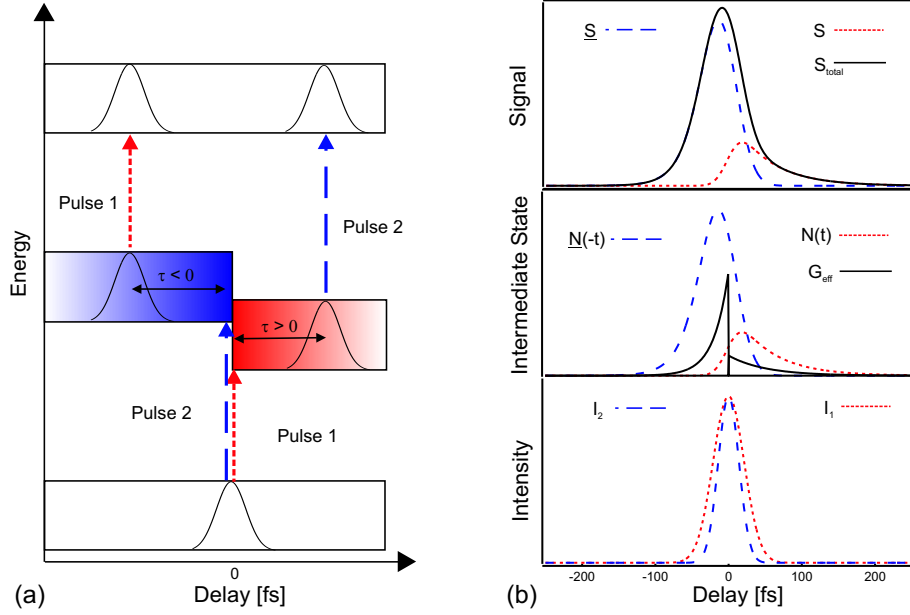


Figure 6.1: (a) Principle of a pump-probe cycle. At positive delay time pulse 1 excites a population into an intermediate state. This population starts to decay and is probed after a delay time τ by pulse 2. For negative delay, this process is reversed with pulse 2 acting as pump and pulse 1 as probe pulse. (b) Formation of the pump-probe signal. Bottom: Intensities of pulse 1 and pulse 2. Middle: Response function G_{eff} and populations N, \underline{N} in the two intermediate states. Top: Signal shapes for the two excitation pathways and their sum.

saturation effects. The absorption coefficients μ_1^2 and μ_2^2 result from the respective dipole moments μ .

The differential equation for N is solved by a Green's function G .

$$N(t) = \mu_1^2 I_1 \circ G(t, T) \quad \text{with} \quad G(t, T) = \Theta(t) e^{-t/T} \quad (6.3)$$

$$\text{and} \quad \Theta(t) = \text{Heavyside function} \quad (6.4)$$

The accumulated signal $S_{rate}(t \rightarrow \infty, \tau) = S_{rate}(\tau)$ then introduces a correlation.

$$S_{rate}(\tau) = \mu_2^2 \int_{-\infty}^{\infty} N(t) I_2(t - \tau) dt \quad (6.5)$$

$$= \mu_1^2 \mu_2^2 \int_{-\infty}^{\infty} [I_1(t) \circ G(t, T)] I_2(t - \tau) dt \quad (6.6)$$

$$= \mu_1^2 \mu_2^2 [I_1(t) \circ G(t, T)] \otimes I_2(t) \quad (6.7)$$

$$= \mu_1^2 \mu_2^2 [I_1(t) \otimes I_2(t)] \circ G(t, T) \quad (6.8)$$

In the final step, the result has been reordered to give the convolution of the response function G of the system with the time resolution of the experiment, determined by the cross-correlation of the two pulses $I_1 \otimes I_2$.

The reversed process is also possible, i.e. pump and probe pulse exchange their role. Pulse 2 excites then a population into an intermediate state and pulse 1 probes the population by transferring it to the detection channel. In general, both the lifetime \underline{T} and the absorption probabilities $\underline{\mu}_{1/2}^2$ are different. The pump-probe signal is described by

$$\underline{S}_{rate}(\tau) = \underline{\mu}_1^2 \underline{\mu}_2^2 I_1(t) \otimes [G(t, \underline{T}) \circ I_2(t)] \quad (6.9)$$

$$= \underline{\mu}_1^2 \underline{\mu}_2^2 [I_1(t) \otimes I_2(t)] \circ G(-t, \underline{T}) \quad (6.10)$$

and is depicted in fig. 6.1 for negative t and τ as the argument of G formally enters here with reversed sign. The total signal S_{rate}^{total} is the sum of both pathways and may be described by an effective response function G_{eff} :

$$S_{rate}^{total} = [I_1(t) \otimes I_2(t)] \circ G_{eff}(t) \quad (6.11)$$

$$\text{with } G_{eff}(t) = \underline{\mu}_1^2 \underline{\mu}_2^2 G(t, T) + \underline{\mu}_1^2 \underline{\mu}_2^2 G(-t, \underline{T}) \quad (6.12)$$

Fig. 6.1(b) exemplifies the formation of the signal. The bottom graph contains the temporal intensities of the two pulses. The middle graph shows the two response functions multiplied by the corresponding absorption coefficients as well as the resulting population evolution in the intermediate states. Finally the detected signals of both pathways and their sum is displayed in the top section.

6.2 Variation of Pump-Probe Intensities

In chapter 5.3 it was shown that we are able to excite and detect the plasmon. However, it is not yet clear how the plasmon excitation is involved in the photoemission process. Following the quantization rule, we may consider the plasmon as particle-like. This seems to be reasonable since it is excited by a photon and also converts into a photon. In that way it may also transfer its energy to a single electron. This picture becomes difficult if implicated with a two-photon photoexcitation. A double-plasmon excitation as proposed by Merschdorf et al. [80] can only be of minor importance. Such a double excitation would lead to direct photoemission as it overcomes the work function, preventing the detection of quantum well states as intermediates (see sec. 5.2). Yet, a coherent two-photon photoexcitation, with the plasmon participating in each excitation step, is not consistent with the particle picture. However, the results obtained by NO exposure in sec. 5.4 suggested such a process. In addition, polarization dependent measurements revealed a \sin^4 photoemission characteristics [80, 105], suggesting a double oscillation in agreement with Hertz's dipole emission characteristics of \sin^2 . In the following, further information on these processes will be gathered by comparison of the transition probabilities in each excitation step in and off plasmon resonance.

By using pulses of different colour in 2PPE we are able to distinguish between variable excitation paths. In fig. 6.2 the possible combinations for coherent two-colour

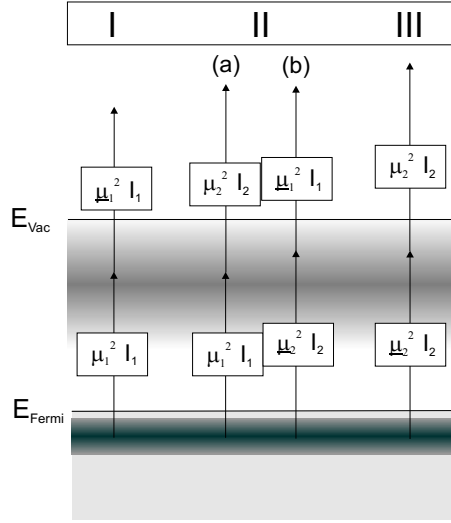


Figure 6.2: Possible excitation pathways for two-colour experiments. For determination of the transition probabilities μ_1^2 and μ_2^2 , we are able to distinguish between three different pathways as indicated at the top.

excitations are sketched. The excitation is in each case enhanced by the resonant transition via an intermediate state (see sec. 5.2). The transition strength for each step is proportional to the transition probability μ_1^2 , μ_2^2 and the laser intensity I_1 , I_2 , as indicated.

The two colours were selected such that one excitation occurs at plasmon resonance at 3.6 eV (Intensity I_2 in fig. 6.2) and the other off-resonant at 3.16 eV (Intensity I_1 in fig. 6.2). It was assured that both spots had the same width in space. However, pulses at 3.16 eV with 100 fs duration were considerably longer than pulses at 3.6 eV with 60 fs duration. The actual deviation was estimated by measuring their overlap by cross-correlation, revealing a factor of 1.5 for 3.16 eV [59].

As we are interested in the transition probabilities μ_1^2 , μ_2^2 we have to eliminate the intensities I_1 , I_2 . This is for pathways I and III easy to do by blocking the other colour and varying the intensity. Fig. 6.3(a) shows the resulting parabolas. Open circles represent 3.6 eV and closed circles 3.16 eV photon energy. A fit reveals their slopes which are proportional to

$$\mu_2^2 \cdot \mu_2^2 = 8.04, \text{ and } \mu_1^2 \cdot \mu_1^2 = 0.226 \cdot 1.5 \quad (6.13)$$

The disentanglement of the two contributions to pathway II is not so straightforward. If we overlap the two colours on the sample in space and time we always get contributions of all pathways depicted in fig. 6.2. To extract only the two-colour pathway II we have to subtract the background due to each single colour transition. This background is obtained at long delay time where a two-colour excitation can be excluded. As next step the light intensities were adjusted such that the signal intensity for each single

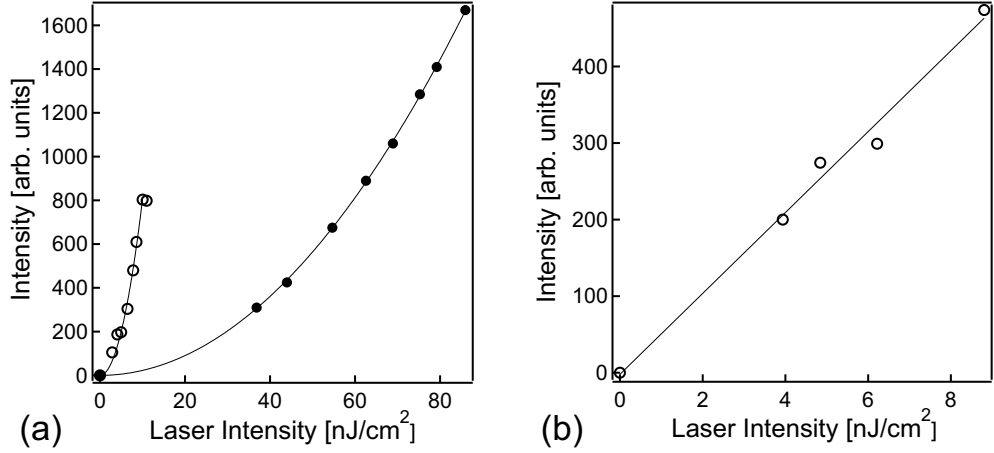


Figure 6.3: (a) Intensity dependence for single colour excitations to determine the slope. Open circles represent 3.6 eV photon energy, closed circles 3.16 eV. (b) Intensity dependence for two-colour excitation. The 3.16 eV intensity was kept constant while the 3.6 eV intensity was varied.

colour was the same. Subsequently, the intensity at 3.16 eV photon energy was kept constant while the intensity at 3.6 eV was varied. The resulting signal intensity dependence is shown in fig. 6.3(b). The data fit well to a line and the slope is proportional to

$$\mu_1^2 \cdot \mu_2^2 + \underline{\mu}_1^2 \cdot \underline{\mu}_2^2 = 3.35, \quad (6.14)$$

since the intensity I_1 is known. Up to now we have three equations for four unknown parameters, which is not sufficient to solve. However, we are basically interested in the last excitation step of II(a) and II(b). If we have a non-plasmon driven process the transition probabilities μ_2^2 and $\underline{\mu}_1^2$ should be equal as the final state is the same. For comparison of both transition probabilities we substitute $\mu_2^2 = a \cdot \underline{\mu}_1^2$, where a is a factor. Equations shown above then will change to

$$\underline{\mu}_2^2 \cdot \underline{\mu}_1^2 = 8.04 \cdot \frac{1}{a}, \text{ and } \mu_1^2 \cdot \underline{\mu}_1^2 = 0.339 \quad (6.15)$$

and

$$a \cdot \mu_1^2 \cdot \underline{\mu}_1^2 + \underline{\mu}_1^2 \cdot \underline{\mu}_2^2 = 3.35 \quad (6.16)$$

By combining equations 6.15 with 6.16, we get $a = 5.5$ as the enhancement of the transition probability μ_2^2 compared to $\underline{\mu}_1^2$. This huge difference can only be explained by a plasmon mediated transition and leads to the conclusion that both excitation steps in 2PPE at plasmon resonance are driven by plasmon excitation. If we put the above result into equations 6.15, we are able to determine the ratio of the excitation probabilities $\underline{\mu}_2^2/\mu_1^2$ for the first step being 4.3. This is still a big enhancement but lower than in case of the factor in the second step. If we take the intermediate state

transition into account, this difference is reasonable because the 3.16 eV excitation is more resonant in this regard (see sec. 5.2).

To summarize, we have observed an increase of the transition probability of 5.5 at plasmon resonance, corresponding to a field enhancement of 2.3. In 2PPE the field dependent emission yield scales with E^4 resulting in an enhancement by a factor of 30. This value is not so far from the quenching factor of 19 found by NO adsorption on the same particle size in sec. 5.4, which we attributed basically to a quenching of the plasmon excitation. The factor of 30 is about one order of magnitude lower than the enhancement of the 2PPE yield of particles at plasmon resonance compared to Ag(111), even after taking the supplementary QWS transition (sec. 5.2) into account. This is in agreement with the not assigned enhancement factor of 10 at $h\nu=3.16$ eV (sec. 5.3). The deviation has to be attributed to other properties of the nanoparticles, e.g. the reduced transport efficiency of excited electrons into the bulk [79].

6.3 Two-Colour Correlation

Two-colour correlation experiments provide on one hand the determination of excited electron lifetimes. This is of particular interest with respect to the involved unoccupied density of states, i.e. the quantum well states observed in sec. 5.2. On the other hand, different decay channels of the plasmon have been proposed [111]. First, the plasmon may decay by pure dephasing, i.e. the loss of the fixed phase correlation between individual excited electrons. This is considered to result in a distribution of the plasmon energy among participating electrons. Second, the plasmon may decay into a quasi-particle (electron-hole pair) or reemission of a photon (luminescence). These processes should result in a completely different population dynamics of energy levels above Fermi level. By choosing one colour at plasmon resonance and the other off-resonant, we are able to retrace the population dynamics upon plasmon excitation.

Experiments were carried out in the same manner as previously described. One colour was chosen at plasmon resonance (3.6 eV) and the other off-resonant (3.16 eV). Both colour intensities were adjusted for equal photoemission intensity in each case. The spots were overlapped in space and time on the sample. Subsequently, the delay between the pulses was changed in 45 fs steps. In fig. 6.4 resulting spectra of 7 nm silver particles are shown. Data are smoothed and the background due to single-colour transition is subtracted. At negative delay time the pump energy is 3.6 eV and the probe energy 3.16 eV, at positive delay time vice versa.

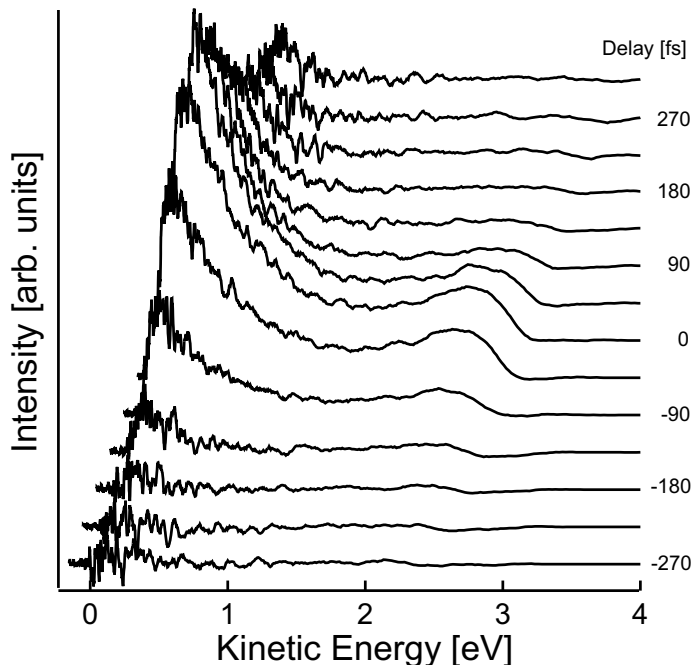


Figure 6.4: Two-colour correlation signal for varying delay times between 3.16 eV and 3.6 eV photon energy pulses on 7 nm silver particles.

In fig. 6.4 we can see the usual spectral shape for the nanoparticles. However, it has to be emphasized that each spectrum consists of the contributions of two different excitation pathways as discussed in the previous section. In this figure, the zero delay point indicates the point where the electron population for the high energy feature, excited with the different pump pulses, reaches its maximum. In sec. 6.1 we have seen, that the maximum intensity marks not necessarily the time when the two pulses meet at the surface. However, at high energy above Fermi level, this is in good approximation the case since we can exclude a contribution by hot electrons. At lower energies, we can see the maximum shifting to positive delay, which can be easier recognized in fig. 6.5 for different intermediate state energies.

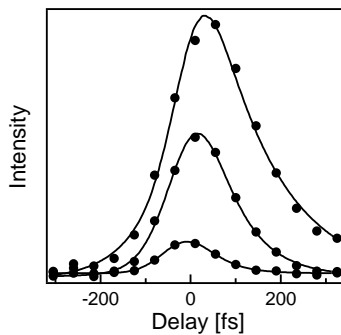


Figure 6.5: Two-colour correlation data at 3.05, 1.05, and 0.75 eV above Fermi energy (from bottom to top).

Each correlation curve, represented by closed circles in fig. 6.5, was obtained by integrating over an energy interval of 0.2 eV. The curve at the bottom belongs to 3.05 eV above Fermi energy, upper curves belong to 1.05 eV and 0.75 eV. It can be clearly seen that the intensity maximum shifts to positive delay as the energy above Fermi level decreases and the curve shape becomes asymmetric. These effects are due to the different excitation and decay pathways and have been analyzed by the rate-equation model derived in sec. 6.1. The corresponding fits are shown as black lines. The correlation width of both laser pulses was determined by the fitting at high energies to be 108 fs and kept constant for lower energies. Fit-parameters are the zero delay position, factors for the associated signal distributions, and the lifetimes of the intermediate states.

Fig. 6.6 represents the position of the zero delay point of the correlation as obtained from the fit. It is plotted in dependence on the intermediate state energy. As fit parameter, the zero delay point cannot be understood any more as the time delay when the two pulses meet at the surface. Rather, it indicates the maximum of the current population deconvolved by the laser pulse shapes (see sec. 6.1). Consequently, at high energies this position corresponds to zero delay of the pulses as long as we can exclude a hot electron contribution. At lower energies, however, the creation of hot electrons becomes relevant. Their usual generation process will be described below.

If we consider an electron being excited by a pump photon it may scatter with a low energy electron and transfer a part of its kinetic energy. This electron and the original one then may suffer the same procedure again leading finally to an electron cascade. Such a scenario will lead to a population of the unoccupied low energy states at times larger than time zero - the lower the energetic position the longer it takes.

In our model we were not able to include repopulation as described above. Therefore, at lower energies where these effects become relevant, the different excitation

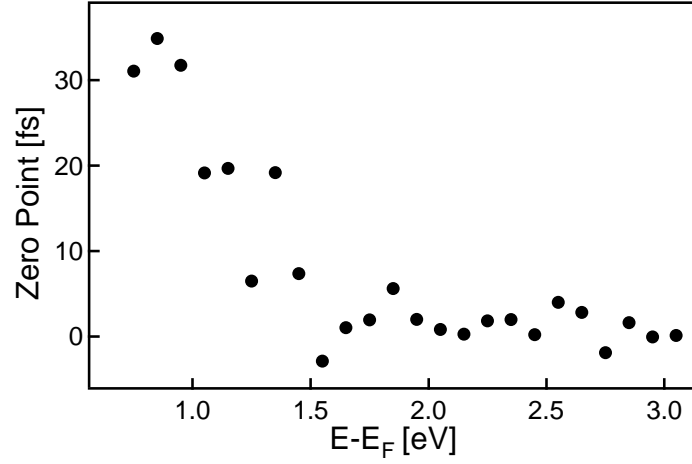


Figure 6.6: Zero delay position of the correlation in dependence on the intermediate state energy.

pathways are pivotal. As the 3.6 eV pulse probes deeper lying states with corresponding longer population times than the 3.16 eV pulse, the zero delay point is shifted to positive delay. This indicates that the plasmon decay proceeds in this case by coupling to single electrons. A direct decay channel of the plasmon due to dephasing of the excited electron cloud, as mentioned above, can only be of minor importance.

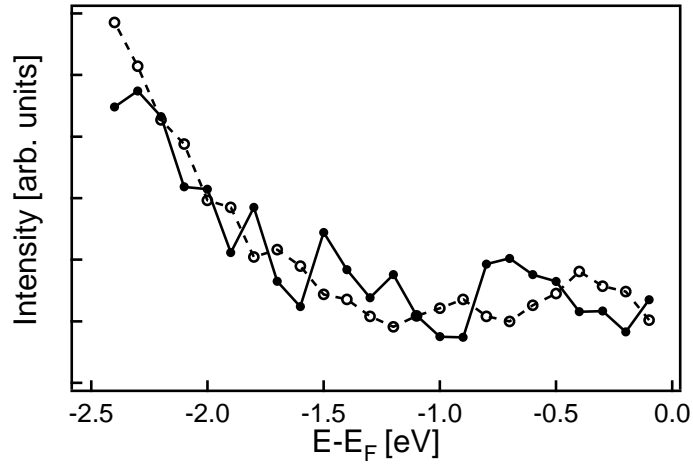


Figure 6.7: Fit-factors for each two-colour pathway of the correlation. Data for 3.6 eV pump energy are given by the solid line, data for 3.16 eV pump energy by the dashed line.

In fig. 6.7 the resulting factors $f_{1/2}$ for each pathway are plotted. $f_{1/2}$ are directly proportional to the signal intensity:

$$f_1 \propto \mu_1^2 I_1 \cdot \mu_2^2 I_2 \cdot \varrho(E_{occupied}) \cdot \varrho(E_{unoccupied}) \quad (6.17)$$

$$f_2 \propto \underline{\mu}_2^2 I_1 \cdot \underline{\mu}_1^2 I_2 \cdot \varrho(E_{occupied}) \cdot \varrho(E_{unoccupied}), \quad (6.18)$$

where $\varrho(E_{occupied})$ represents the occupied density of states and $\varrho(E_{unoccupied})$ the unoccupied density of states. That means: The resulting shapes in fig. 6.7 would be expected for a 2PPE spectrum of each excitation pathway separately. The solid line gives the result for 3.6 eV pump and 3.16 eV probe, the dashed line vice versa. The intensities of both spectra are equal giving support to the result of the previous section that plasmon excitation is involved in each pathway. Close to the Fermi edge again the feature due to the quantum well state transition can be seen for the dashed line. Although the noise for the solid line is higher still a feature can be identified but shifted to lower energy. This shift is due to the different pump energy and in agreement with the results of sec. 5.2. Now we focus on the onset of the hot electron distribution at around -1.4 eV in fig. 6.7. By addition of the pump energy to the energy scale we can compare this onset with fig. 6.6. In fact, it coincides with the onset of the zero point walk-off, supporting our previous interpretation.

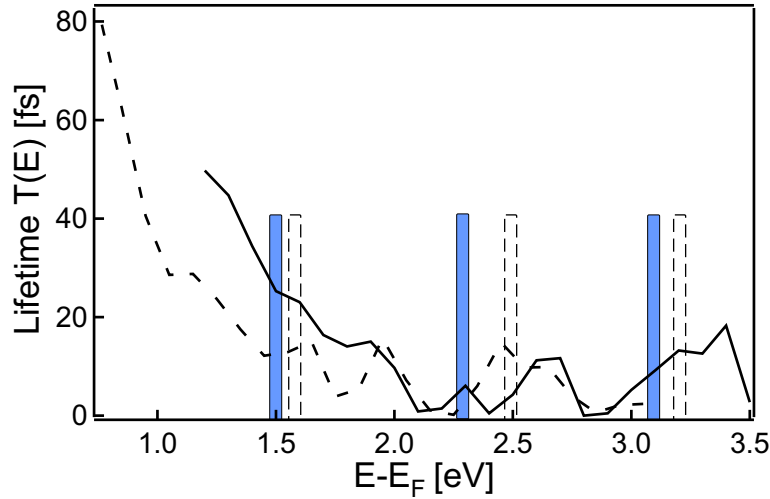


Figure 6.8: Intermediate state lifetimes for the different excitation paths in dependence on the intermediate state energy. The solid line represents data for 3.6 eV pump energy, the dashed line data for 3.16 eV pump energy. Solid bars indicate QWS positions for 7 nm particles (14 ML), dashed bars for 13 ML.

Finally, fig. 6.8 presents the population lifetime in dependence on the intermediate state energy. The solid line shows data for 3.6 eV pump energy, the dashed line for 3.16 eV. As in each case a different energy range is probed, the spectra are shifted. In the model and also in the fitting we have neglected population effects. Therefore, lifetimes lower than 1.5 eV appear too long. This gives an explanation for the deviation between the spectra at low energies. As the pump energy differs, the produced hot electrons populate different energy ranges.

In sec. 5.2 unoccupied quantum well states were detected which are expected to influence the lifetime at respective energies, as has been observed on thin silver films [95].

Indeed, at high energies pronounced fluctuations in lifetime occur. However, lifetime maxima do not coincide with quantum well state positions (solid bars in fig. 6.8), as expected from the model (see sec. 2.1.2) for this particle size. Rather, lifetime maxima appear shifted to higher energies, which could be attributed to the uncertainty of the particle preparation. For the adjacent smaller thickness (dashed bars in fig. 6.8) the agreement is much better. Yet, up to now no quantum well state has been detected beyond 3 eV above Fermi level. This has been assigned to the missing confinement due to the alumina band gap (see sec. 2.1.2), which is supposed to extend only up to around 3 eV. Alternatively, the lack of its former detection could be attributed to the reduced transmission probability in 2PPE to this state. Its wavefunction, extending further into the vacuum at high energies than at lower energies (see sec. 2.1.2), should deviate particularly from lower states.

Very recently, theoretical results on excited electron lifetimes for this particle size have been published [103]. These results show fluctuations of the lifetime depending on particle size, which was attributed to confinement effects. In contrast, Merschdorf et al. measured a monotonous increase of lifetimes for higher binding energies on silver nanoparticles on graphite [79]. Consistently, their 2PPE spectra did not show a distinct feature, as was detected in sec. 5.2 and attributed to a quantum well state transition. As data of the electron dynamics for these particle sizes are scarce, these measurements should be extended to different particle sizes, especially since electron dynamics is considered to play a key role in surface photochemistry.

Chapter 7

Summary and Outlook

This thesis is concerned with the study of electronic properties of nanoparticles by ultrashort laser spectroscopy, as it is the electronic properties of the substrate that are considered as the driving force in surface photochemistry. As a model system silver nanoparticles on an alumina film have been chosen, providing the optical excitation of the surface plasmon. One-photon and two-photon photoemission spectroscopy have been employed to probe the electronic structure as well as the electron dynamics on the nanoparticles. The first technique provides information on the occupied density of states in the vicinity of the Fermi level. The second technique is both sensitive to the occupied and unoccupied density of states and enables the optical excitation of the surface plasmon. To enhance the temporal resolution the existing laser system was extended by a self-constructed noncollinear optical parametric amplifier. Thus, the pulse width could be reduced from 100 fs to less than 60 fs, approaching the range of plasmon or excited state lifetimes of less than 20 fs. Furthermore, the noncollinear optical parametric amplifier opens up a wider spectral range which enables one-photon photoemission. Its small required pump intensity provides two-colour experiments.

Density of States

In one-photon photoemission (1PPE) spectroscopy a peak detected below the Fermi level could be assigned to the silver nanoparticles after eliminating the contribution by the support. With increasing particle size the peak shifted to lower binding energy. Lowering the work function by deposition of cesium reveals a similarity to the Shockley surface state on Ag(111), as also in the case of nanoparticles a partial quenching as well as a shift to higher binding energies are observed. An analysis of this shift within the phase accumulation model of surface states suggests a shift of the sp-band of 0.13 eV.

In 2PPE spectroscopy a broadened feature at equal binding energy as for 1PPE was detected. Its altering with photon energy can be assigned to a resonant transition from an occupied state via an unoccupied state. It is this occupied state that can be identified with that recorded in 1PPE. A lowering of the work function by deposition of cesium shows also an influence on the unoccupied state position and reveals additional

features above the Fermi level. The entire peak ensemble can be explained by quantum well states (QWS) as it is emphasized by a complete description of the experimental features by a QWS simulation for a broad particle size distribution. It gives evidence for the limitation of the QWS series at the first occupied state. The assumption of QWS in this case consequently reveal major differences in the electronic structure of the silver nanoparticles with respect to the single crystal: The sp-band structure must be postulated to change from nearly free electron like in case of Ag(111) to free electron like for the nanoparticles. This is explained by a disordered arrangement of atoms in a silver particle. A change of the sp-band structure gives also an explanation for the missing sp-intraband transition peak in case of nanoparticles which is prominent on Ag(111).

In 2PPE spectroscopy a tremendous enhancement of the photoemission yield on silver nanoparticles is observed. Depending on particle size it increased at $h\nu=3.16$ eV by up to 100 times compared to Ag(111) and the bare alumina film. At plasmon resonance ($h\nu=3.6$ eV) a further increase by a factor of 6 is found. A major part of the enhancement at $h\nu=3.16$ eV can be assigned to a resonant transition between QWS mentioned above. This makes a correction of the detected plasmon resonance necessary which has been determined only by the photoemission yield. The correction causes only a slight shift in energy but an immense decrease in intensity at the low energy wing of the plasmon resonance. This result suggests that the observed cross section for photodesorption on this system at $h\nu=3.2$ eV [105] is not plasmon induced but rather due to the intermediate state enhanced transition probability.

Role of Plasmon Excitation

The nonradiative decay channels of surface plasmon excitation, especially its coupling to the local density of states, have not been elucidated, yet. The present results obtained by two-photon photoemission spectroscopy however contribute to establish a picture of the interaction between plasmon excitation and the local density of states.

The plasmon excitation showed a pronounced coupling to the occupied state in the vicinity of the Fermi level, accompanied by an overall enhancement of the photoemission yield. The analysis of the 2PPE yield showing a deviation from cubic particle size dependence for particles greater than 8 nm suggests particle coalescence at these sizes. As has been found for the intermediate state transition, too, no qualitative difference between excitation at plasmon resonance and off-resonance was observed in this case. In general, the response of a silver nanoparticle to the photoinduced electric field can be regarded as screening of the nearly free 5s-electron cloud against the positive ion cores. Thus, a decrease of the photoemission yield for particle sizes larger than 10 nm can be interpreted in terms of retardation effects occurring when the photoinduced field is not homogeneous throughout the particle any more.

By exposure to NO the "hot spot" generation at Ag(111) defects, mediated by surface plasmons, is quenched. Also the plasmon excitation on nanoparticles is damped by

a factor of 19. A quadratic dependence of the photoemission yield on the induced work function change is found. This implies that both excitation steps in 2PPE are driven by plasmon excitation which has also been confirmed by two-colour experiments. In the latter case, an enhancement of the photoinduced electric field at plasmon resonance by a factor of 2.3 was determined.

This field enhancement results in a factor of 30 for the 2PPE yield at plasmon resonance which is a factor of 10 lower than the observed enhancement compared to Ag(111). A similar factor was found for the off-resonance excitation after elimination of the QWS transition enhancement. This factor must be attributed to other properties of the nanoparticles, e.g. a longer lifetime of excited electrons.

Finally, time resolved two-colour experiments show that the hot electron distribution in case of plasmon excitation stems from an initial photoexcitation of electrons corresponding to the applied photon energy. Due to electron-electron scattering these high energy electrons are cooled to produce a low energy distribution above Fermi level. This manifests in longer delay times for low energy electrons. Thus, the surface plasmon excitation equals the usual photoexcitation process of conduction electrons in a metal: The collective response to the photoinduced field condenses in the excitation of a single electron upon nonradiative decay. Since the plasmon excitation is resonant it leads to a higher absorption of light resulting in an enhancement of the surface electric field.

Summarizing we have presented a detailed analysis of the density of states of silver nanoparticles suggesting occupied and unoccupied quantum well states. This electronic structure differs essentially from that of a single crystal and is therefore considered to have a significant relevance in surface photochemistry as well as in heterogeneous catalysis. The excitation of the surface plasmon in these particles leads to a field enhancement supporting photoexcitation processes. Resulting photoemission spectra could be interpreted by a coupling of the plasmon to an electron of the occupied QWS upon decay.

Outlook

Time-resolved two-colour experiments provide the possibility to determine unoccupied state lifetimes of substrate and adsorbate. In the present case especially the interaction between quantum well states and the lowest unoccupied molecular orbital (LUMO) of adsorbates would be of particular interest with respect to surface photochemistry. As has been shown, quantum well states provide tailoring of the density of states by varying the particle thickness or the work function, e.g. by cesium deposition. In that fashion, an overlap with adsorbate orbital levels can be achieved and a selective photoexcitation to corresponding energy levels. This selectivity could be improved by narrowing the particle size distribution, e.g. by laser shaping [22, 118].

Another selectivity with respect to excitation is provided by plasmon excitation. By using a Ag/Au alloy its resonance position can be tuned in between the original

resonance positions. Further, the construction of particle shells of these metals provides different plasmon resonances on a single nanoparticle [14]. In that way, one could tailor the properties of the substrate in order to drive specific reactions. The exciting light then could simply be white.

As NO damps the plasmon excitation it seems not to be suitable as adsorbate with respect to plasmon induced desorption at first glance. However, as there exist other properties of nanoparticles enhancing the photodesorption cross section, an initial deactivation of the plasmon excitation may provide information on these properties. With this knowledge, subsequently other adsorbates could be used, which permit the excitation of the plasmon, as e.g. CO, which is supposed to have a smaller influence due to its lower bonding energy.

References

- [1] K. Al-Shamery. Dynamics of photoinduced reactions at oxide surfaces. *Applied Physics a-Materials Science & Processing*, 63(6):509–521, 1996.
- [2] K. AlShamery and H. J. Freund. Laser-stimulated desorption from surfaces. *Current Opinion in Solid State & Materials Science*, 1(5):622–629, 1996.
- [3] P. R. Antoniewicz. Model for electron-stimulated and photon-stimulated desorption. *Physical Review B*, 21(9):3811–3815, 1980.
- [4] A. Arbouet, D. Christofilos, N. Del Fatti, F. Vallee, J. R. Huntzinger, L. Arnaud, P. Billaud, and M. Broyer. Direct measurement of the single-metal-cluster optical absorption. *Physical Review Letters*, 93(12):127401–1–4, 2004.
- [5] A. Assion, T. Baumert, M. Bergt, T. Brixner, B. Kiefer, V. Seyfried, M. Strehle, and G. Gerber. Control of chemical reactions by feedback-optimized phase-shaped femtosecond laser pulses. *Science*, 282(5390):919–922, 1998.
- [6] S. Backus, C. G. Durfee, M. M. Murnane, and H. C. Kapteyn. High power ultrafast lasers. *Review of Scientific Instruments*, 69(3):1207–1223, 1998.
- [7] D. Bahnemann. *The Handbook of Environmental Chemistry, vol. 2(Part L), Photocatalytic Detoxification of Polluted Waters*. Springer-Verlag, Berlin, 1999.
- [8] I. Barke and H. Hovel. Confined shockley surface states on the (111) facets of gold clusters. *Physical Review Letters*, 90(16):166801–1–4, 2003.
- [9] L. Bartels, G. Meyer, K. H. Rieder, D. Velic, E. Knoesel, A. Hotzel, M. Wolf, and G. Ertl. Dynamics of electron-induced manipulation of individual CO molecules on Cu(iii). *Physical Review Letters*, 80(9):2004–2007, 1998.
- [10] C. L. Bastidas, A. Liebsch, and R. L. Mochan. Influence of d electrons on the dispersion relation of Ag surface plasmons for different single-crystal faces. *Physical Review B*, 63(16):165407–1–12, 2001.
- [11] M. Bauer and M. Aeschlimann. Dynamics of excited electrons in metals, thin films and nanostructures. *Journal of Electron Spectroscopy and Related Phenomena*, 124(2-3):225–243, 2002. Sp. Iss. SI.

- [12] M. Baumer and H. J. Freund. Metal deposits on well-ordered oxide films. *Progress in Surface Science*, 61(7-8):127–198, 1999.
- [13] I. Beauport, K. AlShamery, and H. J. Freund. Rotational alignment in the UV-laser induced desorption of CO from $\text{Cr}_2\text{O}_3(0001)$. *Chemical Physics Letters*, 256(6):641–648, 1996.
- [14] W. Bente, N. Nilius, N. Ernst, and H. J. Freund. Photon emission spectroscopy of single oxide-supported Ag-Au alloy clusters. *Physical Review B*, 72(4):45403–1–7, 2005.
- [15] C. N. Berglund and W. E. Spicer. Photoemission studies of copper + silver - experiment. *Physical Review a-General Physics*, 136(4A):1044–&, 1964.
- [16] C. N. Berglund and W. E. Spicer. Photoemission studies of copper + silver - theory. *Physical Review a-General Physics*, 136(4A):1030–&, 1964.
- [17] E. Bertel, P. Roos, and J. Lehmann. Promotion of catalytic reactions by depopulation of surface states. *Physical Review B*, 52(20):R14 384–387, 1995.
- [18] C. F. Bohren and D. R. Huffman. *Absorption and scattering of light by small particles*. John Wiley and Sons, New York, 1983.
- [19] M. Bonn, S. Funk, C. Hess, D. N. Denzler, C. Stampfl, M. Scheffler, M. Wolf, and G. Ertl. Phonon- versus electron-mediated desorption and oxidation of CO on $\text{Ru}(0001)$. *Science*, 285(5430):1042–1045, 1999.
- [20] S. Borowski, T. Kluner, and H. J. Freund. Complete analysis of the angular momentum distribution of molecules desorbing from a surface. *Journal of Chemical Physics*, 119(19):10367–10375, 2003.
- [21] S. Borowski, T. Kluner, H. J. Freund, I. Klinkmann, K. Al-Shamery, M. Pykavy, and V. Staemmler. Lateral velocity distributions in laser-induced desorption of CO from $\text{Cr}_2\text{O}_3(0001)$: experiment and theory. *Applied Physics a-Materials Science & Processing*, 78(2):223–230, 2004.
- [22] J. Bosbach, D. Martin, F. Stietz, T. Wenzel, and F. Trager. Laser-based method for fabricating monodisperse metallic nanoparticles. *Applied Physics Letters*, 74(18):2605–2607, 1999.
- [23] T. Brixner, G. Krampert, P. Niklaus, and G. Gerber. Optimal control of molecular femtochemistry. In *Laser Spectroscopy*, pages 85–95. 2004.
- [24] D. J. Burke, T. Vondrak, and S. R. Meech. Photodesorption and photochemical dynamics on roughened silver: Sulphur dioxide and carbonyl sulphide. *Surface Science*, 585(1-2):123–133, 2005.

- [25] W. Cai, H. Hofmeister, and M. Dubiel. Importance of lattice contraction in surface plasmon resonance shift for free and embedded silver particles. *European Physical Journal D*, 13(2):245–253, 2001.
- [26] C. I. Carlisle and D. A. King. Direct molecular imaging of NO monomers and dimers and a surface reaction on Ag(111). *Journal of Physical Chemistry B*, 105(18):3886–3893, 2001.
- [27] H. Cercellier, Y. Fagot-Revurat, B. Kierren, D. Malterre, and F. Reinert. Shockley state in epitaxial Ag films on Au(111). *Surface Science*, 566:520–525, 2004. Part 1.
- [28] K. P. Charle, L. Konig, S. Nepijko, I. Rabin, and W. Schulze. The surface plasmon resonance of free and embedded Ag-clusters in the size range $1,5 \text{ nm} < d < 30 \text{ nm}$. *Crystal Research and Technology*, 33(7-8):1085–1096, 1998.
- [29] C. K. Chen, A. R. B. Decastro, and Y. R. Shen. Surface-enhanced 2nd-harmonic generation. *Physical Review Letters*, 46(2):145–148, 1981.
- [30] T. C. Chiang. Photoemission studies of quantum well states in thin films. *Surface Science Reports*, 39(7-8):183–235, 2000.
- [31] N. Del Fatti, C. Flytzanis, and F. Vallee. Ultrafast induced electron-surface scattering in a confined metallic system. *Applied Physics B-Lasers and Optics*, 68(3):433–437, 1999.
- [32] W. Drachsel, M. Adelt, N. Nilius, and H. J. Freund. Cathodoluminescence of small silver particles on Al₂O₃/NiAl (110). *Journal of Electron Spectroscopy and Related Phenomena*, 122(3):239–249, 2002.
- [33] P. M. Echenique, R. Berndt, E. V. Chulkov, T. H. Fauster, A. Goldmann, and U. Hofer. Decay of electronic excitations at metal surfaces. *Surface Science Reports*, 52(7-8):219–317, 2004.
- [34] H. A. Engelhardt and D. Menzel. Adsorption of oxygen on silver single crystal surfaces. *Surface Science*, 57(2):591–618, 1976.
- [35] D. A. Evans, M. Alonso, R. Cimino, and K. Horn. Observation of quantum size effects in photoemission from Ag islands on GaAs(110). *Physical Review Letters*, 70(22):3483–3486, 1993.
- [36] G. H. Fecher, O. Schmidt, Y. Hwu, and G. Schonhense. Multiphoton photoemission electron microscopy using femtosecond laser radiation. *Journal of Electron Spectroscopy and Related Phenomena*, 126(1-3):77–87, 2002.

- [37] A. Fohlsch, P. Feulner, F. Hennies, A. Fink, D. Menzel, D. Sanchez-Portal, P. M. Echenique, and W. Wurth. Direct observation of electron dynamics in the attosecond domain. *Nature*, 436(7049):373–376, 2005.
- [38] R. Franchy, S. K. So, Z. C. Ying, and W. Ho. Photophysics and photochemistry of NO on Ag(111), Cu(111), and Si(111)7 x 7. *Surface Science*, 19:85–92, 1990.
- [39] P. M. W. French. The generation of ultrashort laser-pulses. *Reports on Progress in Physics*, 58(2):169–262, 1995.
- [40] H. Friedrich. *Theoretical Atomic Physics*. Springer, Berlin, 1998.
- [41] P. I. Geshev, S. Klein, T. Witting, K. Dickmann, and M. Hietschold. Calculation of the electric-field enhancement at nanoparticles of arbitrary shape in close proximity to a metallic surface. *Physical Review B*, 70(7):075402–1–16, 2004.
- [42] T. Gotz, W. Hoheisel, M. Vollmer, and F. Trager. Characterization of large supported metal-clusters by optical spectroscopy. *Zeitschrift Fur Physik D-Atoms Molecules and Clusters*, 33(2):133–141, 1995.
- [43] M. Gratzel. Solar energy conversion by dye-sensitized photovoltaic cells. *Inorganic Chemistry*, 44(20):6841–6851, 2005.
- [44] T. W. Hansen, J. B. Wagner, P. L. Hansen, S. Dahl, H. Topsøe, and C. J. H. Jacobsen. Atomic-resolution in situ transmission electron microscopy of a promoter of a heterogeneous catalyst. *Science*, 294(5546):1508–1510, 2001.
- [45] C. L. Haynes, A. D. McFarland, L. L. Zhao, R. P. Van Duyne, G. C. Schatz, L. Gunnarsson, J. Prikulis, B. Kasemo, and M. Kall. Nanoparticle optics: The importance of radiative dipole coupling in two-dimensional nanoparticle arrays. *Journal of Physical Chemistry B*, 107(30):7337–7342, 2003.
- [46] C. Hendrich, J. Bosbach, F. Stietz, F. Hubenthal, T. Vartanyan, and F. Trager. Chemical interface damping of surface plasmon excitation in metal nanoparticles: a study by persistent spectral hole burning. *Applied Physics B-Lasers and Optics*, 76(8):869–875, 2003.
- [47] C. Hess, S. Funk, M. Bonn, D. N. Denzler, M. Wolf, and G. Ertl. Femtosecond dynamics of chemical reactions at surfaces. *Applied Physics a-Materials Science & Processing*, 71(5):477–483, 2000.
- [48] H. Hovel. Clusters on surfaces: high-resolution spectroscopy at low temperatures. *Applied Physics a-Materials Science & Processing*, 72(3):295–302, 2001.
- [49] H. Hovel and I. Barke. Large noble metal clusters: electron confinement and band structure effects. *New Journal of Physics*, 5:31.1–31.14, 2003.

- [50] H. Hovel, B. Grimm, M. Pollmann, and B. Reihl. Cluster-substrate interaction on a femtosecond time scale revealed by a high-resolution photoemission study of the fermi-level onset. *Physical Review Letters*, 81(21):4608–4611, 1998.
- [51] R. Huber, H. Satzger, W. Zinth, and J. Wachtveitl. Noncollinear optical parametric amplifiers with output parameters improved by the application of a white light continuum generated in CaF₂. *Optics Communications*, 194(4-6):443–448, 2001.
- [52] R. M. Jaeger, H. Kuhlenbeck, H. J. Freund, M. Wuttig, W. Hoffmann, R. Franchy, and H. Ibach. Formation of a well-ordered aluminum-oxide overlayer by oxidation of NiAl(110). *Surface Science*, 259(3):235–252, 1991.
- [53] R. C. Jaklevic and J. Lambe. Experimental study of quantum size effects in thin metal-films by electron tunneling. *Physical Review B*, 12(10):4146–4160, 1975.
- [54] M. P. Jigato, D. A. King, and A. Yoshimori. The chemisorption of spin polarized NO on Ag111. *Chemical Physics Letters*, 300:639–644, 1999.
- [55] M. Kerker. *The Scattering of Light and Other Electromagnetic Radiation*. Academic Press, New York, physical chemistry edition, 1969.
- [56] I. Kinoshita, A. Misu, and T. Munakata. Electronic excited-state of NO adsorbed on Cu(III) - a 2-photon photoemission-study. *Journal of Chemical Physics*, 102(7):2970–2976, 1995.
- [57] T. Kluner, H. J. Freund, V. Staemmler, and R. Kosloff. Theoretical investigation of laser induced desorption of small molecules from oxide surfaces: A first principles study. *Physical Review Letters*, 80(23):5208–5211, 1998.
- [58] K. Kneipp, Y. Wang, H. Kneipp, L. T. Perelman, I. Itzkan, R. Dasari, and M. S. Feld. Single molecule detection using surface-enhanced Raman scattering (SERS). *Physical Review Letters*, 78(9):1667–1670, 1997.
- [59] E. Knoesel, T. Hertel, M. Wolf, and G. Ertl. Femtosecond dynamics of electronic excitations of adsorbates studied by 2-photon photoemission pulse correlation - Co/Cu(111). *Chemical Physics Letters*, 240(5-6):409–416, 1995.
- [60] E. Knoesel, A. Hotzel, and M. Wolf. Ultrafast dynamics of hot electrons and holes in copper: Excitation, energy relaxation, and transport effects. *Physical Review B*, 57(20):12812–12824, 1998.
- [61] W. Knoll. Interfaces and thin films as seen by bound electromagnetic waves. *Annual Review of Physical Chemistry*, 49:569–638, 1998.

- [62] C. P. Koch, T. Kluner, H. J. Freund, and R. Kosloff. Femtosecond photodesorption of small molecules from surfaces: A theoretical investigation from first principles. *Physical Review Letters*, 90(11):117601–1–4, 2003.
- [63] U. Kreibig and M. Vollmer. *Optical Properties of Metal Clusters*. Springer, Berlin, 1995.
- [64] A. Kubo, K. Onda, H. Petek, Z. J. Sun, Y. S. Jung, and H. K. Kim. Femtosecond imaging of surface plasmon dynamics in a nanostructured silver film. *Nano Letters*, 5(6):1123–1127, 2005.
- [65] S. Kwiet, D. E. Starr, A. Grujic, M. Wolf, and A. Hotzel. Femtosecond laser induced desorption of water from silver nanoparticles. *Applied Physics B-Lasers and Optics*, 80(1):115–123, 2005.
- [66] B. Lamprecht, A. Leitner, and F. R. Aussenegg. Shg studies of plasmon dephasing in nanoparticles. *Applied Physics B-Lasers and Optics*, 68(3):419–423, 1999.
- [67] I. Langmuir. A theory of adsorption. *Physical Review*, 6(1):79–80, 1915.
- [68] R. Lazzari, J. Jupille, and J. M. Layet. Electron-energy-loss channels and plasmon confinement in supported silver particles. *Physical Review B*, 68(4):045428–1–4, 2003.
- [69] J. Lehmann, M. Merschdorf, W. Pfeiffer, A. Thon, S. Voll, and G. Gerber. Surface plasmon dynamics in silver nanoparticles studied by femtosecond time-resolved photoemission. *Physical Review Letters*, 85(14):2921–2924, 2000.
- [70] J. Lerme, M. Pellarin, E. Cottancin, M. Gaudry, M. Broyer, N. Del Fatti, F. Vallee, and C. Voisin. Influence of lattice contraction on the optical properties and the electron dynamics in silver clusters. *European Physical Journal D*, 17(2):213–220, 2001.
- [71] J. Li, W.-D. Schneider, S. Crampin, and R. Berndt. Tunnelling spectroscopy of surface state scattering and confinement. *Surface Science*, 422:95–106, 1999.
- [72] J. Libuda and H. J. Freund. Molecular beam experiments on model catalysts. *Surface Science Reports*, 57(7-8):157–298, 2005.
- [73] A. Lindinger, A. Merli, M. Plewicki, F. Vetter, S. M. Weber, and L. Woste. Optimal control of isotope selective fragmentation. *Chemical Physics Letters*, 413(4-6):315–320, 2005.
- [74] E. G. McRae and M. L. Kane. Calculations on the effect of the surface-potential barrier in lead. *Surface Science*, 108(3):435–445, 1981.

- [75] N. Memmel. Monitoring and modifying properties of metal surfaces by electronic surface states. *Surface Science Reports*, 32(3-4):93–163, 1998.
- [76] M. Menges, B. Baumeister, K. Alshamery, H. J. Freund, C. Fischer, and P. Andresen. Dynamical Studies of UV-Laser-Induced No-Desorption from the Polar NiO(111) Versus the Nonpolar NiO(100) Surfaces. *Journal of Chemical Physics*, 101(4):3318–3325, 1994.
- [77] D. Menzel and R. Gomer. Desorption from metal surfaces by low-energy electrons. *Journal of Chemical Physics*, 41(11):3311–&, 1964.
- [78] M. Merschdorf. *Femtodynamics in Nanoparticles. The Short Lives of Excited Electrons in Silver*. PhD thesis, Julius-Maximilians-Universitaet Wuerzburg, 2002.
- [79] M. Merschdorf, C. Kennerknecht, and W. Pfeiffer. Collective and single-particle dynamics in time-resolved two-photon photoemission. *Physical Review B*, 70(19), 2004.
- [80] M. Merschdorf, W. Pfeiffer, A. Thon, S. Voll, and G. Gerber. Photoemission from multiply excited surface plasmons in Ag nanoparticles. *Applied Physics a-Materials Science & Processing*, 71(5):547–552, 2000.
- [81] G. Mie. Beiträge zur Optik trüber Medien, Speziell kolloider Metallösungen. *Annalen der Physik*, 25:377, 1908.
- [82] T. Miller and T. C. Chiang. Photoemission spectral lineshapes from metal overlayers. *Journal of Electron Spectroscopy and Related Phenomena*, 117:413–432, 2001.
- [83] T. Miller, W. E. McMahon, and T. C. Chiang. Interference between bulk and surface photoemission transitions in Ag(111). *Physical Review Letters*, 77(6):1167–1170, 1996.
- [84] T. Miller, A. Samsavar, G. E. Franklin, and T. C. Chiang. Quantum-well states in a metallic system - Ag on Au(111). *Physical Review Letters*, 61(12):1404–1407, 1988.
- [85] P. Monchicourt, M. Raynaud, H. Saringar, and J. Kupersztych. Resonant electron emission of silver spheroids induced by laser surface plasmon excitation. *Journal of Physics-Condensed Matter*, 9(27):5765–5775, 1997.
- [86] G. Moos. *Zur Dynamik niederenergetischer Elektronen in metallischen Festkörpern*. PhD thesis, Freie Universitaet Berlin, 2002.

- [87] A. Mugarza and J.E. Ortega. Electronic states at vicinal surfaces. *Journal of Physics C*, 15:S3281–S3310, 2003.
- [88] T. Mull, B. Baumeister, M. Menges, H. J. Freund, D. Weide, C. Fischer, and P. Andresen. Bimodal velocity distributions after ultraviolet-laser-induced desorption of NO from oxide surfaces - experiments and results of model-calculations. *Journal of Chemical Physics*, 96(9):7108–7116, 1992.
- [89] G. Neuhold and K. Horn. Depopulation of the Ag(111) surface state assigned to strain in epitaxial films. *Physical Review Letters*, 78(7):1327–1330, 1997.
- [90] N. Nilius. *Lichtemission aus einzelnen, oxidgetragenen Metallpartikeln im Rastertunnelmikroskop*. PhD thesis, Humboldt-Universitaet zu Berlin, 2001.
- [91] N. Nilius, H. M. Benia, C. Salzemann, G. Rupprechter, H. J. Freund, A. Brioude, and M. P. Pileni. Light emission spectroscopy of self-assembled arrays of silver nano-crystals with the stm. *Chemical Physics Letters*, 413(1-3):10–15, 2005.
- [92] N. Nilius, N. Ernst, and H. J. Freund. Photon emission spectroscopy of individual oxide-supported silver clusters in a scanning tunneling microscope. *Physical Review Letters*, 84(17):3994–3997, 2000.
- [93] N. Nilius, M. Kulawik, H. P. Rust, and H. J. Freund. Quantization of electronic states in individual oxide-supported silver particles. *Surface Science*, 572(2-3):347–354, 2004.
- [94] P. Nozieres and D. Pines. *The Theory of Quantum Liquids*. Perseus Books, Cambridge Massachusetts, 1999.
- [95] S. Ogawa, H. Nagano, and H. Petek. Optical intersubband transitions and femtosecond dynamics in Ag/Fe(1000) quantum wells. *Physical Review Letters*, 88(11):116801–1–4, 2002.
- [96] G. Pacchioni and N. Rosch. Modeling of supported metal-clusters - a density-functional study of co chemisorption on ni clusters deposited on alumina. *Surface Science*, 306(1-2):169–178, 1994.
- [97] F. Patthey and W. D. Schneider. Layer-by-layer-resolved quantum-well states in ultrathin silver islands on graphite - a photoemission-study. *Physical Review B*, 50(23):17560–17563, 1994.
- [98] F. Patthey and W.-D. Schneider. Layer-by-layer resolved surface states of ultrathin silver islands on graphite: a photoemission study. *Surface Science*, 334:L715–L718, 1995.

- [99] H. Petek and S. Ogawa. Femtosecond time-resolved two-photon photoemission studies of electron dynamics in metals. *Progress in Surface Science*, 56(4):239–310, 1997.
- [100] W. Pfeiffer, C. Kennerknecht, and M. Merschdorf. Electron dynamics in supported metal nanoparticles: relaxation and charge transfer studied by time-resolved photoemission. *Applied Physics a-Materials Science & Processing*, 78(7):1011–1028, 2004.
- [101] N. Pontius, V. Sametoglu, and H. Petek. Simulation of two-photon photoemission from the bulk sp-bands of Ag(111). *Physical Review B*, 72(11):115105–1–9, 2005.
- [102] D. Popovic, F. Reinert, S. Hufner, V. G. Grigoryan, M. Springborg, H. Cercellier, Y. Fagot-Revurat, B. Kierren, and D. Malterre. High-resolution photoemission on Ag/Au(111): Spin-orbit splitting and electronic localization of the surface state. *Physical Review B*, 72(4):45419–1–4, 2005.
- [103] M. Quijada, R. D. Muino, and P. M. Echenique. The lifetime of electronic excitations in metal clusters. *Nanotechnology*, 16(5):S176–S180, 2005. Sp. Iss. SI.
- [104] H. Raether. *Surface Plasmons*. Springer, Berlin, 1988.
- [105] C. Rakete. *Photoemission und Photodesorption von NO auf NiO und Silberclustern mit Femtosekunden-Laserpulsen*. PhD thesis, Freie Universitaet Berlin, 2003.
- [106] P. A. Redhead. Interaction of slow electrons with chemisorbed oxygen. *Canadian Journal of Physics*, 42(5):886–&, 1964.
- [107] F. Reinert, G. Nicolay, S. Schmidt, D. Ehm, and S. Hufner. Direct measurements of the L-gap surface states on the (111) face of noble metals by photoelectron spectroscopy. *Physical Review B*, 63(11):115415–1–7, 2001.
- [108] E. Riedle, M. Beutter, S. Lochbrunner, J. Piel, S. Schenkl, S. Sporlein, and W. Zinth. Generation of 10 to 50 fs pulses tunable through all of the visible and the NIR. *Applied Physics B-Lasers and Optics*, 71(3):457–465, 2000.
- [109] H. Sasaki, A. Tanaka, S. Suzuki, and S. Sato. Comparative angle-resolved photoemission study of Ag nanometer films grown on fcc Fe(111) and bcc Fe(110). *Physical Review B*, 70(11):115415–1–6, 2004.
- [110] M. Scharte, R. Porath, T. Ohms, M. Aeschlimann, J. R. Krenn, H. Ditlbacher, F. R. Aussenegg, and A. Liebsch. Do mie plasmons have a longer lifetime on resonance than off resonance? *Applied Physics B-Lasers and Optics*, 73(4):305–310, 2001.

- [111] M. Scharte, R. Porath, T. Ohms, M. Aeschlimann, B. Lamprecht, H. Ditlbacher, and F. R. Aussenegg. Lifetime and dephasing of plasmons in Ag-nanoparticles. In *Controlling and Using Light in Nanometric Domains*, volume 4456 of *PROCEEDINGS OF THE SOCIETY OF PHOTO-OPTICAL INSTRUMENTATION ENGINEERS (SPIE)*, pages 14–21. 2001.
- [112] W. Shockley. On the surface states associated with a periodic potential. *Physical Review a-General Physics*, 56(4A):317–323, 1939.
- [113] N. V. Smith. Phase-analysis of image states and surface-states associated with nearly-free-electron band-gaps. *Physical Review B*, 32(6):3549–3555, 1985.
- [114] N. V. Smith, N. B. Brookes, Y. Chang, and P. D. Johnson. Quantum-well and tight-binding analyses of spin-polarized photoemission from Ag/Fe(001) overlayers. *Physical Review B*, 49(1):332–338, 1994.
- [115] S. K. So, R. Franchy, and W. Ho. The adsorption and reactions of NO on Ag(111) at 80-K. *Journal of Chemical Physics*, 91(9):5701–5706, 1989.
- [116] C. Sonnichsen, T. Franzl, T. Wilk, G. von Plessen, and J. Feldmann. Plasmon resonances in large noble-metal clusters. *New Journal of Physics*, 4, 2002.
- [117] K. Stepan, J. Gudde, and U. Hofer. Time-resolved measurement of surface diffusion induced by femtosecond laser pulses. *Physical Review Letters*, 94(23):236103–1–4, 2005.
- [118] F. Stietz. Laser manipulation of the size and shape of supported nanoparticles. *Applied Physics a-Materials Science & Processing*, 72(4):381–394, 2001.
- [119] M. I. Stockman, S. V. Faleev, and D. J. Bergman. Localization versus delocalization of surface plasmons in nanosystems: Can one state have both characteristics? *Physical Review Letters*, 87(16):167401, 2001.
- [120] D. H. Sutter, I. D. Jung, F. X. Kartner, N. Matuschek, F. Morier-Genoud, V. Scheuer, M. Tilsch, T. Tschudi, and U. Keller. Self-starting 6.5-fs pulses from a Ti:Sapphire laser using a semiconductor saturable absorber and double-chirped mirrors. *Ieee Journal of Selected Topics in Quantum Electronics*, 4(2):169–178, 1998.
- [121] A. Tanaka, Y. Takeda, T. Nagasawa, and S. Sato. Dynamic final-state nanoparticle-substrate interaction in the photoemission of dodecanethiolate-passivated Ag nanoparticles on graphite substrates. *Physical Review B*, 67(3):033101–1–4, 2003.

- [122] S. Thiel, M. Pykavy, T. Kluner, H. J. Freund, R. Kosloff, and V. Staemmler. Three-dimensional ab initio quantum dynamics of the photodesorption of CO from $\text{Cr}_2\text{O}_3(0001)$: Stereodynamic effects. *Physical Review Letters*, 8707(7):077601–1–4, 2001.
- [123] S. Thiel, M. Pykavy, T. Kluner, H. J. Freund, R. Kosloff, and V. Staemmler. Rotational alignment in the photodesorption of CO from $\text{Cr}_2\text{O}_3(0001)$: A systematic three-dimensional ab initio study. *Journal of Chemical Physics*, 116(2):762–773, 2002.
- [124] C. Voisin, D. Christofilos, N. D. Fatti, F. Vallee, B. Prevel, E. Cottancin, J. Lerme, M. Pellarin, and M. Broyer. Size-dependent electron-electron interactions in metal nanoparticles. *Physical Review Letters*, 85(10):2200–2203, 2000.
- [125] T. Vondrak, D. J. Burke, and S. R. Meech. The dynamics and origin of NO photodesorbed from NO/Ag(111). *Chemical Physics Letters*, 327(3-4):137–142, 2000.
- [126] S. M. Weber, A. Lindinger, M. Plewicki, C. Lupulescu, F. Vetter, and L. Woste. Temporal and spectral optimization course analysis of coherent control experiments. *Chemical Physics*, 306(1-3):287–293, 2004.
- [127] F. Weik, A. Demeijere, and E. Hasselbrink. Wavelength dependence of the photochemistry of O_2 on Pd(111) and the role of hot-electron cascades. *Journal of Chemical Physics*, 99(1):682–694, 1993.
- [128] M. Wessendorf, C. Wiemann, M. Bauer, M. Aeschlimann, M. A. Schneider, H. Brune, and K. Kern. Electronic surface structure of n-ML Ag/Cu(111) and Cs/n-ML Ag/Cu(111) as investigated by 2PPE and STS. *Applied Physics a-Materials Science & Processing*, 78(2):183–188, 2004.
- [129] K. Wettergren, B. Kasemo, and D. Chakarov. Photodesorption of NO from graphite(0001) surface mediated by silver clusters. *Surface Science*, 593(1-3):235–241, 2005.
- [130] T. Wilhelm, J. Piel, and E. Riedle. Sub-20-fs pulses tunable across the visible from a blue-pumped single-pass noncollinear parametric converter. *Optics Letters*, 22(19):1494–1496, 1997.
- [131] M. Wolf. Femtosecond dynamics of electronic excitations at metal surfaces. *Surface Science*, 377(1-3):343–349, 1997.
- [132] V. P. Zhdanov and B. Kasemo. Specifics of substrate-mediated photo-induced chemical processes on supported nm-sized metal particles. *Journal of Physics-Condensed Matter*, 16(39):7131–7141, 2004.

- [133] F. M. Zimmermann and W. Ho. State-resolved studies of photochemical dynamics at surfaces. *Surface Science Reports*, 22(4-6):129–247, 1995.

List of Publications

F. Evers, C. Rakete, K. Watanabe, D. Menzel, and H.-J. Freund. Two-photon photoemission from silver nanoparticles on thin alumina films: Role of plasmon excitation. *Surface Science*, 593:43–48, 2005.

Danksagung

Mein besonderer Dank gilt:

Prof. Dr. Hans-Joachim Freund für die interessante Aufgabenstellung, seine Anregung und Unterstützung im Verlauf dieser Arbeit.

Dr. Wolfgang Drachsel für sein Engagement in technischen Dingen.

Dr. Christoph Rakete für den Aufbau des UHV-Systems.

Walter Wachsmann für seine Hilfsbereitschaft und etliche Probenpräparationen.

Dr. Kazuo Watanabe für die Möglichkeit, eigene Ideen umsetzen zu können.

Prof. Dr. Dietrich Menzel für kritische Fragen.

Dr. Kerstin Jacobsen für zahlreiche Tips zur Endfassung dieser Arbeit.

Prof. Dr. Thomas Möller für die Bereitschaft zur Begutachtung dieser Arbeit.

Lebenslauf

Name	Florian Evers
Geburtsdatum	25.4.1972
Geburtsort	München
1978 - 1982	Grundschule in Ismaning bei München
1982 - 1991	Reuchlin-Gymnasium Pforzheim, Baden-Württemberg
Juli 1991	Allgemeine Hochschulreife
1991 - 1993	Zivildienst beim Arbeiter-Samariter-Bund in Pforzheim
April 1993	Immatrikulation für Physik an der Technischen Universität Berlin
Januar 1998	Studienarbeit über <i>Cavity Ring Down-Spektroskopie an 9-(N-carbonyl)-Anthrazen</i>
1998 -1999	Studentische Hilfskraft mit Aufgabe der Beschichtung von Substraten und deren Untersuchung
1998 - 2000	Diplomarbeit bei Prof. Dr. P. Zimmermann zur <i>Identifikation von Clusterzuständen an bichromophoren Molekülen mittels Ionisationsanregungsspektroskopie im Molekülstrahl</i>
Februar 2000	Abschluß als Diplom-Physiker
2000 - 2001	Programmierung von "Embedded Systems" in C++ zur Steuerung einer Röntgen-Meßanlage
April 2001	Forschungsaufenthalt am CEA/LETI in Grenoble/Frankreich zur Präparation dünner Metallfilme
Seit März 2002	Promotion am Fritz-Haber-Institut Berlin bei Prof. Dr. H.-J. Freund: <i>Comparative Study of Silver Nanoparticles and Silver(111) by means of Femtosecond Laser Pulses</i>

Berlin, 25. Januar 2006

Florian Evers